Terahertz Laser Induced Ratchet Effects and Magnetic Quantum Ratchet Effects in Semiconductor Nanostructures

DISSERTATION

zur Erlangung des Doktorgrades der Naturwissenschaften
doctor rerum naturalium
(Dr. rer. nat.)
Fakultät für Physik
Universität Regensburg

vorgelegt von
Philipp Faltermeier
aus Mallersdorf-Pfaffenberg
im Jahr 2017

Die Arbeit wurde von Prof. Dr. Sergey D. Ganichev angeleitet.

Das Promotionsgesuch wurde am 8. Juni 2017 eingereicht.

Prüfungsausschuss:

Vorsitzende:	Prof. Dr. Milena Grifoni
1. Gutachter:	Prof. Dr. Sergey D. Ganichev
2. Gutachter:	PD Dr. Tobias Korn
weiterer Prüfer:	Prof. Dr. Christian Schüller

Contents

1 Introduction

The classical ratchet and the quantum ratchet effects occur in spatially periodic non-centrosymmetric systems which are able to transport non-equilibrium particles in the absence of an average macroscopic force [1–5]. By driving such systems out of thermal equilibrium, for example by high frequency alternating electric fields, a direct electric current is generated in semiconductors and semiconductor nanostructures [6–20]. The requirement of a non-centrosymmetric system can be fulfilled by either making use of an in-built asymmetry induced by a crystallographic structure (in this case ratchet effects are called photogalvanic effects [11, 15, 21]) or by an artificial structure superimposed on typically two-dimensional semiconductor materials [11, 13, 14, 22–25]. Such structures were realized on semiconductor quantum wells [14, 15, 22, 26] and on top of graphene [27, 28]. These experiments demonstrate that, in particular, the ratchet effects are efficiently excited by terahertz radiation. Based on the experimental data, the basic physics of the ratchet effect in low dimensional electron systems was explored, providing information on the non-equilibrium transport in these systems. The influence of the magnetic field, however, as well as the ratchet effect as possibility for detecting the terahertz radiation's polarization states were not considered up to now.

The core of this thesis is to investigate the influence of the magnetic field on the ratchet effects, which are generated by the terahertz radiation. The terahertz electric field and the external magnetic field in combination with the lateral asymmetric dual grating gate structure on top of the quantum well structure give rise to several new effects which will be investigated in this thesis. One of these effects is that the generated current exhibits sign-alternating $1/B$-periodic oscillations with amplitudes by orders larger than the ratchet current at zero magnetic field. Further, it will be shown that the sign and the amplitude of the magnetic quantum ratchet current can be effectively controlled by the applied gate voltages. Moreover, it will be demonstrated that different directions of the linearly polarized radiation, as well as left-handed and right-handed circularly polarized radiation, can change the amplitude and even the sign of the current oscillations. These new effects are observed in CdTe and in diluted magnetic semiconductor (Cd,Mn)Te quantum wells. The latter mate-

rial leads to enhanced spin related phenomena due to the exchange interaction of the electrons with manganese (Mn^{2+}). This interaction allows to explore the role of the spin ratchet effect [29] by changing either the temperature, the magnetic field or the potentials induced by the voltages applied to the top gate structure. Since these materials were not investigated for ratchet effects up to now, the ratchet currents at zero magnetic field are also investigated. The obtained experimental phenomena are discussed by terms of the simultaneously developed theory.

The fact that the ratchet current is alterable by different gate voltages and also by different polarization states of the radiation, provides the basis for the development of a polarization sensitive detector. In this work, an InAlAs/InGaAs/InAlAs/InP based high electron mobility transistor was chosen as detecting material [23–25, 30] which has previously been shown to be a good material for detection. Although, the recently developed terahertz detectors based on field effect transistors are focused on single gated structures, several groups demonstrated that higher sensitivities are anticipated for structures with periodic symmetric and asymmetric metal stripes or gates [13, 17, 23, 26, 30–34].
In this thesis, it will be demonstrated that the generated direct photocurrent, excited by terahertz radiation in a dual grating gate InGaAs high electron mobility transistor, is sensitive to the radiation helicity and the linear polarization state of the radiation. These phenomena are well described in terms of the ratchet effects [15–17, 22, 30] excited in two dimensional electron systems with a spatially periodic *dc* in-plane potential [17, 19, 23]. Furthermore, it will be shown that single photocurrent contributions, e.g. those induced by the helicity of the radiation, can be turned on and off by a proper choice of the voltages applied to the top gate structure. In particular, the photocurrent changes its direction by inverting the polarization helicity. These effects open up new possibilities for an all-electric detector for the terahertz radiation polarization state at room temperature.

The thesis is organized as follows: In Chap. 2, the theoretical background, which serves as a basis for the study of the magnetic ratchet effect as well as

the ratchet effect in the terahertz detection, is presented. The theoretical background includes the basic principle of the ratchet effect and the longitudinal magneto-resistance, as well as a description of the diluted magnetic semiconductors. The experimental methods are discussed in Chap. 3, containing a brief introduction of the used radiation sources, as well as the Stokes parameters of the radiation's polarization state and the methods for its variation. Chapter 4 is dedicated to the samples, including their growth, the processing of the top gate structures and their characterization. In Chap. 5, the experimental results of the polarization independent and polarization dependent ratchet effect at zero magnetic field are presented, as well as the microscopy theory and a short summary. Next follows an investigation of the magnetic quantum ratchet effect in Chap. 6, starting with the experimental results and discussion, the semiclassical theory and a summary in the last section. The data and theory for the polarization sensitive magnetic quantum ratchet effect are shown and discussed in Chap. 7. The ratchet effect as terahertz radiation detector is presented in Chap. 8, whilst Chap. 9 gives a summary of the whole work.

2 Physical Background

The magnetic quantum ratchet effect (MQRE), which is observed and explored in this work, is based on different physical models. To aid understanding, these models will be briefly discussed in this chapter. After describing the ratchet effect in semiconductor heterostructures with lateral top gate potentials, the longitudinal magneto-oscillations - describing the oscillating behavior of the MQRE in the magnetic field B - will be explained. In addition, as most experiments for the MQRE were carried out on diluted magnetic semiconductors (DMS), the influence of the DMS materials will be briefly introduced.

2.1 Basics of the Ratchet Effect

The ratchet effect is generally known as the generation of a direct current, induced by a terahertz (THz) radiation in two-dimensional (2D) semiconductor systems with an asymmetric top gate structure. The common idea is that a non-equilibrium spatially periodic non-centrosymmetric system is able to transport particles under the influence of an oscillating force, which is zero in average [7, 14–16, 22, 28, 35, 36].
Blanter and Büttiker introduced a model describing the motion of particles in a periodic potential and their exposure to a periodic temperature modulation [7]. Figure 2.1(a) shows a schematic drawing of their considered system. In this system, a superlattice is irradiated through a mask of the same period, but phase shifted with respect to the superlattice [6]. This spatially modulated irradiation leads to a locally modulated electron gas heating inducing a temperature gradient in the two-dimensional electron gas (2DEG). The influence of this gradient yields to a direct current of the charge carriers.

A possible realization of this system with small variations of the top structure is shown in Fig. 2.1(b). The superlattice is replaced by a lateral periodic potential induced by a non-centrosymmetric metal grating on top of the sample surface. Therefore, the in-plane modulation of the radiation does not appear via a mask with periodic structures but instead due to the near-field effect of the THz radiation propagating through the metal grating [22]. This near-field diffraction heats the electron gas locally.

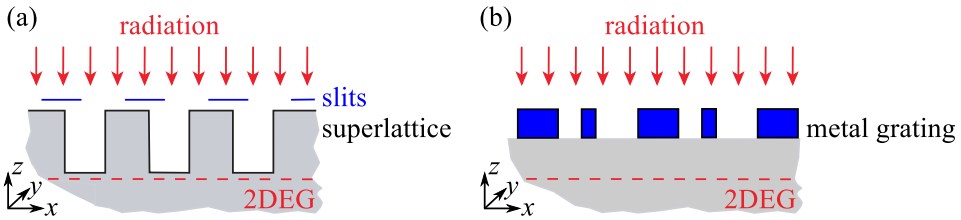

Figure 2.1: (a) Idea to realize a electronic ratchet by Blanter and Büttiker [7, 14]. Superlattice irradiated through a mask of the same period but phase shifted with respect to the underlying superlattice. (b) shows one possible realization of this idea with metallic gate stripes on top of the sample (adapted from [14, 22]).

A theoretical model for the phenomenological description of the ratchet effect, following the descriptions in Refs. [15, 22, 35], will be given here. The considered structure has a quantum well with an one-dimensional periodic potential $V(x)$ on top of the surface with the property $V(x) = V(x + d)$ and the period d. The coordinate system is defined in Fig. 2.1, with the x- and y-directions lying in the quantum well (QW) plane, the z-axis being parallel to the growth direction and pointing against the propagation of the radiation. The radiation shining on the QW is an alternating time dependent in-plane electric field $\boldsymbol{E}(x, t)$, described as

$$\boldsymbol{E}(x,t) = \boldsymbol{E}_\omega(x)e^{-i\omega t} + \boldsymbol{E}^*_\omega(x)e^{i\omega t} \,,$$

with the radiation frequency ω, the time t and the amplitude $\boldsymbol{E}_\omega(x)$ modulated along the x-direction and with the same period as the static lateral potential, $\boldsymbol{E}_\omega(x) = \boldsymbol{E}_\omega(x + d)$. The electric field $\boldsymbol{E}_\omega(x)$ and the potential $V(x)$ can be written in a general form [15, 22]:

$$\begin{aligned} \boldsymbol{E}_\omega(x) &= \boldsymbol{E}_0 \left[1 + \sum_{n=1}^{\infty} h_n \cos\left(nqx + \varphi_{E,n}\right) \right] \,, \\ V(x) &= \sum_{n=1}^{\infty} V_n \cos\left(nqx + \varphi_{V,n}\right) \,, \end{aligned} \tag{2.1}$$

with the phases for the electric field $\varphi_{E,n}$ and the potential $\varphi_{V,n}$. The coordinate independent amplitude of the electric field is given by $\boldsymbol{E}_0$. The coefficients h_n and V_n are real values, n is an integer number and q is $2\pi/d$.

The ratchet effect will be described by using the classical Boltzmann equation for the electron distribution function $f_{\boldsymbol{k}}(x,t)$, as provided in Ref. [15,22]. The Boltzmann equation can be used when the potential $V(x)$ is weak and smooth, satisfying $|V(x)| \ll \varepsilon_e$ and $q \ll \boldsymbol{k}$. The electron energy ε_e is defined as $\varepsilon_e = \hbar^2\boldsymbol{k}^2/2m^*$ with the Planck constant $\hbar$, the electron wave vector $\boldsymbol{k}$ and the effective mass m^*. The typical electron energy ε_e has to be much larger than the photon energy $\hbar\omega$, which is fulfilled in the THz frequency range. The Boltzmann equation is given by [15,22]

$$\left(\frac{\partial}{\partial t} + \boldsymbol{v}_{\boldsymbol{k},x}\frac{\partial}{\partial x} + \frac{\boldsymbol{F}(x,t)}{\hbar}\frac{\partial}{\partial \boldsymbol{k}}\right) f_{\boldsymbol{k}}(x,t) + Q_k = 0, \tag{2.2}$$

where $\boldsymbol{v}_{\boldsymbol{k}} = \hbar\boldsymbol{k}/m^*$ is the electron velocity and $\boldsymbol{k} = (k_x, k_y)$ is lying in the QW plane. Q_k is the collision integral and the force $\boldsymbol{F}(x,t)$ consists of two terms:

$$\boldsymbol{F}(x,t) = -\frac{dV(x)}{dx}\hat{\boldsymbol{e}}_x + e\boldsymbol{E}(x,t),$$

with the electron charge e and the unit vector $\hat{\boldsymbol{e}}_x$ along the x-direction. The collision integral Q_k is the sum of the energy relaxation and the elastic scattering terms (for more information, see Refs. [15,22]).

From the Boltzmann equation, the average electron current $\boldsymbol{j}$ is calculated which is given in the following equation:

$$\boldsymbol{j} = 2e\sum_{\boldsymbol{k}} \boldsymbol{v}_{\boldsymbol{k}}\overline{f}_{\boldsymbol{k}}\,. \tag{2.3}$$

The bar over the electron distribution function $f_{\boldsymbol{k}}$ means averaging over the spatial coordinate x and time t. The prefactor 2 stems from the electron spin degeneracy.

The current $\boldsymbol{j}$ is obtained by solving the classical Boltzmann Eq. (2.2). Therefore, the electron distribution function $f_{\boldsymbol{k}}(x,t)$ is expanded in third order perturbation theory. This means the function is expanded up to the second order in powers of the radiation electric field and in the first order of the static lateral potential $V(x)$:

$$f_{\boldsymbol{k}}(x) = f^{(0)}_{\boldsymbol{k}}(x) + f^{(1)}_{\boldsymbol{k}}(x,t) + f^{(2)}_{\boldsymbol{k}}(x,t)\,. \tag{2.4}$$

The first term, $f^{(0)}_{\boldsymbol{k}}(x)$, is the equilibrium distribution function and $f^{(1)}_{\boldsymbol{k}}(x,t)$ depends linearly on the electric field $\boldsymbol{E}(x,t)$. The last term, $f^{(2)}_{\boldsymbol{k}}(x,t)$, is quadratic

in $\boldsymbol{E}(x,t)$ and, therefore, linear in the intensity of the radiation. For further calculations only the time-independent contribution $f_{\boldsymbol{k}}^{(2)}(x) = \xi_{\boldsymbol{k}}(x)$ is necessary. The electron distribution function in Eq. (2.3) is substituted by Eq. (2.4). By successive iteration of the kinetic equation Eq. (2.2) and summing over all $\boldsymbol{k}$, the current can be written as:

$$\boldsymbol{j} = \mu_e \left\{ \overline{\delta N(x) \frac{dV(x)}{dx}} \hat{\boldsymbol{e}}_x + 2|e| \mathrm{Re}[\overline{\boldsymbol{E}_\omega^*(x) \delta N_\omega(x)}] \right\} . \tag{2.5}$$

Here, $\mu_e = |e|\,\tau/m^*$ is the electron mobility with the momentum relaxation time τ. The spatially modulated electron densities are given by

$$\delta N(x) = 2 \sum_{\boldsymbol{k}} \xi_{\boldsymbol{k}}(x) \text{ and} \qquad \delta N_\omega(x) = 2 \sum_{\boldsymbol{k}} f_{\boldsymbol{k}\omega}^{(1)}(x).$$

The first term on the right hand side in Eq. (2.5) describes the polarization independent Seebeck ratchet effect and the second term is the polarization dependent ratchet effect. Several assumptions have to be made to allow further calculations of the ratchet current, namely [15, 22]:

- the energy relaxation time τ_ε is larger than the momentum relaxation time τ and the inverse frequency ω^{-1}
- the electron mean free path $l_e = v_T \tau$ and the energy diffusion length $l_\varepsilon = v_T \sqrt{\tau \tau_\varepsilon}$ are both small compared to the superlattice period d. The thermal velocity v_T is given by $v_T = \sqrt{2 k_\mathrm{B} T / m^*}$ with the Boltzmann constant k_B and the temperature T
- the influence of *ac* diffusion on first-order amplitudes $f_{\boldsymbol{k}\omega}^{(1)}(x,t)$ is neglected, which is correct for $v_T q \ll \omega$
- no restrictions on the value of the product $\omega\tau$

The Seebeck ratchet current contains the static correction $\delta N(x)$ of the spatially modulated electron density. The spatially modulated radiation heats the two-dimensional electron gas, which changes the effective temperature of the electron gas from the equilibrium value T to $T(x) = T_e + \delta T(x)$. Here, T_e is the average electron temperature and the temperature correction term $\delta T(x)$

oscillates in space with the period d [16]. The temperature gradient, caused by $\delta T(x)$, leads to a redistribution of the electron density $\delta N(x)$ and therefore to an appearance of an electric-field-induced static correction of $\delta N(x)$ [22]. Further, $\delta T(x)$ causes an inhomogeneous correction to the conductivity, leading to a direct current which is independent of the polarization state of the radiation.

The polarization dependent ratchet current can be calculated when the second term in Eq. (2.5) is taken into account. The spatially modulated electron density $\delta N_\omega(x)$ is time-dependent and satisfies the continuity equation. From the continuity equation, it follows that - when calculating the current $\boldsymbol{j}$ - it is sufficient to find a correction to $\delta N_\omega(x)$. This correction contribution is linear in the lateral potential and replaces $\boldsymbol{E}_\omega(x)$ by a non-modulated electric field $\boldsymbol{E}_0$ [15, 22]. Taking the average over the x-direction and time t of the spatially modulated electron density $\delta N_\omega(x)$ and the electric field $\boldsymbol{E}^*_\omega(x)$ leads to the polarization dependent ratchet photocurrent.

The ratchet current can be written as the sum of the polarization independent Seebeck ratchet and the polarization dependent ratchet effect. Therefore, Eq. (2.5) can be further treated by averaging over the x-direction and considering the modulated electron densities. The polarization independent and dependent ratchet currents in x- and y-direction are given by [15, 22]

$$\begin{aligned} j_x &= \bar{I}[\chi_1 + \chi_2(|\hat{\boldsymbol{e}}_x|^2 - |\hat{\boldsymbol{e}}_y|^2)] \,, \\ j_y &= \bar{I}[\chi_3(\hat{\boldsymbol{e}}_x\hat{\boldsymbol{e}}^*_y + \hat{\boldsymbol{e}}_y\hat{\boldsymbol{e}}^*_x) - \gamma P_{\mathrm{circ}}\hat{\boldsymbol{e}}_z] \,, \end{aligned} \tag{2.6}$$

with $P_{\mathrm{circ}}\hat{\boldsymbol{e}}_z = i(\hat{\boldsymbol{e}}_x\hat{\boldsymbol{e}}^*_y - \hat{\boldsymbol{e}}_y\hat{\boldsymbol{e}}^*_x)$. The average light intensity $\bar{I}$ is defined by

$$\bar{I} = \frac{cn_\omega}{2\pi}(|E_{0x}|^2 + |E_{0y}|^2) \,,$$

with the speed of light in vacuum c and the frequency dependent refractive index n_ω. The remaining coefficients are

$$\chi_2 = \chi_3 = -\omega\tau\gamma, \qquad \chi_1 = (4\tau_\epsilon - \tau)\omega\gamma \,,$$

with

$$\gamma = \zeta\frac{\pi e^2}{\hbar c n_\omega}\frac{\hbar q}{m^*}\frac{V_1}{k_{\mathrm{B}}T}\frac{\mu_e N_0 \tau}{\omega(1+\omega^2\tau^2)} \,.$$

Here, $\zeta = h_1 \sin(\varphi_V - \varphi_E)$ is called the asymmetry parameter and N_0 is the x-independent electron density. The Seebeck ratchet current is represented by the coefficient χ_1, whilst the linear ratchet effect is attributed to $\chi_2(|\hat{\boldsymbol{e}}_x|^2 - |\hat{\boldsymbol{e}}_y|^2)$ and $\chi_3(\hat{\boldsymbol{e}}_x\hat{\boldsymbol{e}}_y^* + \hat{\boldsymbol{e}}_y\hat{\boldsymbol{e}}_x^*)$. The circular polarization sensitive ratchet current is described by $\gamma P_{\mathrm{circ}}\hat{\boldsymbol{e}}_z$.
In the ratchet current, the phase shift ζ is included in all coefficients χ_1, χ_2, χ_3 and γ. Therefore, $(\varphi_V - \varphi_E) \neq n\pi$ is necessary to obtain a current, with n as an integer number. The phase shift is achieved when the electric field and the potential are out of phase with respect to each other.
In order to clarify the contribution of the intensity of the electric field $|E(x)|^2$ and the variation of the potential $\partial V/\partial x$ on the current generation, the equation for the ratchet currents can be rewritten. The current $j_{x/y}$ can be expressed as [16, 22]:

$$j_{x/y} \propto \Xi$$

with

$$\Xi = qV_1h_1E_0^2 \sin(\varphi_V - \varphi_E) = \overline{|E(x)|^2 \frac{\partial V}{\partial x}}. \tag{2.7}$$

Thereby, the simplest form of the electric field and lateral-potential modulation from Eq. (2.1) for $n = 1$ is taken into account. The parameter Ξ will be treated as *lateral asymmetry* and its value may change its sign due to changes of the potential $V(x)$ [37].

2.2 Longitudinal Magneto-Resistance Oscillations

The longitudinal magneto-resistance oscillations can be observed in a two-dimensional electron gas when high magnetic fields are applied perpendicularly to the two-dimensional quantum well plane at low temperatures. One of the characteristics of the 2DEG is that the motion of the electrons in growth directions of the quantum well is quantized, but the electrons can move in the QW plane without restrictions. Under application of a magnetic field, however, the electron energy spectrum is additionally quantized, forming discrete Landau levels. Thereby, each Landau level is connected to a separated δ-peak

in the density of states $\nu_\pm$ for the condition $k_\mathrm{B}T < \hbar\omega_c$ [38]. Here, the angular frequency is $\omega_c = eB/m^*$ with the magnetic field B.
Even though, the Landau levels (LL) and, therefore, the peaks of the density of states are broadened in a realistic system due to both finite temperatures and scattering processes, they can be separated, as illustrated in Fig. 2.2(a).

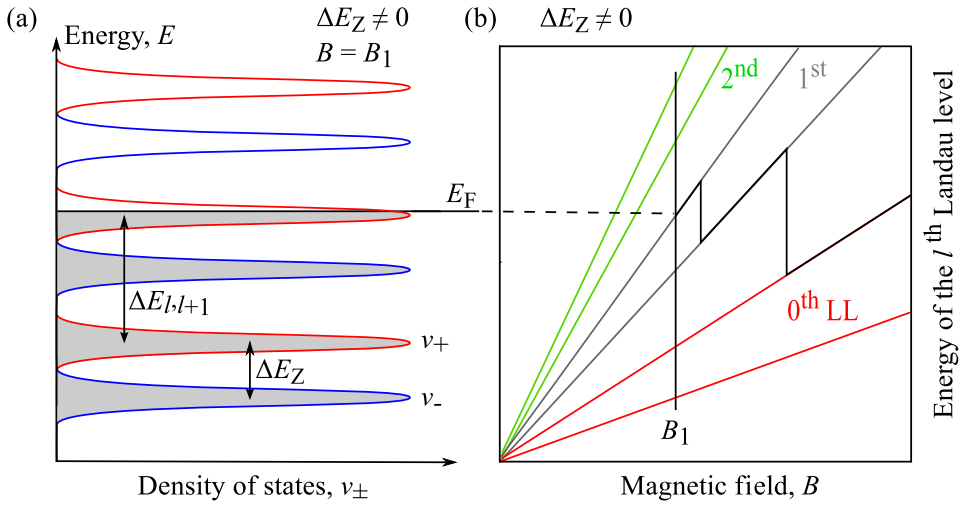

Figure 2.2: (a) depicts a schematic view of density of states $\nu_\pm$ for fixed magnetic field $B = B_1$ with Landau level splitting $\Delta E_{l,l+1}$ and Zeeman splitting ΔE_Z. (b) shows a sketch of spin split Landau levels as a function of B. The magnetic field B_1 and the Fermi energy E_F are marked as black solid lines (adapted from [39]).

The energy of the l-th Landau level can be calculated for a parabolic energy spectrum using the following equation [39]:

$$E_l = \hbar\omega_c(l + \frac{1}{2}) \,, \tag{2.8}$$

with l as an integer number. The energy-related distance between two neighboring Landau levels l and $l \pm 1$ is given by $\Delta E_{l,l\pm1} = \hbar\omega_c$.
The application of a sufficiently strong magnetic field B additionally splits the Landau levels according to the electron spin. This phenomenon is called Zeeman effect, resolving energetically the degenerated spin states in the Landau levels. This difference in energy is given by

$$\Delta E_\mathrm{Z} = g\mu_\mathrm{B}B, \tag{2.9}$$

with the Landé factor g of the material and the Bohr magneton μ_B [39]. Taking into account the Zeeman splitting, the number of carriers on each spin split Landau level is given by $n_\mathrm{LL} = |e|\,B/h$, see Ref. [39]. The number of filled Zeeman split Landau levels is called filling factor v. When considering an electron gas with a carrier density N_s, the filling factor v is given by [39]:

$$v = \frac{N_s}{n_\mathrm{LL}} = \frac{N_s h}{|e|\,B}\,. \tag{2.10}$$

For a fixed carrier density N_s, the Fermi energy E_F oscillates as a function of the applied magnetic field B [39,40] as shown in Fig. 2.2(b). These oscillations of the Fermi energy rely on the density of states $\nu_\pm$ [38]. In an example where the Landau level l is completely filled and the $(l+1)$ level is only partly filled, the Fermi energy E_F lies within the energetically higher $(l+1)$ Landau level, see Fig. 2.2(a). If the magnetic field B is increased, the energy of the $(l+1)$ Landau level rises and is emptied, due to the increasing degeneration of the lower Landau levels. Therefore, the Fermi energy drops back down to the l-th Landau level [38]. This is illustrated in Fig. 2.2(b), which shows the oscillation of the Fermi energy in an ideal system with δ function Landau levels. Beyond that, the oscillations of the Fermi energy E_F result in a changing of the filling factor v. If the magnetic field B is changed, the Landau levels and the connected density of states are shifted through the Fermi energy, resulting in a $1/B$-periodic oscillation. This can also be achieved by varying the Fermi energy and keeping the magnetic field at a fixed value.

Figure 2.2(a) shows that the density of states $\nu_\pm$ at the Fermi energy level E_F varies with changes to the magnetic field B. The density of states is zero when the Fermi energy lies in between two Landau levels, but reaches a maximum when the Fermi energy is in the middle of the broadened Landau level. This oscillation can be directly observed in the longitudinal magneto-resistance R_{xx} of a sample as function of the magnetic field B as illustrated in Fig. 2.3 for an AlGaAs/GaAs quantum well sample at temperature $T = 8\,\mathrm{mK}$ [41]. For magnetic fields $B > \approx 1\,\mathrm{T}$, the resistance starts to oscillate. The minima occur when the Fermi energy E_F lies in between two Landau levels, meaning zero density of states and no free energy states near the Fermi energy, which are necessary for carrier transport. The peaks in the longitudinal magneto-resistance R_{xx} appear when the Fermi energy lies within a Landau level [38]. In this

case, the Landau levels are partly filled and electrons can occupy empty states leading to electron transport. These oscillations of the longitudinal magneto-resistance as a function of the magnetic field are well known as the Shubnikov-de Haas effect. At small magnetic field values ($B < 1\,\mathrm{T}$), the distance between the Landau levels decreases and at a certain magnetic field, the Landau level separation vanishes completely. In this situation, the Fermi energy E_F is always located in a Landau level and has, consequently, no extrema in the density of states and so the resistance stops oscillating [39].

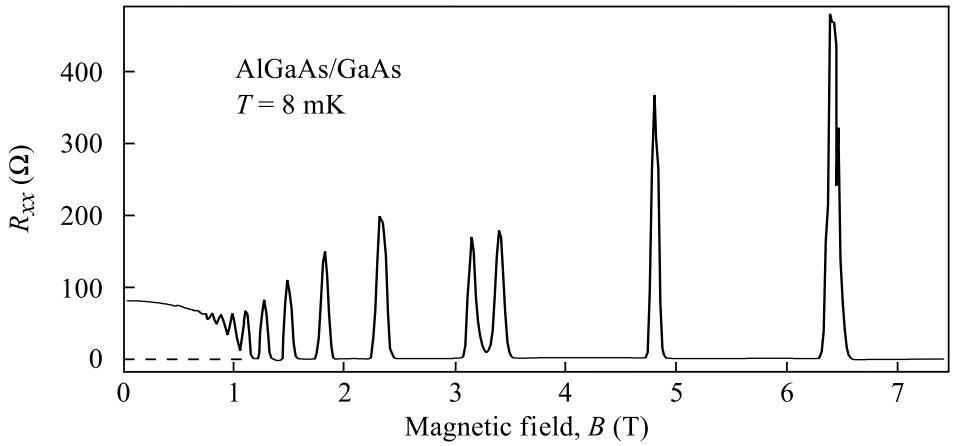

Figure 2.3: Longitudinal magneto-resistance R_{xx} measured in a AlGaAs/GaAs heterostructure at temperature $T = 8\,\mathrm{mK}$ (adapted from [41]).

The oscillating behavior of the longitudinal conductivity σ_{xx} for parabolic bands and evenly spaced Landau levels can be described with the following equation [42, 43]:

$$\sigma_{xx} = \frac{N_s e^2 \tau_f}{m^*} \frac{1}{1+(\omega_c\tau_f)^2} \left(1 - 2\frac{(\omega_c\tau_f)^2}{1+(\omega_c\tau_f)^2}\delta\frac{z}{\sinh z} + \cdots\right), \tag{2.11}$$

The terms δ and z are defined as

$$\delta = \cos\left(\frac{2\pi\mu}{\hbar\omega_c}\right) \mathrm{e}^{\left(-\frac{\pi}{\omega_c\tau_\mathrm{f}}\right)},$$

$$z = \frac{2\pi^2 k_\mathrm{B} T}{\hbar\omega_c},$$

where μ is the chemical potential sufficiently larger than $\hbar\omega_c$ and τ_f represents the zero-field relaxation time.

2.3 Diluted Magnetic Semiconductor

A considerable proportion of the experiments were carried out on (Cd,Mn)Te QW samples, which belong to the group of diluted magnetic semiconductors. Therefore, a short introduction to the inherent characteristics of DMS, as well as their influence on the Zeeman effect, will be given in this chapter.
In DMS structures, paramagnetic ions, e.g. manganese (Mn^{2+}), are implemented into the QW layer during the growth process. In the QW layer, e.g. CdTe, the Cd atoms are randomly replaced by Mn atoms. These Mn atoms induce a magnetic moment which also depends on the concentration $\bar{x}$ of the Mn atoms. In (Cd,Mn)Te QW samples, Mn^{2+} is electrically neutral, as it substitutes Cd^{2+}, but Mn provides a localized spin $S = 5/2$ [44–46]. Due to the magnetic ions (Mn^{2+}), the sample exhibits the giant Zeeman splitting resulting in an enhancement of the effective g-factor [45, 47]. Therefore, Eq. (2.9) has to be modified in the following way:

$$\Delta E_{\mathrm{Z}} = g^* \mu_{\mathrm{B}} B, \tag{2.12}$$

with g^* as the effective g-factor. If the manganese concentration $\bar{x}$ is small ($\bar{x} \approx 0.01$), then the spins of the Mn^{2+}-ions can be considered to be independent from each other. Assuming a small Mn concentration, hence, the effective g-factor g^* is written as

$$g^* = g + \frac{\overline{x} S_0 N_0 \alpha_e}{\mu_{\mathrm{B}} B} \mathcal{B}_{5/2} \left(\frac{5 \mu_{\mathrm{B}} g^*_{\mathrm{Mn}} B}{2 k_{\mathrm{B}} (T_{\mathrm{Mn}} + T_0)} \right) ,$$

with the modified Brillouin function $\mathcal{B}_{S=5/2}$. S_0 and T_0 are phenomenological fitting parameters [46], T_{Mn} is the Mn spin system temperature, $g^*_{\mathrm{Mn}} = 2$ is the Mn g-factor and $N_0 \alpha_e$ is the exchange integral. Taking into account the effective g-factor g^* and substitute it into Eq. (2.12), then the exchanged enhanced Zeeman splitting is given by

$$\Delta E_{\mathrm{Z}} = g \mu_{\mathrm{B}} B + \overline{x} S_0 N_0 \alpha_e \mathcal{B}_{5/2} \left(\frac{5 \mu_{\mathrm{B}} g^*_{\mathrm{Mn}} B}{2 k_{\mathrm{B}} (T_{\mathrm{Mn}} + T_0)} \right) . \tag{2.13}$$

The Brillouin function $\mathcal{B}_{5/2}$ depends on the temperature $T_{\mathrm{Mn}} + T_0$ as well as on the magnetic field B and, thus, ΔE_{Z} depends on these parameters. At low temperatures and high magnetic fields, the normal Zeeman splitting is

smaller than the second term in Eq. (2.13), which is dominated by the Brillouin function. Moreover, the sign of both terms can be opposite, which can lead to an increase or a decrease in the amplitude of ΔE_{Z}. Furthermore, the giant Zeeman splitting is not linear in the magnetic field, a phenomenon that is caused by the Brillouin function. More details are described in Chap. 6.2.

3 Experimental Methods

This chapter is dedicated to the overall experimental setup. The illumination of the sample was achieved with a continuous wave (*cw*) terahertz laser source, as well as with a Gunn diode for radiation in the gigahertz (GHz) frequency range.
For some of the effects studied, it is important to change the polarization state of the radiation. Therefore, different techniques to control the polarization state will be outlined. The final state of the polarization can be described by the Stokes parameters, which will be presented alongside the description of the used waveplates and grid. In the last part of this chapter, the experimental setup with the optical elements and the electrical devices is briefly depicted, including the electrical circuits used in the experiments.

3.1 Optically Pumped Molecular THz Laser

Most of the experiments described in this thesis were carried out on an optically pumped molecular *cw* THz laser system that is not very commonly used and therefore described in more detail here. It is an effective way of creating THz laser radiation. In this system, molecular gases act as active media for the far-infrared (FIR) radiation and a mid-infrared (MIR) CO_2 laser is the source of optically pumping. The following section contains a brief introduction to the physics and characteristics of this monochromatic laser radiation source.

The power of the pump CO_2 laser is $\approx 50\,\mathrm{W}$ in continuous operation mode and is achieved with a longitudinal electrical excitation along the resonator. The electrical excitation populates the first excited state $v = 1$ of the N_2 molecules, which are inserted in the cavity in addition to the CO_2 molecules as shown in Fig. 3.1(a). The energetic level of the excited N_2 and CO_2 molecules are similar and, therefore, due to the collision of both molecules, the energy can be transferred to the CO_2 molecules. The depopulation of this excited state is done by emitting photons in optical transitions via the 9.4 or the $10.4\,\mu$m branch. These wavelength branches belong to two different optical active transitions between vibrational modes of the CO_2 molecule, see Fig. 3.1 (a). Different wavelengths can be selected by changing the position of the resonator grating, because the

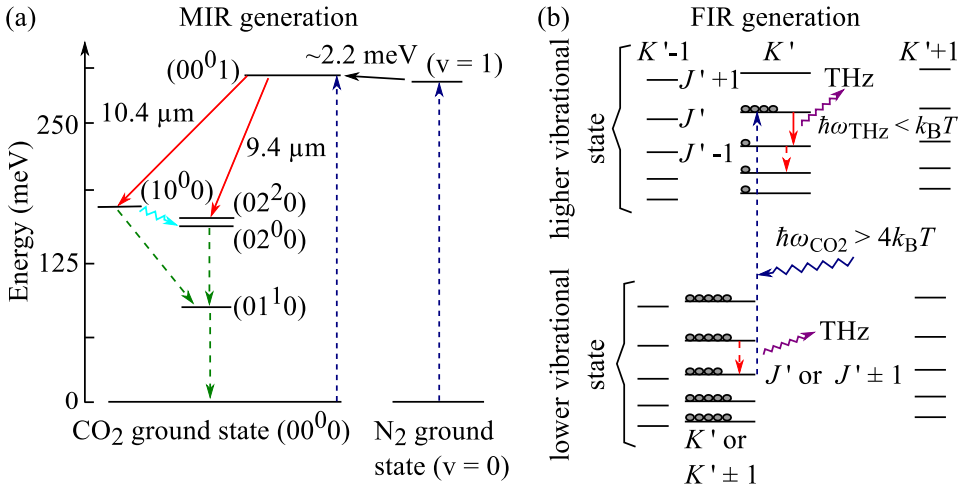

Figure 3.1: Scheme of transitions in the MIR and in the FIR gas laser in (a) and (b), respectively. (a) shows the symmetric (10^00), the antisymmetric (00^01) and the bending vibrational modes (02^20), (02^00) and (01^10) of the CO_2 molecules. The red arrows indicate the optical laser transitions for the wavelengths 10.4 and 9.4 μm. The dashed arrows illustrate the excitation (blue) and the relaxation processes (green). The vertical arrow indicates the energy transfer between the N_2 and CO_2 molecules. The buckled cyan arrow is the Fermi resonance. (b) shows the scheme of the transitions in the FIR range in symmetric top molecules, which are pumped by the CO_2 energy $\hbar\omega_{CO_2}$. The relaxation process happens between the rotational modes within one vibrational state, giving rise to an emission of THz radiation. J and K stand for angular momentum and its projection, respectively (adapted from Ref. [49]).

vibrational modes are rotationally broadened [48, 49]. For a detailed explanation and a closer look at the different modes and transitions, see Ref. [49]. The depopulation of the final states of the optical transitions is achieved with the help of the Fermi resonance and the collision with helium atoms. The output radiation is not used in the experiments, but acts as optical pump source for the FIR gas laser. The pump laser radiation obtained is now guided to a zinc selenide (ZnSe) lens with two planar mirrors. The lens focuses the beam through a polarizing ZnSe Brewster window fixed on a gold-coated steel mirror with a hole and into the cavity of the FIR laser system, as depicted in Fig. 3.2.

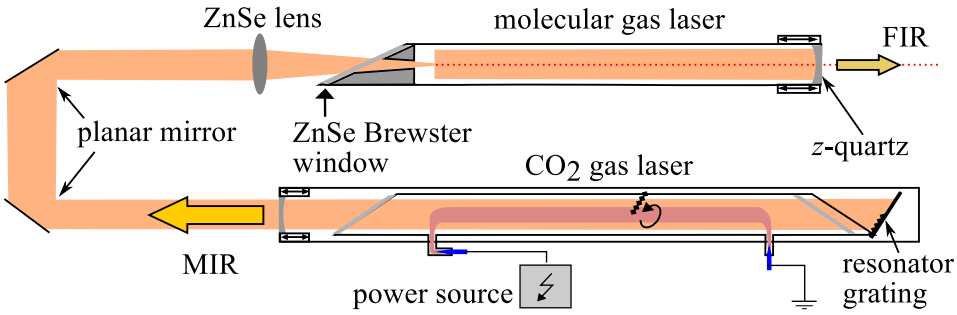

Figure 3.2: Sketch of the CO_2 pump laser generation (MIR) and the optical path to the molecular gas laser with its components. The FIR optical path is illustrated as a red dashed line and the MIR as an orange one (adapted from Ref. [50]).

The strong pump lines of the CO_2 laser excite a vibrational state in the molecules of the FIR gas laser system, which have a permanent electric dipole moment as shown in Fig. 3.1 (b). The inserted gas molecules determine the generated wavelength. For this work, methanol (CH_3OH) was used for the wavelength $\lambda = 118.8\,\mu$m, corresponding to the frequency $f = 2.54\,$THz, the energy $E_{\hbar\omega} = 10.35\,$meV and the output power $P = 90\,$mW. For pumping this methanol wavelength, the CO_2 laser was adjusted to emit the wavelength $\lambda_{CO_2} = 9.695\,\mu$m.

Figure 3.1 (b) shows the vibrational states of an optically pumped symmetric top molecule. J is the angular momentum and K is its projection on the symmetry axis of the molecule. In the case of the vibrational relaxation being sufficiently slow, the emission of far-infrared radiation can occur between the rotational states, as illustrated by the buckled arrows [49]. The dashed arrows are the relaxation processes and the blue arrow pointing upwards stands for the optical pumping transition, induced by the CO_2 laser energy $\hbar\omega_{CO_2}$.

The out coupling window is made out of a silver-coated z-quartz window, which is transparent for THz frequencies but reflects mid-infrared radiation. Therefore, the FIR resonator emits monochromatic radiation. The transverse mode shape of this radiation can be modified by moving the quartz window, resulting in a change of the resonator length.

3.2 Microwave Radiation Generation

The high electron mobility transistor (HEMT) samples were also studied with a second wavelength. This wavelength is 3.14 mm, corresponds to a frequency of 95.5 GHz and was generated by a Gunn diode. These diodes are standard radiation sources based on the Gunn effect as discovered by J.B. Gunn [51]. This effect occurs due to the negative differential resistance [52, 53].
The Gunn diode used in this work emits monochromatic radiation with a radiation power of several milliwatts. However, neither the beam profile nor the effective power on the sample surface could be determined to a satisfactory level of accuracy, meaning all of the data obtained by illuminating the sample with the Gunn diode will be given in arbitrary units.

3.3 Variation of Radiation's Polarization State

The radiation emitted by the laser system - as described in Chap. 3.1 - is linearly polarized, while the polarization of the Gunn diode is circularly polarized[1]. In this thesis, effects were investigated which are highly sensitive to the polarization states of the radiation. Therefore, it is necessary to be able to control the polarization state, as well as to describe these states theoretically. The polarization state of the initial electric field vector $\boldsymbol{E}_\mathrm{i}$ can be changed by applying a $\lambda/2$- or a $\lambda/4$-waveplate for the THz range and a wire grid for the microwave radiation. The theoretical description will now be briefly introduced based on the Stokes parameters.
The $\lambda/2$- and $\lambda/4$-waveplates utilize birefringent medias like, for instance, a x-cut quartz. This quartz includes two different refraction indices n_o and n_{eo} for the plane ordinary and extraordinary axes, respectively [49]. Both indices are wavelength dependent. The difference of the refraction indices $\Delta n = n_o - n_{eo}$ allows one to fabricate $\lambda/2$- or $\lambda/4$-waveplates for a selected wavelength.
The electric field vector $\boldsymbol{E}_\mathrm{i}$ of the linear polarized radiation, which shines normal to the optical axis c (parallel to the extraordinary axis), can be divided into the parallel and perpendicular electric field vector $\boldsymbol{E}_\parallel$ and $\boldsymbol{E}_\perp$, respectively.

[1] achieved by using the device "MI-Wave 284 Series Tapered Mode Transitions", which transforms a linear polarization to a circular one.

They are orientated in relation to the c-axis, which is shown in Fig. 3.3(a). Due to this splitting of the electric field and, therefore, the different propagation velocities for those beams inside the media, a phase shift $\Delta\Phi$ is generated between them. This shift is dependent on the waveplate's thickness d, the orientation in respect to the optical axis and on the wavelength λ. The shift is given by

$$\Delta\Phi = n_0 d - n_{eo} d = \frac{2\pi d}{\lambda}\Delta n.$$

With this equation, it is possible to obtain the thickness d for fabricating waveplates for the requested wavelength λ. The two important cases for this work are the $\lambda/2$-waveplate for rotating the plane of linearly polarized radiation and, secondly, the $\lambda/4$-waveplate to obtain circularly (elliptically) polarized radiation, see Figs. 3.3 and 3.4, respectively.

For the rotation of the linear polarization a $\lambda/2$-waveplate is necessary with a phase shift $\Delta\Phi = (2k+1)\pi$, where k is numbering the order. In this condition, the linear polarization of the final electric field $\boldsymbol{E}_\mathrm{f}$ is rotated by the azimuthal angle α in respect to the initial electric field $\boldsymbol{E}_\mathrm{i}$. The angle α describes the rotation of the polarization and is twice the angle β, which stands for the angle of rotation of the optical axis c as shown in Figs. 3.3(a) and (b). Nevertheless, higher order $\lambda/2$-plates are also possible, but result in thicker plates and therefore in higher absorption of the radiation.

The linear polarization state of the radiation can be described by three Stokes parameters, namely s_0, s_1 and s_2 [54–57]. Therefore, a coordinate system has to be introduced with the xy-plane lying in the waveplate as shown in Fig. 3.3(a). To obtain a coincidence with the sample description, the z-axis directs along the growth direction of the quantum wells and, therefore, against the propagation direction of the radiation. In this system, the rotation of the final linearly polarized electric field vector $\boldsymbol{E}_\mathrm{f}$ can be well described by its two components

E_x and E_y. The rotation can be expressed by the Stokes parameters in the following equations [55, 57]:

$$\begin{aligned} s_0 &= |E_x|^2 + |E_y|^2 = I, \\ s_1 &= \frac{|E_x|^2 - |E_y|^2}{s_0} = \cos(2\alpha), \\ s_2 &= \frac{E_x E_y^* + E_y E_x^*}{s_0} = \sin(2\alpha). \end{aligned} \tag{3.1}$$

Here, s_0 is the polarization independent intensity of the radiation, s_1 is the linear polarization within the x- and y-axis and s_2 is also the linear polarization, but within a 45° rotated coordinate frame of the x- and y-axis.

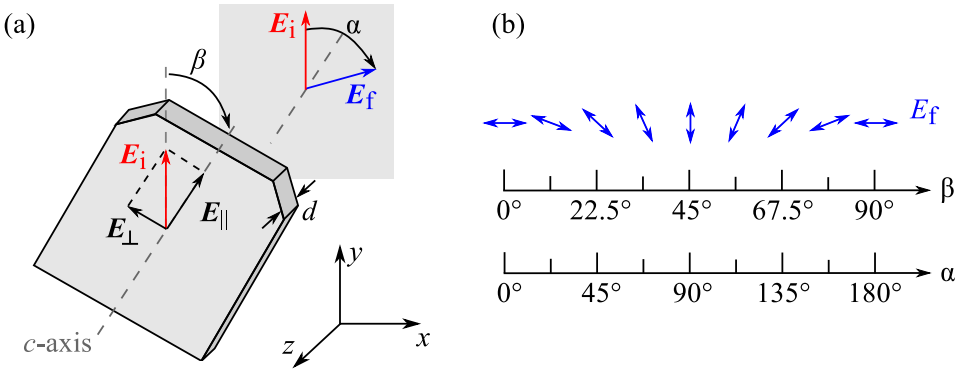

Figure 3.3: (a) shows a schematic sketch of a $\lambda/2$-waveplate with initial polarization state of the incoming radiation $\boldsymbol{E}_\mathrm{i}$. The blue arrow indicates the final polarization state of the radiation $\boldsymbol{E}_\mathrm{f}$ on the sample surface. The thickness of the plate is marked by d. (b) illustrates the state of polarization depending on the rotation angle β of the waveplate and on the azimuthal angle α for the rotation of the radiation (adapted from Ref. [50]).

The circular or elliptical polarization can be obtained by using a $\lambda/4$-waveplate. In comparison to the $\lambda/2$-waveplate, only the thickness of the material d is different. This can be determined by the phase shift $\Delta\Phi = (2k + \frac{1}{2})\pi$. The angle φ describes the rotation of the c-axis in respect to the direction of $\boldsymbol{E}_\mathrm{i}$, see Fig. 3.4(a). If $\varphi = 45° + k \cdot 180°$ and $\varphi = 135° + k \cdot 180°$ then fully right-handed (σ^+) and left-handed (σ^-) circularly polarized radiation is obtained, respectively as shown in Fig. 3.4(b). A further notification is that for the rotation of the plate angle $\varphi = n \cdot 90°$ the initial polarization of $\boldsymbol{E}_\mathrm{i}$ is parallel

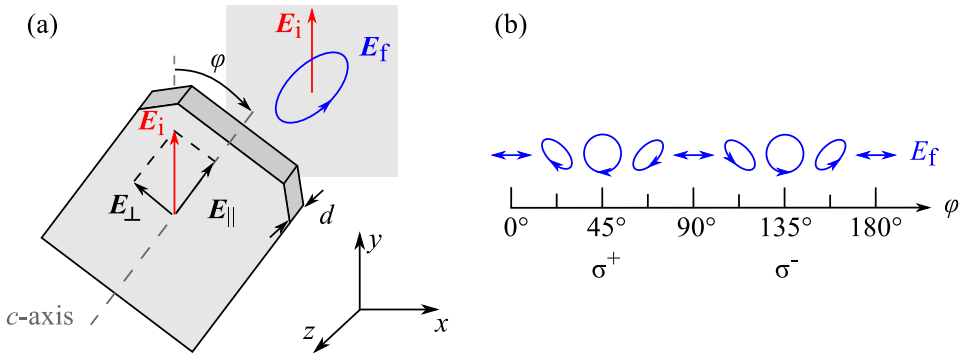

Figure 3.4: (a) shows a schematic sketch of a $\lambda/4$-waveplate with linear polarization of the initial electric field $\boldsymbol{E}_\mathrm{i}$ and final polarization state of $\boldsymbol{E}_\mathrm{f}$. The thickness of the plate is indicated by d. (b) illustrates the state of polarization, depending on the rotation angle φ (adapted from Ref. [50]).

either to the ordinary or to the extraordinary refraction axis. Therefore, the radiation is not influenced by the media concerning its polarization state. Between these angles, the $\lambda/4$-waveplate generates elliptical polarization with a maximum at $\varphi = 22.5° + k \cdot 90°$. The polarization states as function of the rotation angle φ can be expressed by the four Stokes parameters s_0, s_1, s_2 and s_3 [54–57]:

$$\begin{aligned} s_0 &= |E_x|^2 + |E_y|^2 = I, \\ s_1 &= \frac{|E_x|^2 - |E_y|^2}{s_0} = \frac{1 + \cos(4\varphi)}{2}, \\ s_2 &= \frac{E_x E_y^* + E_y E_x^*}{s_0} = \frac{\sin(4\varphi)}{2}, \\ s_3 &= \frac{i(E_x E_y^* - E_y E_x^*)}{s_0} = -P_\mathrm{circ} = -\sin(2\varphi). \end{aligned} \tag{3.2}$$

The circular polarization state of the radiation is described by the fourth Stokes parameter s_3. The minus sign in s_3 stems from the propagation of the radiation against the z-axis direction.

Both λ-waveplates were used for manipulating the polarization state of the THz laser radiation. In the case of microwave radiation, a grid polarizer was used to change the linear polarization of the radiation [49], since no λ-waveplate was available in this frequency range. Figure 3.5(a) shows a grating with the grating

axis g, whilst g^* is the rotated g-axis. The grating axis g is perpendicular to the gate stripes. The initial electric field $\boldsymbol{E}_\mathrm{i}$ and the final electric field $\boldsymbol{E}_\mathrm{f}$ with the corresponding polarization state are also depicted. The azimuthal angle α indicates the rotation of the grid, as well as the rotation of the linear polarization. In Fig. 3.5(b), various states of the linear polarization are shown as a function of the angle α.

The principle of the grating is that it is only transparent for the electric field perpendicular to the lattice stripes, meaning parallel to the g-axis, and is non-transparent for the electric field parallel to them (perpendicular to the g-axis). Therefore, the incoming radiation is disassembled into its two orthogonal parts, $\boldsymbol{E}_\parallel$ and $\boldsymbol{E}_\perp$. Only the $\boldsymbol{E}_\perp$ part of the radiation is transmitted and follows the rotation of the grating. In the worst case, the incoming linearly polarized radiation will completely vanish. Nevertheless, in this work, the Gunn diode emits circularly polarized radiation and, therefore, nearly the same power at all rotation angles α is obtained due to an equal splitting of the incoming circularly polarized radiation.

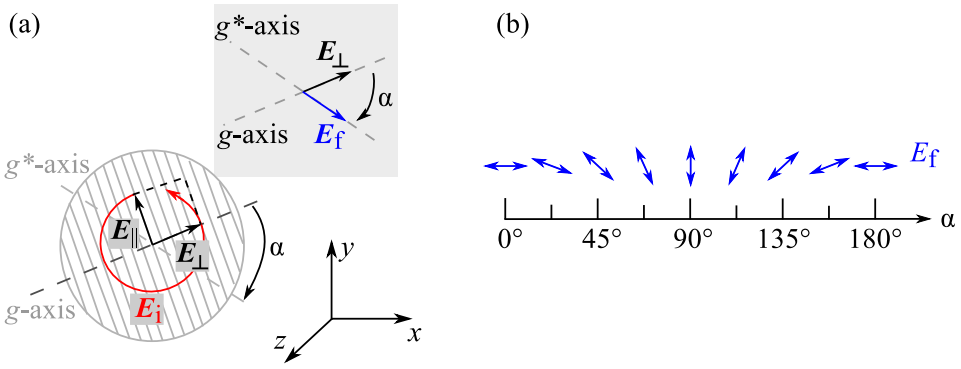

Figure 3.5: (a) shows a schematic sketch of a grating with initial circularly polarized electric field $\boldsymbol{E}_\mathrm{i}$ and the final linear polarization state of the electric field $\boldsymbol{E}_\mathrm{f}$ on the sample surface. The grating axis g and the rotated grating axis g^* are drawn as dashed grey lines. (b) illustrates the state of linear polarization depending on the rotation angle α.

3.4 Experimental Setup

This chapter focuses on the electrical devices, optical elements and the beam path, which are schematically shown in the experimental setup, see Fig. 3.6.

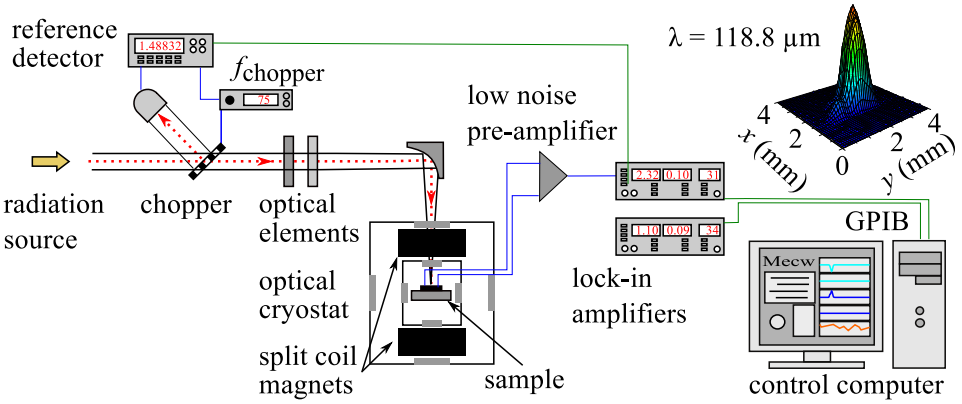

Figure 3.6: A depiction of the optical elements and electrical devices. The radiation path is illustrated as a red dashed line. The devices are named in the picture, but not all connecting wires (blue/ green lines) were drawn from the start of the survey. The top corner shows the beam profile for wavelength $\lambda = 118.8\,\mu$m (adapted from Ref. [50]).

The polarized radiation, illustrated as red dashed line in Fig. 3.6, passes through a tilted chopper with a frequency $f_{\text{chopper}} = 75\,\text{Hz}$ or 625 Hz. The beam is partly reflected into a pyroelectric detector, which is used as a reference detector. This reference signal has two tasks. The first is to stabilize the laser radiation power in the FIR resonator (not shown). The second is to normalize the measured photosignal to the fluctuations of the laser power. The transmitted beam is guided through the optical elements, such as $\lambda/4$- , $\lambda/2$-waveplates or a grid polarizer. These elements can be rotated stepwise to change the polarization state in a controlled way (see Chap. 3.3). Afterwards, the radiation is focused with a parabolic mirror through the windows of the optical cryostat onto the sample surface. The almost Gaussian beam profile of the THz beam was measured with a pyroelectric camera as shown in the right top corner of Fig. 3.6. The sample is mounted between two superconducting split coil magnets, allowing the application of magnetic fields of up to $\pm 7\,\text{T}$ perpendicular to the sample's surface. In the cryostat, the temperature can be varied between room

temperature and $\approx 2\,\mathrm{K}$. The photovoltage generated in the sample is amplified with a low noise pre-amplifier and is detected with a standard lock-in amplifier. The data obtained are processed via the control program, which is based on LabVIEW and records the most important data e.g. the reference signal, the photosignal, the temperature, the magnetic field, etc.
As part of this thesis, experiments with the FIR laser and the Gunn diode were also carried out at room temperature. The setup for the THz laser is the same as for the GHz radiation setup. The Gunn diode has an integrated electrical chopper, which consists of a PIN diode controlled by transistor-transistor logic and, thus, makes the optical chopper redundant. The reference signal was obtained by a beam splitting element in the Gunn diode. For the room temperature measurements, the sample was mounted outside the cryostat but electrically connected in the same way as in the low temperature setup.

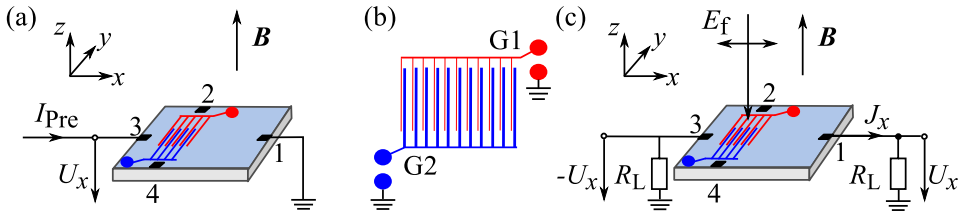

Figure 3.7: Overview of the used measurement geometries. (a) shows the principle circuit for magneto-transport measurements. An alternating current I_{Pre} with a frequency $f = 12\,\mathrm{Hz}$ is applied to the sample. The voltage drop U_x is measured against ground with a lock-in amplifier. The differentially measured voltage U_y in y-direction is not shown. The magnetic field B is applied perpendicularly to the sample surface. In (b) the thinner gate is G1 and the thicker gate is G2. This is illustrated with red and blue fingers, respectively. (c) shows the setup for the photocurrent measurements. The polarized radiation E_{f} irradiates the sample at normal incidence. The magnetic field B is applied perpendicularly to the sample surface. For the photocurrent in (c), both voltage drops $|U_x|$ are measured across a load resistance R_{L} against ground. The same can be done for $|U_y|$ in y-direction, but due to reasons of clarity, this is not shown.

The measurement geometries used will now be briefly introduced. Figure 3.7(a) shows the magneto-transport geometry. The transport measurements were used for the characterization of the samples, see Chap. 4.1.6. Furthermore, magneto-transport measurements on Hall bar samples of the same batch were carried out by Prof. Tomasz Wojtowicz's group[2]. In the measurements carried out in Regensburg, an alternating current I_{Pre} is applied in x-direction of the sample (contacts 1 and 3). The current is in the range of $\approx 50\,\mathrm{nA}$ with a frequency of 12 Hz. The voltage drop U_x over the sample is measured and corresponds to the longitudinal resistance of the sample. The Hall voltage U_y can be measured by connecting contacts 2 and 4 differentially to the lock-in amplifier. These voltages, U_x and U_y, are measured with standard lock-in amplifiers. Afterwards, the longitudinal and the Hall resistance can be calculated based on $R_{xx} = U_x/I_{\mathrm{Pre}}$ and $R_{xy} = U_y/I_{\mathrm{Pre}}$, respectively.
Figure 3.7(b) shows a sketch of the double grating top gate structure, which is fabricated on nearly all sample surfaces used. The thinner gate and the thicker gate stripes are not connected. Therefore, different bias voltages U_{G1} and U_{G2} can be applied to the thinner gate G1 and thicker gate G2, respectively. For a detailed description, see Chap. 4.1.2.
Figure 3.7(c) shows the experimental setup for the photovoltage measurement, which is the measurement mainly used in this thesis. The photosignals under investigation are induced by the electric field E_{f} of the radiation, which irradiates the sample surface under normal incidence. The polarization states of the electric field can be controllable changed (see Chap. 3.3). For the magnetic quantum ratchet effect, a magnetic field is applied perpendicularly to the sample surface. It is to mention that no voltage, except the *dc* bias voltage at the gates, is applied to the samples.
The radiation induced photocurrent J_x is detected by a voltage drop U_x of the same values over two similar load resistances R_{L}. Both voltages are guided to the low noise pre-amplifier, which amplifies differentially. The total photovoltage is given by $U_{\mathrm{total}} = [U_x - (-U_x)]/2$ and is further guided to a lock-in amplifier. In order to obtain the photocurrent J_x, the effective total resistance R_{T} has to be calculated. In the experiments, the load resistance R_{L} is much

[2]Institute of Physics, Polish Academy of Sciences, Al. Lotnikow 32/46 Warsaw, Poland

smaller than the sample resistance R_S ($R_L \ll R_S$). Both resistances are parallel connected and therefore, the total resistance R_T can be calculated as follows:

$$\begin{aligned} R_T &= \frac{R_L \cdot R_S}{R_L + R_S} \text{ with } R_L \ll R_S \\ R_T &\approx \frac{R_L \cdot R_S}{R_S} \approx R_L. \end{aligned} \tag{3.3}$$

Therefore, the voltage drop is directly proportional to the generated photocurrent and does not feel any extra influence of the sample resistance.
In the calculations, the signal obtained was normalized on the reference signal of the radiation to reduce the influence of the variations of the radiation power. The reference signal was obtained coincident with the photocurrent signal and was calibrated with a power measurement before the experiments.

4 Sample Preparation and Characteristics

The magnetic quantum ratchet effect was observed and investigated in CdTe/CdMgTe and (Cd,Mn)Te/CdMgTe QW samples with a dual grating gate (DGG) superlattice on top of the quantum well structures. Therefore, a brief outline of the wafer growth, the fabrication of the DGG superlattice, the soldering of the ohmic contacts and the characterization of the samples will be given in the following.
Additionally, this thesis also investigates the ratchet effect as detector, which was observed in similar top gate structures as in the MQRE samples, but on high electron mobility transistors. A short overview of the InAlAs/InGaAs/-InAlAs/InP HEMT sample growth, the processing of the superlattice and the sample characteristics will be provided here.

4.1 CdTe and (Cd,Mn)Te Samples

Firstly, the wafer growth of the CdTe and (Cd,Mn)Te samples, which were conducted by Prof. Tomasz Wojtowicz's group will be briefly introduced. As far as the ratchet effects under investigation are concerned, the dual grating top gate superlattice is of importance; hence the processing steps for fabrication will be introduced. These steps involve the design, the electron beam lithography (EBL), the evaporation of the gate material and the lift-off process of the unnecessary material. All of the methods used in the fabrication of the DGG are standard procedures in semiconductor wafer processing. Therefore, they will be only briefly introduced, as many authors have explained and discussed these methods in detail (refer to, for example, Refs. [58–60] for more details). The last step in the fabrication of samples is to solder the ohmic contacts. The characterization of the samples is given in the final section.
The explanations and methods for the preparation of the DGG will be explained through the example of (Cd,Mn)Te sample #1, see Tab. 1. All other CdTe and (Cd,Mn)Te samples, except sample #4, are produced in the same way. The detailed recipes for each processing step of the superlattice and the fabrication of the ohmic contacts can be found in the Appendix.

4.1.1 Sample Growth

The double grating top gate superlattice is fabricated on (Cd,Mn)Te/CdMgTe and CdTe/CdMgTe single QW structures, which were grown by molecular beam epitaxy on (001)-oriented GaAs substrates [37,47,61–64]. The schematic design of the layer structure and sketches of the QWs can be found in Figs. 4.1(a)-(c), respectively.
A thick buffer layer of 6 μm consisting of CdTe and $Cd_{0.76}Mg_{0.24}Te$ layers was grown on top of the (001)-GaAs substrate, followed by a short period of superlattices made of CdTe/$Cd_{0.76}Mg_{0.24}Te$ as shown in Fig. 4.1(a). These layers were grown to reduce the number of dislocations due to the large lattice mismatch between the GaAs substrate and the $Cd_{0.76}Mg_{0.24}Te$ layer. The QW width for both wafers is 9.7 nm and the QW is embedded between two barriers of $Cd_{0.76}Mg_{0.24}Te$ alloys. The top side barrier is 10 or 15 nm thick, corresponding to (Cd,Mn)Te/CdMgTe or CdTe/CdMgTe QWs, respectively. On top of this barrier, a doped layer was grown, which is 5 nm thick and is composed of CdMgTe:I. In this layer, iodine acts as an electron donor for modulation doping of the 2DEG. To protect the doped region, a cap layer of 50 or 75 nm thickness was grown for either (Cd,Mn)Te/CdMgTe or CdTe/CdMgTe QWs, respectively.

Figures 4.1(b) and (c) illustrate the cross-section of the QWs for (Cd,Mn)Te and CdTe, respectively. The (Cd,Mn)Te/CdMgTe wafer has a single QW consisting of (Cd,Mn)Te compound, while CdTe/CdMgTe structures have a nonmagnetic CdTe QW. The (Cd,Mn)Te QW has two evenly spaced $Cd_{0.8}Mn_{0.2}Te$ layers inserted during the growth process, which are separated by CdTe layers. The $Cd_{0.8}Mn_{0.2}Te$ layers are three monolayers thick and the CdTe layers are eight monolayers thick as shown in Fig. 4.1(b).
In the QW layers of (Cd,Mn)Te, the Cd atoms are exchanged by Mn atoms, which carry a localized spin $S = 5/2$. This leads to an increase of the effective g^*-factor of the band carriers and therefore to an enhanced Zeeman splitting ΔE_Z as discussed in Chap. 2.3. For proofing the increased Zeeman splitting ΔE_Z, magneto-photoluminescence studies were performed in a previous work in which the same wafer material was used, see Ref. [64]. These measurements show a strong red-shift with increasing magnetic field. From these measure-

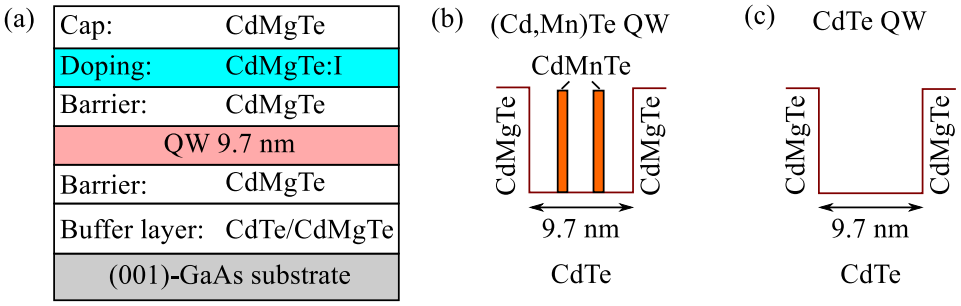

Figure 4.1: (a) shows a schematic overview of the layer sequences for (Cd,Mn)Te/CdMgTe and CdTe/CdMgTe QWs. The QW is embedded between two barriers of CdMgTe and additionally modulation doped by iodine donors in the doping region on the top side of the wafer. In (b) the sketch of the (Cd,Mn)Te/CdMgTe QW is depicted. The two red bars represent evenly spaced (Cd,Mn)Te layers, which are inserted in the QW between CdTe layers. In (c), the QW for the CdTe wafer is illustrated. Both QWs have the same width of 9.7 nm.

ments, it is possible to extract the average Mn concentration in the digital alloy $\overline{x} = 0.015$, as well as the Fermi energy $E_F = 1.6\,\text{eV}$ from the linewidth.

4.1.2 Structure Design

Before fabricating the dual grating gate superlattice, the layout with the parameters has to be prepared. Therefore, it is necessary to define the location on the sample surface, the width and spacing of the separated gate stripes and their period. A sample with both, a region with a DGG and a region without as reference, is required to compare the photosignals observed that are induced by the DGG and by the untouched surface. Thus, the location of the DGG was fixed at the left side of the sample, as shown in Fig. 4.2(a). The sample sizes vary between $4 \times 10\,\text{mm}^2$ and $4 \times 4\,\text{mm}^2$. In the smaller samples, there is no ungated area large enough to serve as reference.
As discussed in Chap. 2.1, the ratchet effect occurs in asymmetric top gate structures; therefore, the DGG consists of two different thick gate stripes - G1 and G2 - which are separated from each other by different distances in x-direction. The cross-section of the DGG superlattice on top of the QW

structure is depicted in Fig. 4.2(b). The source and drain contacts correspond respectively to the points 3 and 1 in Fig. 4.2(a) and are oriented perpendicular to the gate stripes (along the x-axis). The contacts for measuring parallel to the gate stripes (in y-direction) are 2 and 4. The width of the thinner stripes (G1) is $d_1 = 1.7$ or $1.85\,\mu$m and the thicker stripes (G2) always have the same width, namely $d_2 = 3.7\,\mu$m (see Tab. 1 and Ref. [37]). To further increase the asymmetry of the superlattice, the spacing between the gate stripes is around $a_1 = 2.8\,\mu$m and $a_2 = 5.6\,\mu$m. Only one structure with $\approx 20\%$ larger spacing, namely $a_1 = 3.5\,\mu$m and $a_2 = 7.0\,\mu$m, was fabricated to clarify the influence of different scaled DGG on the ratchet effect. The asymmetric superlattice consists of a repetition of N - between 56 and 65 - times the period $d = d_1 + d_2 + a_1 + a_2$, see Tab. 1 and Refs. [22,28,37,65]. This results in a total length l, which varies between 875 and $905\,\mu$m. The total area covered can be estimated by $w_2 * Nd$, with w_2 as the overlap length of the two different thick gate stripes. The overlap is in the order of $450 - 600\,\mu$m as shown in Fig. 4.2(c) and Tab. 1.

The double grating gate stripes consist of 25 or 30 nm thick gold stripes, except sample #4, for which the DGG structure consists of a 75 nm thick dysprosium layer and a 15 nm gold cover layer. The chosen gold stripe thicknesses are almost transparent for the THz radiation used. This was experimentally proved applying photoconductivity measurements and comparing the photosignals of a free area and an area covered by gold of different thicknesses. For the gold thickness of 25 nm, being relevant for the studied DGG structures, the reduction of the signal was about 10% to 20% whereas for gold of 85 nm thickness, the signal is nearly completely suppressed. Taking into account the skin depth of gold which is in the range of 50 nm for the frequency $f = 2.54$ THz [66], these measurements demonstrate that the electric field reduction is negligible for the layer thickness smaller than 50 nm which is the case in this thesis.

As outlined, the thinner and thicker gate stripes do not touch each other. To be able to apply the same voltage to all stripes of G1 or G2, a horizontal gold stripe interconnects the single stripes; see the sample picture in Fig. 4.2(c).

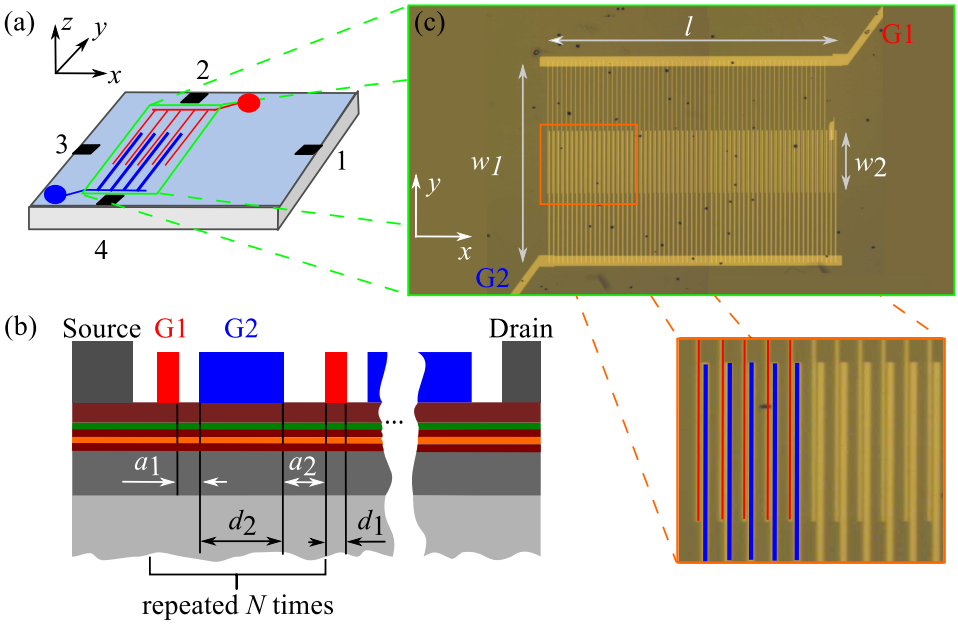

Figure 4.2: (a) shows a sketch of the entire sample with superlattice position and its gate contacts (red and blue). The ohmic contacts are marked as black squares and numbered from 1-4. The cross-section of the DGG superlattice, which is deposited on top of the QW structure, is shown in (b). The grating fingers have two different widths, d_1 and d_2 and are separated by the spacing a_1 and a_2. This period $d = d_1 + d_2 + a_1 + a_2$ is repeated N times, resulting in a total length l, see Tab. 1. (c) depicts a photograph of the double grating gate structure and a zoom in to render the gate stripes visible. The thinner stripes, G1, are highlighted with red stripes and the thicker ones, G2, with blue (adapted from [37]).

4.1.3 Electron Beam Lithography and Optical Lithography

The design of the DGG superlattice is transferred to the sample surface by the electron beam lithography or the optical lithography. The superlattice on top of the CdTe and (Cd,Mn)Te QW structures were created by the EBL process, while T. Otsuji's group[3] fabricated the structure by combining the EBL process for the thinner stripes and the optical lithography for the thicker gate stripes for the DGG HEMT samples. Both lithographies are based on the

[3]Research Institute of Electrical Communication, Tohoku University, Sendai, Japan

Sample	#1	#2	#3	#4	#5	#6	#7
material	CdMnTe	CdMnTe	CdMnTe	CdMnTe	CdTe	CdTe	CdTe
Au	25 nm	25 nm	30 nm	15 nm	25 nm	25 nm	30 nm
Dy	-	-	-	75 nm	-	-	-
d_1 (μm)	1.85	1.85	1.7	1.7	1.7	1.85	1.7
a_1 (μm)	2.8	3.4	3.5	2.8	2.8	2.8	2.8
d_2 (μm)	3.7	3.7	3.7	3.7	3.7	3.7	3.7
a_2 (μm)	5.6	5	7	5.8	5.8	5.6	5.8
d (μm)	13.95	13.95	15.9	14	14	13.95	14
l (μm)	905	905	880	875	875	905	880
N	65	65	56	63	63	65	63
w_1 (μm)	600	600	450	450	450	600	450
w_2 (μm)	200	200	350	350	350	200	350

Table 1: Samples with a DGG superlattice on top of CdTe and (Cd,Mn)Te QWs structures. The parameters are described and schematically sketched in Fig. 4.2 (adapted from Ref. [37]).

same principle, which will be briefly introduced in the following section.
On the one hand, the information about the design of the superlattice, e.g. the size and the position of the stripes, the dose of the beam intensity, etc., is load into a program which controls the electron beam in the EBL process. On the other hand, the optical lithography uses a mask, in which the structure has already been etched and, therefore, cannot be varied anymore. In order to write the DGG superlattice - either with the EBL or the optical lithography - the sample surface has to be spin coated with a suitable resist, e.g. polymethylmethacrylate (PMMA) for the EBL processing.
In the EBL, the program controllable moves the electron beam to write the structure into the resist. The dose of the beam intensity defines how long the beam remains in the same position to irradiate the resist down to the surface. For the optical lithography, the exposure time is the critical value to fully illuminate the resist. Consequently, it is necessary to know the thickness of the resist, otherwise the structure cannot be transferred to the surface. The irradiation of the resist by the electron beam or the ultra violet light in the optical lithography triggers a chemical reaction in the resist. This reaction

breaks the long chained PMMA molecules, which can be dissolved in a further step [67, 68]. The remaining - not irradiated - areas are insoluble and stay on the sample surface surrounding the DGG structure.

4.1.4 Thermal Evaporating and Lift-off

After the lithography process, the sample surface is only partly covered with a resist. The residual areas are clean and define the DGG structure. The defined superlattice is thermally evaporated by the selected top gate material, e.g. Au or Dy/ Au as used in this thesis. During the evaporation process both the desired structure and the remaining resist are covered. To obtain the DGG, the resist with its Au or Dy/Au covering is removed in a lift-off step, whereby the sample is put in an acetone bath for several hours at temperature $T = 60°\mathrm{C}$. The acetone only removes the resist and, with it, the Au or Dy/Au covering, meaning only the defined DGG superlattice remains on the sample surface after the bath.

4.1.5 Ohmic Contacts

Ohmic contacts are necessary to perform photocurrent and magneto-transport measurements. Therefore, several pairs of electrical contacts to the 2DEG were prepared, as shown in Fig. 4.2(a). In this sketch, the black squares are the contact pads. They were made as pairs to measure parallel (J_y, 2-4) and perpendicular (J_x, 1-3) to the double grating gate.
It is commonly known that a metal on top of a semiconductor surface normally results in a Schottky barrier. This barrier has a nonlinear non-ohmic current-voltage behavior. Schottky contacts also have a rectifying characteristic and are, therefore, not suitable for any *ac* measurements. In his diploma thesis, C. Betthausen studied, among other things, various methods of fabricating ohmic contacts to a CdTe 2DEG, see Ref. [69]. Based on his research and descriptions contained within Betthausen's work, the ohmic contacts were consequently made by soldering indium contacts to the 2DEG.
First, the oxide layer on top of the sample surface has to be removed, which is achieved by scratching the surface several times with a needle. Afterwards,

the cut surface of a small indium piece, which was cut off a bigger piece only a short time before, is pressed onto the scratched area. The piece was cut to break the oxide layer on the indium surface and within this short time period, a In_2O_3 oxide layer can hardly grow again which would prevent ohmic contacting. Next, the indium pad is soldered for approximately seven seconds. Good thermal contact between the soldering iron and the indium dot is crucial and can be improved by covering the soldering iron tip with some indium. This procedure results in an ohmic contact characteristic. If not, the contact can be heated for another three seconds with the soldering iron.
The ohmic contacts were tested for their current-voltage characteristic on a point probe station and for many samples; a room temperature resistance between 10 kΩ and 120 kΩ was obtained. A crucial behavior is that the resistance can either increase or decrease after cooling the sample to liquid helium temperature. At the time of writing, there is no known explanation for why some contacts improve and some decline in quality.

4.1.6 CdTe and (Cd,Mn)Te Quantum Well Characterization

The sample characterization was done with magneto-transport measurements, meaning the Shubnikov-de-Haas (SdH) oscillations and, further, the quantum Hall plateaus will be presented. The measurements were performed in a two-point geometry on rectangular shaped samples with a double grating gate superlattice as shown in Fig. 3.7(a). The SdH oscillations and the quantum Hall effect (QHE) for an exemplary (Cd,Mn)Te and CdTe sample are shown in Figs. 4.3(a) and (b), respectively. Note here, that the QHE in sample #1 does not solely have plateaus; it also has some peaks. This is due to the influence of the SdH oscillations on the QHE which can occur when the x- and y-direction of the contacts are not perpendicular to each other in the two-point measurement geometry.
The amplitudes of the SdH oscillations increase with the raising of the magnetic field B in CdTe structures, but in the (Cd,Mn)Te sample a beat-like pattern occurs at $B > 4.5\,\mathrm{T}$, see Fig. 4.3. These beatings are common in diluted magnetic semiconductors structures like (Cd,Mn)Te and are explained in more detail in Chap. 2.3. The density of the two-dimensional electron gas n_e and

QW material	n_e (cm^{-2})	μ (cm^2/Vs)
(Cd,Mn)Te/CdMgTe	6.6×10^{11}	9.5×10^3
CdTe/CdMgTe	4.2×10^{11}	65×10^3

Table 2: Sample parameters: electron density n_e and electron mobility μ for two different QW structures, (Cd,Mn)Te/CdMgTe and CdTe/CdMgTe, at $T = 4.2\,\mathrm{K}$.

the electron mobility μ for both QW structures at liquid helium temperature $T = 4.2\,\mathrm{K}$ are summarized in Tab. 2 and Ref. [37].

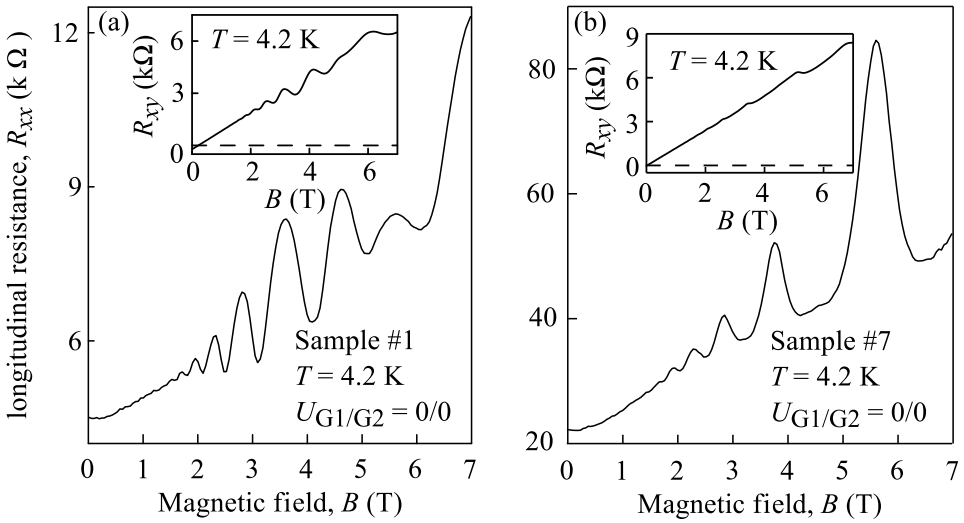

Figure 4.3: Magneto-transport experiments performed at temperature $T = 4.2\,\mathrm{K}$ in (Cd,Mn)Te and CdTe structures in (a) and (b), respectively. Both samples are rectangular shaped with a DGG superlattice. The insets in (a) and (b) show the Hall resistance for the corresponding samples at $T = 4.2\,\mathrm{K}$ (adapted from Ref. [37]).

Further magneto-transport measurements for sample #1 at liquid helium temperature are shown in Fig. 4.4. This figure presents the longitudinal magnetoresistance R_{xx} for different gate voltage combinations ($U_{\mathrm{G1/G2}} = 0/0$, $U_{\mathrm{G1/G2}} = -0.5/0\,\mathrm{V}$ and $U_{\mathrm{G1/G2}} = 0/-0.5\,\mathrm{V}$). Figure 4.4 reveals that the application of the gate voltages has no considerable influence on the period of the $1/B$-oscillations in R_{xx}. This is caused by the fact that the DGG superlattice only

covers a small area of the whole sample [37]. The inset in Fig. 4.4 shows the gate voltage dependence of R_{xx}. The dependencies are measured by sweeping the potential on one gate U_{G1} (U_{G2}) while the other gate U_{G2} (U_{G1}) was held at zero bias voltage. The results are obtained for a fixed magnetic field $B = 3.9\,\mathrm{T}$. The influence of gate G1 (U_{G1}) on R_{xx} is negligible; the second gate (U_{G2}), on the other hand, leads to an increase of the resistance of $\approx 12\%$ at $U_{G2} = -0.5\,\mathrm{V}$ [37].

The overall characteristic of the results for different cool down processes is the same but the value of the resistance increase can vary on the gate voltage scale by $\pm 0.1\,\mathrm{V}$. The reason for this is attributed to the trapping of the charges in the insulator, which is cooldown dependent [37].

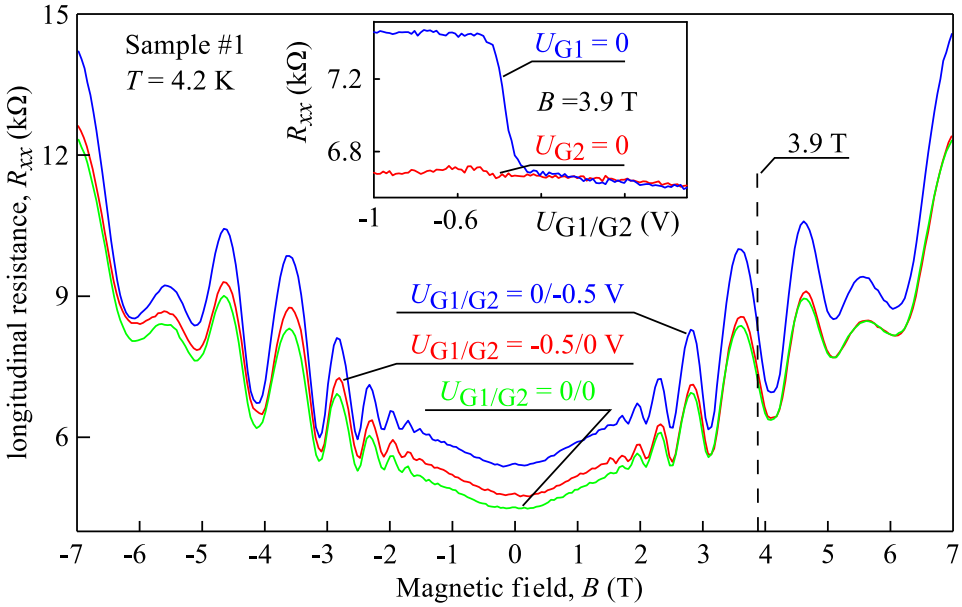

Figure 4.4: Magneto-transport data obtained at temperature $T = 4.2\,\mathrm{K}$ in (Cd,Mn)Te sample #1. The green line shows the data for the gate voltage combination $U_{G1} = 0$ and $U_{G2} = 0$; the red one for $U_{G1} = -0.5\,\mathrm{V}$ and $U_{G2} = 0$; and the blue line for $U_{G1} = 0$ and $U_{G2} = -0.5\,\mathrm{V}$. For clarity, they are simplified as $U_{G1/G2} = 0/0$, $U_{G1/G2} = -0.5/0\,\mathrm{V}$ and $U_{G1/G2} = 0/-0.5\,\mathrm{V}$, respectively. The inset shows the longitudinal resistance R_{xx} as a function of the applied gate voltage U_{G1} (U_{G2}) measured for $U_{G2} = 0$ ($U_{G1} = 0$) at $B = 3.9\,\mathrm{T}$, indicated by the vertical dashed line (adapted Ref. [37]).

As a side note, it should be mentioned that the fabrication of such large-size superlattices is challenging. Some of the structures listed in Tab. 1 have minor imperfections, which can be observed through an optical microscope. These imperfections are caused by occasional inhomogeneities of the PMMA layer. Consequently, the EBL beam was unable to write the exact structures as intended. This could, thereby, result in the metal fingers overlapping after the thermal evaporation, causing short circuits and leading to the destruction of a few gate fingers. The latter occurs in the lift-off process when the metal stripes cannot be separated from the surrounding material and are, therefore, also removed with the unnecessary metal. The short circuits can also be caused by surface impurities, which are covered by gold, but were not supposed to be part of the superlattice.

4.2 High Electron Mobility Transistor Samples

The helicity sensitive ratchet effect was observed in InAlAs/InGaAs/InAlAs/ InP high electron mobility transistors with doubly interdigitated grating gates. The superlattice design is similar to the CdTe/CdMgTe and (Cd,Mn)Te/ CdMgTe samples as shown in Chap. 4.1.2 but the HEMT samples were fabricated by the group of T. Otsuji. Consequently, only the parameter of the superlattice will be described. The sample growth and characterization will also be briefly introduced.

4.2.1 Sample Growth

The layer sequence of the HEMT samples is sketched in Fig. 4.5(a). The sketch shows the cross-section of the different layers with their corresponding thicknesses.
The HEMT structure is grown on a (001)-grown semi-insulating InP substrate, which is doped with iron (Fe). The substrate resistivity is $\approx 5 \times 10^7\,\Omega$cm and has a thickness of 600 μm. On top, an $In_{0.52}Al_{0.48}As$ layer was grown to a height of 100 nm to overcome the lattice mismatch between the substrate and the undoped composite channel layers. The channel layer sequence consists of $In_{0.53}Ga_{0.47}As/In_{0.70}Ga_{0.30}As/In_{0.53}Ga_{0.47}As$ with 5, 8 and 3 nm thickness, respectively. The QW is formed between the composite channel and a carrier-supplying layer. The carrier supplying layer includes three layers of $In_{0.52}Al_{0.48}As$ with different thicknesses, namely 3, 5 and 15 nm. The mid-level $In_{0.52}Al_{0.48}As$ layer has a Si-doping to increase the carrier density in the 2DEG. The structure is finished with a cap layer consisting of a 6 nm thick insulating InP film [70].
The ohmic contacts to the 2DEG were made in a non-alloyed way. The composition of the source/drain contacts consists of Si-doped $In_{0.52}Al_{0.48}As$ and a doped film of $In_{0.53}Ga_{0.47}As$ with a thickness of 15 nm for both layers. The contact surface is protected against oxidation with a gold covering [71].

(a)

Cap	InP	6 nm
Carrier-supplying	$In_{0.52}AlAs$	15 nm
	$In_{0.52}AlAs$:Si	5 nm
	$In_{0.52}AlAs$	3 nm
Quantum Well at heterointerface		
Composite channel	$In_{0.53}GaAs$	3 nm
	$In_{0.70}GaAs$	8 nm
	$In_{0.53}GaAs$	5 nm
Buffer layer	$In_{0.52}AlAs$	100 nm
(001) semi-insulating	InP:Fe	~0.6 mm

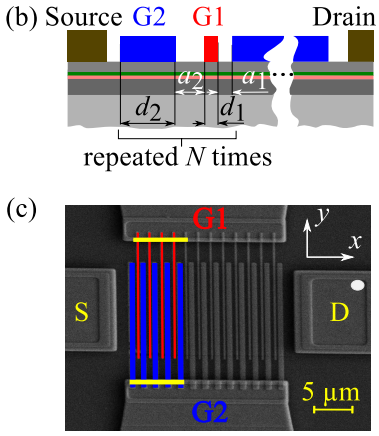

Figure 4.5: (a) shows a sketch of the layer sequence and the thickness of each layer. In (b), the cross-section of the sample with the double grating gate superlattice is depicted. The grating fingers have two different widths, d_1 and d_2, and are separated by spacing a_1 and a_2. The period $d = d_1 + d_2 + a_1 + a_2$ is repeated to obtain an active area of about $400\,\mu m^2$. An overview of the parameters is given in Chap. 4.2.2. (c) shows a photograph of the sample structure. The source and drain contacts are named S and D, respectively. The thinner stripes, G1, are highlighted with red stripes and the thicker ones, G2, with blue (adapted from Ref. [70]).

4.2.2 Fabrication of Double Interdigitated Grating Gates

The double interdigitated grating gates have a similar design to the DGG superlattice in CdTe and (Cd,Mn)Te QW samples. Therefore, only a brief summary of the parameters will be given.

The thinner gate stripes, G1, were written in an EBL process, whereas the thicker gate stripes, G2, were realized by optical lithography. The stripes are formed of 65 nm-thick Ti/Au/Ti layers in a standard lift-off process [70]. The width of the stripes, d_1 and d_2, and the spacing between them, a_1 and a_2, are illustrated in Fig. 4.5(b). In all HEMT samples studied, the grating gate fingers G1 and G2 have the width $d_1 = 200\,nm$ and $d_2 = 800\,nm$, respectively. Equally, the asymmetric spacing between the fingers is the same for each sample, namely $a_1 = 200\,nm$ and $a_2 = 400\,nm$. The size of the active area covered by the grating is about $20\,\mu m \times 20\,\mu m$ [70].

4.2.3 HEMT Sample Characterization

Just as the fabrication of the HEMT samples, the characterization was done by the group of T. Otsuji [70]. The 2DEG of the InAlAs/InGaAs/InAlAs/InP QW structure has an electron density of $\approx 3 \times 10^{12}\,\mathrm{cm}^{-2}$ and the effective electron mass is $m^* = 0.04\,m_0$, with the free-electron mass m_0. The Hall mobility μ_0 was measured with a non-contact Hall measurement at room temperature [72] and is in the order of $\mu_0 = 11500 \pm 500\,\mathrm{cm}^2/\mathrm{Vs}$ [70].
A typical characteristic of a transistor is that, with increasing gate voltages, the depletion zone increases and, therefore, the current is cut off. This characteristic can be seen in the current-voltage-measurement of the sample HEMT #1 in Fig. 4.6. The source-drain current I_{SD} is close to zero for the gate voltage $U_{\mathrm{G1}} < -1.2\,\mathrm{V}$ and for the second gate voltage $U_{\mathrm{G2}} = 0$. Due to Ohm's law, the current-voltage-characteristic can also be shown in a resistance measurement. The resistance R_{SD} between the source and drain contact is shown as dependency of the gate voltage U_{G1} (U_{G2}) for zero bias at the other gate U_{G2} (U_{G1}) in the inset of Fig. 4.6. Here, the resistance increases when increasing bias voltages are applied to the gates. The vertical dashed line at $U_{\mathrm{G2}} = -1.2\,\mathrm{V}$ indicates the breakdown voltage limit of the transistor. The voltage limit for U_{G1} is at $-1.4\,\mathrm{V}$.

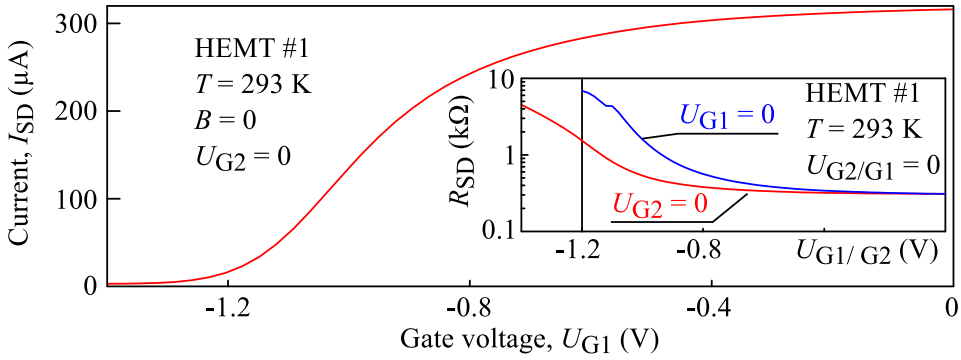

Figure 4.6: Current I_{SD} between drain and source contacts as a dependence of the gate voltage U_{G1} for $U_{\mathrm{G2}} = 0$ at room temperature $T = 293\,\mathrm{K}$. Inset shows the resistance R_{SD} in a logarithm scale as a function of the gate voltage U_{G1} (U_{G2}) measured for $U_{\mathrm{G2}} = 0$ ($U_{\mathrm{G1}} = 0$). The vertical dashed line indicates the breakdown voltage limit for U_{G2} (adapted Ref. [70]).

5 Ratchet Effect at Zero Magnetic Field in (Cd,Mn)Te QWs

The ratchet effect was researched at zero magnetic field in (Cd,Mn)Te QW superimposed with an asymmetric lateral dual grating gate superlattice. It will be demonstrated that the ratchet effect is sensitive to variations of the applied gate potentials as well as to the different polarization states of the incident radiation. In detail, this means that, by changing the gate voltages or the polarization, the ratchet current can change its amplitude and sign. To explain this behavior, the ratchet theory introduced in Chap. 2.1 will be considered and adjusted to the experiment. Most results presented in this chapter are published in Ref. [37].

5.1 Experimental Results and Discussion

A photocurrent is observed when the double grating gate superlattice is irradiated under normal incidence with a radiation frequency $f = 2.54\,\mathrm{THz}$. This current is measured perpendicular to (x-direction) and along (y-direction) the stripes, see Fig. 5.1, showing the photocurrents J_x/P and J_y/P, which are normalized to the radiation power P, to be a function of the azimuthal angle α. For better comparison, the current J_y/P is multiplied by a factor of -10. It can be seen that the overall behavior of both photocurrents is very similar but the magnitude of the current in y-direction is about 10 times smaller than that in x-direction. Therefore, only the data for J_x/P will be presented for sample #1. The observation of these currents is already a first indication that the photoresponse is generated due to the superlattice. This assumption is based on the well-known fact that a photosignal can only be detected under oblique incidence in (001)-oriented QW structures [47, 64]. As shown in Fig. 5.1, the current consists of the polarization independent and a polarization dependent contribution. The latter contribution varies upon changing the direction of the linearly polarized electric field vector in respect to the gate stripes by the azimuthal angle α. The polarization is orientated perpendicular to the gate

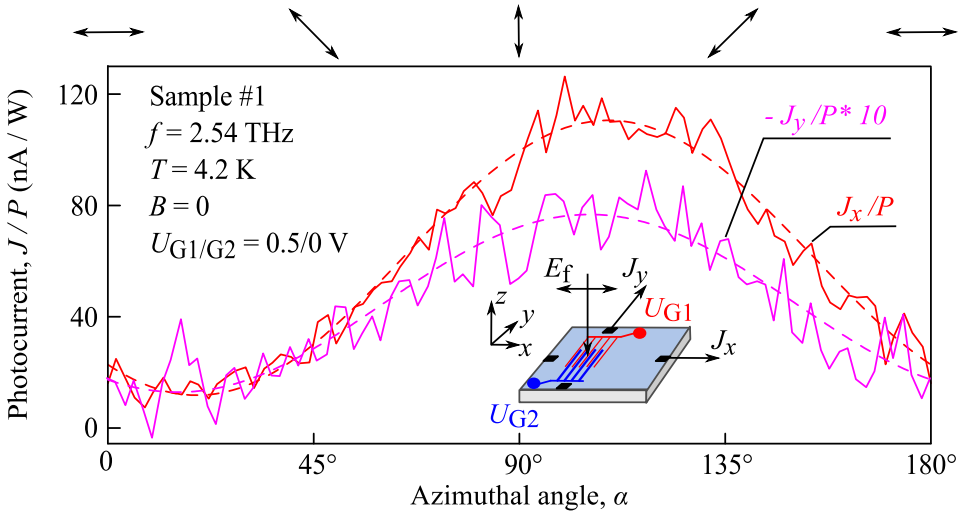

Figure 5.1: Photocurrent J normalized to the radiation power P measured in x- and y-direction in sample #1 for zero magnetic field as a function of the azimuthal angle α. The photocurrent J_y/P is multiplied by a factor of -10. The arrows on top illustrate the polarization plane orientation for several angles α. The data are obtained for gate voltage combination $U_{\mathrm{G1/G2}} = 0.5/0\,\mathrm{V}$. Dashed curves are fits based on Eq. (5.1). The inset sketches the experimental geometry and shows a schematic sketch of the gate structure with gate potentials applied to narrow stripes (gate G1) and the wider stripes (gate G2).

stripes for the angle $\alpha = 0°$. The overall polarization dependence can be well fitted by

$$J_{x,y}(\alpha) = J^{\mathrm{A}}_{x,y} \cos(2\alpha) + J^{\mathrm{B}}_{x,y} \sin(2\alpha) + J^{\mathrm{D}}_{x,y}\,, \tag{5.1}$$

where $J^{\mathrm{A}}_{x,y}$, $J^{\mathrm{B}}_{x,y}$, and $J^{\mathrm{D}}_{x,y}$ are fitting parameters. The latter term $J^{\mathrm{D}}_{x,y}$ is the polarization independent contribution, called Seebeck ratchet current (as introduced in Chap. 2.1). The Stokes parameters of the radiation are represented by $\cos(2\alpha)$ and $\sin(2\alpha)$ (for more details see Chap. 3.3). The fact that the photocurrent given by Eq. (5.1) is polarization dependent and is observed at normal incidence of the radiation onto the double grating gate structure, indicates that this current is generated by the ratchet effect.

A further evidence for this is provided by the experiments measuring the gate voltage dependencies of the photocurrents for the thinner and thicker gate

stripes. The ratchet effects are expected to be dependent on the in-plane asymmetry of the electrostatic potential. As was shown in Chap. 2.1, the ratchet effect is proportional to the averaged product (see Eq. (2.7))

$$\Xi = \overline{|E(x)|^2 \frac{\partial V}{\partial x}}$$

of the electric near-field distribution $E(x)$ as well as to the derivative of the coordinate dependent electrostatic potential $V(x)$ [15–17, 20]. Therefore, sweeping one gate bias, e.g. U_{G1}, from negative to positive voltages and holding the other one at zero should cause the sign inversion of the ratchet current. This is indeed observed for all three contributions $J^{\mathrm{D}}_{x,y}/P$, $J^{\mathrm{A}}_{x,y}/P$ and $J^{\mathrm{B}}_{x,y}/P$ as shown in Fig. 5.2. Additionally, the direction of the photocurrent can be reversed by sweeping U_{G2}, which was previously set to zero, and holding U_{G1} at zero bias. These observations clearly demonstrate that the photocurrent generated has its origin in the ratchet effect.

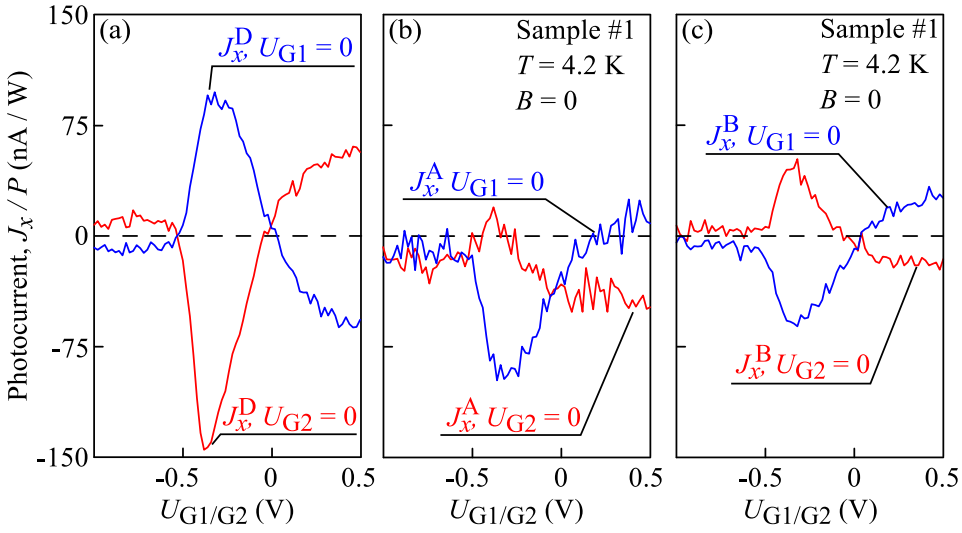

Figure 5.2: Magnitudes of the photocurrent contributions J^{D}_x, J^{A}_x and J^{B}_x normalized to the radiation power P measured in sample #1 for zero magnetic field in (a), (b) and (c), respectively. Magnitudes J^{D}_x/P, J^{A}_x/P and J^{B}_x/P are plotted against the gate voltage U_{G1} (U_{G2}) for zero potential on the other gate U_{G2} (U_{G1}).

It should be noted that while the dominating contribution to the total photocurrent comes from the polarization independent Seebeck current J^{D}_x/P, po-

larization dependent currents also yield substantial contributions, see Fig. 5.2. It is also important that the polarization dependence cannot be attributed to the magnitude variation of the Seebeck ratchet effect due to the change of the radiation reflection from the metallic DGG structure. The radiation reflection would result in a minimum signal for the radiation electric field parallel to the gate stripes ($\alpha = 90°$), whereas in the experiments exactly the opposite behavior was observed; the minimum signal is achieved for electric field $\boldsymbol{E}_\mathrm{f}$ perpendicular to the stripes in x-direction ($\alpha = 0$) as shown in Fig. 5.1.
Further proof that the polarization dependence is not caused by the Seebeck effect is shown in Fig. 5.3. It can be seen that for sample #2 at zero magnetic field, the photocurrent changes its direction as function of the azimuthal angle α for the gate voltage combination $U_{\mathrm{G1/G2}} = 0/0.25$ V. This sign change cannot be attributed to the magnitude variation of the Seebeck ratchet effect alone.

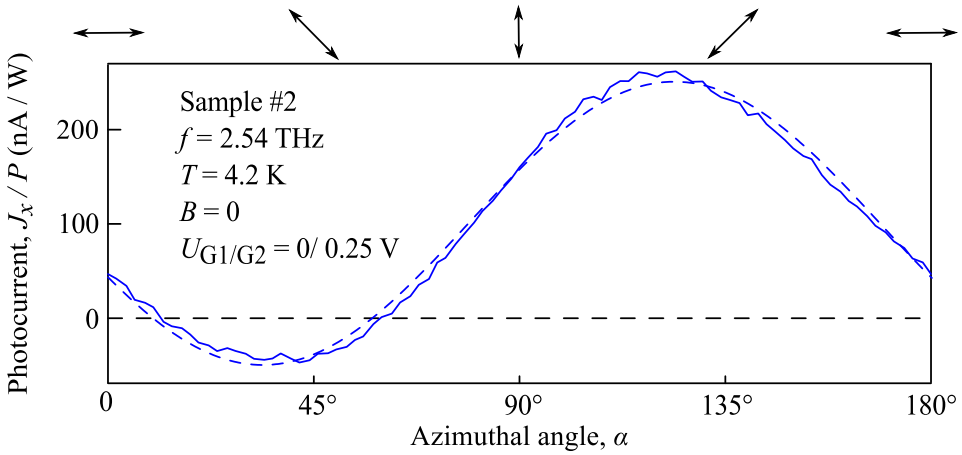

Figure 5.3: Normalized photocurrent J_x/P measured as a function of the azimuthal angle α in sample #2 at zero magnetic field. Arrows on top illustrate the polarization plane orientation for several angels α. The data are obtained for gate voltages $U_{\mathrm{G1/G2}} = 0/0.25$ V. Dashed curve is the fit based on Eq. (5.1).

An investigation of the contribution proportional to the radiation helicity is necessary to fully describe the influence of the polarization on the ratchet current generation. Figure 5.4(a) shows the photocurrent J_x/P as a function of

the radiation helicity for sample #1 at zero magnetic field for the gate voltages $U_{\mathrm{G1/G2}} = 0/-0.5\,\mathrm{V}$. This gate voltage combination suppresses the contributions proportional to the coefficients J_x^{A}/P, J_x^{B}/P, and J_x^{D}/P as shown in Fig. 5.2. The data obtained can be well fitted by

$$J_{x,y}(\varphi) = J_{x,y}^{\mathrm{A}} \frac{1+\cos(4\varphi)}{2} + J_{x,y}^{\mathrm{B}} \frac{\sin(4\varphi)}{2} - J_{x,y}^{\mathrm{C}} \sin(2\varphi) + J_{x,y}^{\mathrm{D}}, \tag{5.2}$$

where $J_{x,y}^{\mathrm{C}}$ is a fitting parameter for the contribution proportional to the degree of circular polarization $P_{\mathrm{circ}} = \sin 2\varphi$. The latter corresponds to the fourth Stokes parameter (see Chap. 3.3). In sweeping either U_{G1} or U_{G2} the helicity driven photocurrent is - for both gates - proportional to the degree of the electrostatic potential asymmetry as shown in Fig. 5.4(b). Both observations further prove that the photocurrent measured is generated by the ratchet effect due to the sign sensitivity on the circularly polarized radiation and that this photocurrent contribution can be directly influenced by the lateral asymmetry. The same behavior was observed in sample #2. An example of the helicity dependence obtained in this sample is depicted for the gate voltage combination $U_{\mathrm{G1/G2}} = 0/0$ in the inset of Fig. 5.4(a). It can be seen that the measured curve is well fitted by Eq. (5.2). The inset further reveals that the ratchet current can be detected even for zero bias at both gates. For unbiased gates, the required lateral asymmetry is induced by a non-zero built-in electrostatic potential which is formed by the influence of the metal stripes in the QW vicinity. This lateral asymmetry potential is particularly large in sample #2 compared to sample #1.

It should be noted that the overall characteristics of the data measured for different cool down processes is the same, but the sign inversions of the photocurrent can shift on the gate voltage scale by $\pm 0.1\,\mathrm{V}$ [37]. This has already been addressed in Chap. 4.1.6 for the gate voltage dependencies of the transport measurement and can also be ascribed to the charge trapping in the insulator for different cool downs. Another aspect is that the polarization independent contribution to the photocurrent vanishes at large negative gate voltages. This is probably caused by closing the transistor channel below the superlattice. In Fig. 5.2, the saturation of the photocurrent at large positive gate voltages is revealed, which is attributed to the effect of high electron densities [37].

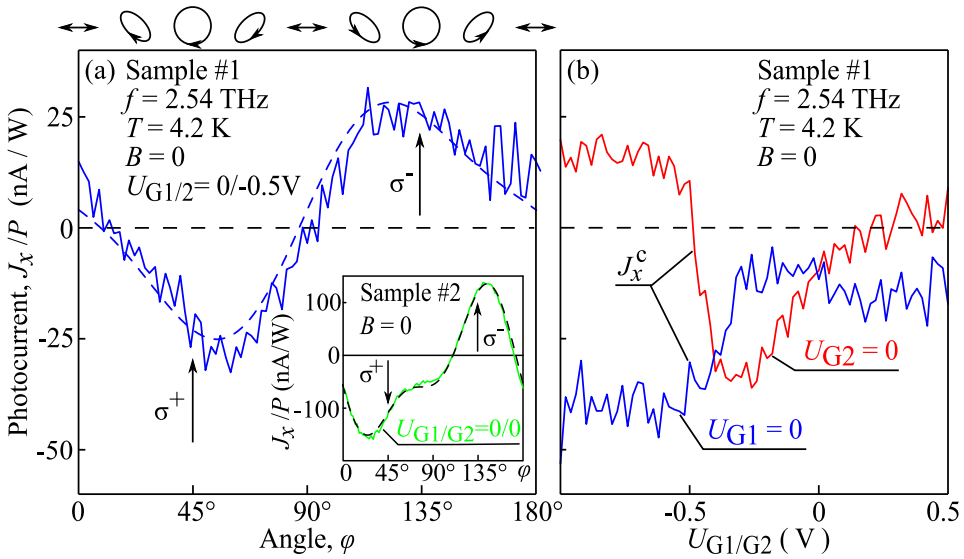

Figure 5.4: Normalized photocurrent J_x/P measured in (Cd,Mn)Te QW samples for zero magnetic field. (a) shows the photocurrent excited in sample #1 as a function of the angle φ. The symbols on top illustrate the polarization states for several values of φ. Vertical arrows indicate angles φ for right-handed ($\sigma^+, \varphi = 45°$) and left-handed ($\sigma^-, \varphi = 135°$) circularly polarized radiation. The data are obtained for the gate voltage combination $U_{\mathrm{G1/G2}} = 0/-0.5\,\mathrm{V}$. The dashed curve is the fit according to Eq. (5.2). The inset shows the photocurrent as a function of the angle φ detected in sample #2. Here, both gates are set to zero voltage. (b) shows the dependencies of the magnitude J_x^{C}/P on the gate voltage U_{G1} (U_{G2}) obtained for zero gate potentials U_{G2} (U_{G1}) for sample #1 in red (blue).

5.2 Microscopic Theory and Comparison with Experiments

A direct electric current can be generated due to the influence of an alternating electric field of an electromagnetic wave in a low-dimensional semiconductor structure with lateral top gate grating [35] (see Chap. 2.1). The DGG structure on top of the sample surface has two effects. First, it causes a one-dimensional periodic electrostatic potential $V(x)$, which acts upon the 2D carriers. The second effect is a periodic spatial modulation of the THz electric field due to the near-field diffraction [37].

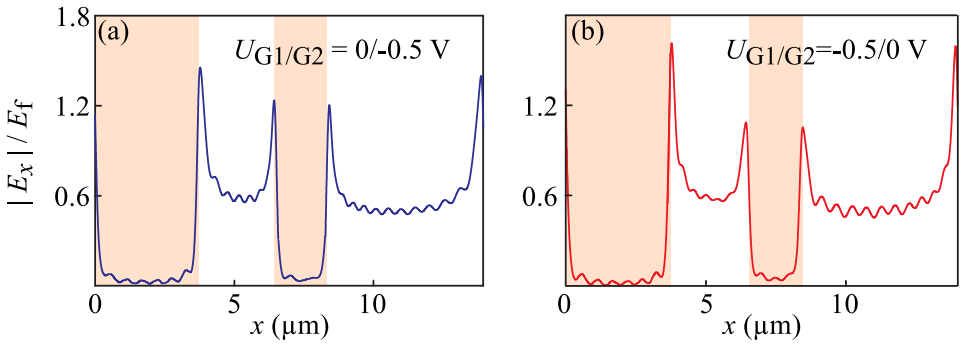

Figure 5.5: Normalized electric near-field $E_x(x)/E_\mathrm{f}$, with the incident THz electric field E_f, as a function of the x-coordinate. The DGG metal stripes are illustrated with shaded regions. The calculations were done for parameters of (Cd,Mn)Te QW sample #1 with dielectric constant $\epsilon = 10$ at the frequency $f = 2.54\,\mathrm{THz}$. The momentum relaxation time τ is obtained from the electron mobility given in Chap. 4.1.6 (adapted from Ref. [37]).

The normalized THz electric near-field $E_x(x)/E_\mathrm{f}$ is calculated for the frequency $f = 2.54\,\mathrm{THz}$ as a function of the x-coordinate, see Fig. 5.5. The electric field is computed for two combinations of the gate voltages $U_{G1/G2}$ for the (Cd,Mn)Te QW based DGG structures. As shown in Fig. 5.5, the near-field distribution hardly depends on the applied gate voltages and, therefore, the influence of the gate voltages is neglected. The calculations for the electric field distribution were done by Prof. V.V. Popov[4] and co-workers using a self-consistent electromagnetic approach, which is described in detail in Ref. [73].

The THz absorption spectrum was calculated for the parameters of sample #1 and is shown in Fig. 5.6. The calculation demonstrates that the plasmonic resonances in the QWs appear at lower frequencies than the radiation frequency ($f = 2.54\,\mathrm{THz}$) of the experiments. Hence, the absorption in the experiments follows the Drude law, see Fig. 5.6(b) showing a smaller frequency range located around the marked frequency $f = 2.54\,\mathrm{THz}$. Therefore, the plasma oscillations have hardly any influence on the near-field distribution and thus, the near-field distribution is caused almost solely by the metal dual-grating gate on top of the sample surface. Since the laser radiation frequency is much higher than the

[4]Institute of Radio Engineering and Electronics (Saratov Branch), 410019 Saratov, Russia

ones necessary for plasmonic resonances, only the electronic ratchet mechanism will be considered in the following section [37].

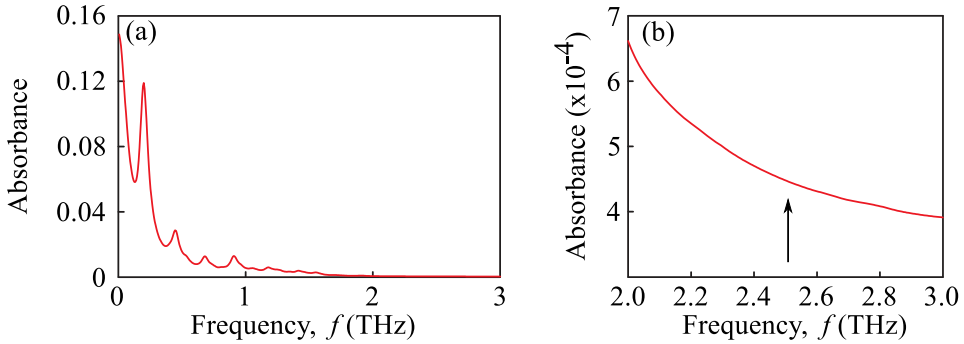

Figure 5.6: (a) illustrates the THz absorption spectrum of the structure. (b) shows the spectrum in the vicinity of the frequency $f = 2.54\,\mathrm{THz}$ (indicated by vertical arrow) used in the experiments. The curve is calculated for the parameters used in Fig. 5.5 (adapted from Ref. [37]).

As introduced in Chap. 2.1, the ratchet current is generated by the combination of the radiation near-field shining through the grating stripes and the periodic static potential $V(x)$, which both act on the carriers [14–16, 22, 28]. An important requirement for the generation of a direct electric current is the asymmetric lateral superlattice. The lateral asymmetry Ξ can be reversed by varying the potential $V(x)$ due to the controllable changing of the gate voltages U_{G1} and U_{G2}. Therefore, a sign inversion of the generated ratchet photocurrent can occur and this was observed in the experiment as shown in Fig. 5.2.
The ratchet current was described in Eq. (2.6) which shows that the current has components perpendicular (x-direction) and parallel (y-direction) to the gates stripes. The general ratchet current consists of polarization independent, linear and circular contributions, which were observed and described in various semiconductor-based structures [14, 15, 22] and also in graphene with lateral periodical top gates [16,28]. The basic principle of the photocurrent generation can be illustrated by using the example of the polarization independent Seebeck ratchet (thermo ratchet) effect. Like depicted in Fig. 5.2 and discussed in Chap. 5.1, the polarization independent contribution dominates at zero magnetic field.

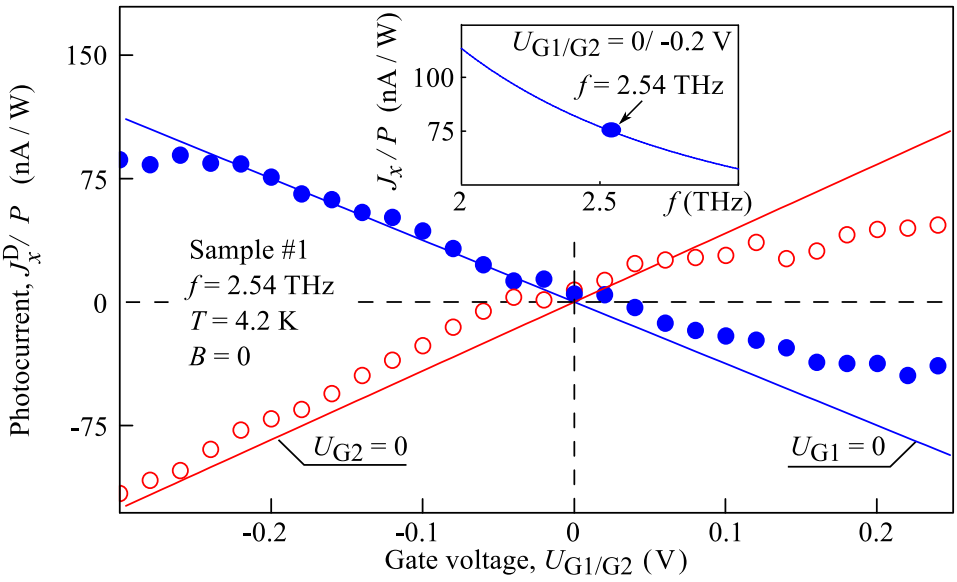

Figure 5.7: Photocurrent $J_x/P = j_0 w_2$ calculations as function of the gate voltages U_{G1} (red) and U_{G2} (blue) fitted to experimental curves shown in Fig. 5.2. The linear fit curves are obtained after Eq. (5.3). The calculations were done for $\boldsymbol{E}_f \parallel x$ in accordance with the experimental setup. The structure parameters for (Cd,Mn)Te DGG QW samples (see Chap. 4.1.2), electric near-field $E_x(x)$ (see Figs. 5.5(a) and (b)), frequency $f = 2.54\,\mathrm{THz}$, effective mass $m^* = 0.1\,m_0$ and lattice temperature $T = 4.2\,\mathrm{K}$ were used for the calculations. Fitting parameter is the relaxation time $\tau_\varepsilon = 4\,\mathrm{ns}$. The inset shows the fit of the photocurrent J_x/P as function of the frequency together with the experimental result for $f = 2.54\,\mathrm{THz}$ (depicted as a dot) (adapted from Ref. [37]).

As outlined in Chap. 2.1, the Seebeck ratchet effect has its origin in the inhomogeneous heating of the two-dimensional electron gas and subsequent relaxation of the electron temperature [37]. The near-field $E_x(x)$ is space modulated and, therefore, the influence on the electrons is also x-coordinate dependent, see Fig. 5.5. This electric near-field heats the 2DEG and hence locally changes the effective temperature to $T(x) = T_e + \delta T(x)$. It is assumed that within a short time the electron distribution becomes a quasi equilibrium Fermi-Dirac distribution with the temperature $T(x)$ [37]. By following Ref. [16], the space-modulated temperature correction is defined by the energy balance. Further,

it has to be taken into account that $\omega\tau \gg \omega_c\tau \gg 1$ for the experiments.
The inhomogeneous heating of the electrons results in an electron diffusion from the warmer to the colder regions, forming a non-equilibrium density profile. Thus, the ratchet current at zero magnetic field can be treated as drift current of the electrons in an electric field $\boldsymbol{E}$ of the space modulated electrostatic potential $V(x)$ [37]. Taking Ohm's law $\boldsymbol{j} = \sigma\boldsymbol{E}$ and replacing $\boldsymbol{E}$ by $-(1/e)\partial V/\partial x$, the Seebeck current j_0 has the form:

$$j_0 = -\frac{e\tau}{m^*}\,\overline{\delta N(x)\frac{\partial V(x)}{\partial x}}.$$

The bar stands for averaging over the superlattice period d (see Chap. 4.2) and $\delta N(x)$ is the spatially modulated electron density. Based on Refs. [16,35], the ratchet current density for zero magnetic field can be written as:

$$j_0 = \frac{\pi e^3 \tau_\varepsilon k_\mathrm{B} T}{3m^*\hbar^2\omega^2 E_\mathrm{F}}\Xi, \tag{5.3}$$

with Ξ given in Eq. (2.7) and the temperature relaxation time τ_ε.
In Fig. 5.7, the photocurrent calculated after Eq. (5.3) is plotted together with the experimental data of Fig. 5.2(a). The parameters of sample #1 as well as the near-field $E_x(x)$, which is depicted in Fig. 5.5, were used for the calculations. The temperature relaxation time τ_ε in Eq. (5.3) was the only adjustable parameter and was set to $\tau_\varepsilon = 4\,\mathrm{ns}$, whilst the value of τ_ε agrees with the one reported for degenerate electron gas in GaAs-based heterojunctions [74]. The experiment and the theory of the ratchet effect show qualitative and reasonably good quantitative agreement in Fig. 5.7.

Aside from the polarization independent Seebeck ratchet effect, the THz radiation can induce additional photocurrents which are sensitive to the linearly or to the circularly polarized radiation. These currents appear because the carriers can move in the xy-plane of the 2DEG and are influenced by the two electric field components E_x and E_y.

As already discussed in Chap. 2.1, these photocurrents are well described by means of the classical Boltzmann statistics [15, 22]. The direct current equations are given in the following form:

$$\begin{aligned} j_x &= [\chi_1 + \chi_2(|\hat{\boldsymbol{e}}_x|^2 - |\hat{\boldsymbol{e}}_y|^2)]\Xi\,, \\ j_y &= [\chi_3(\hat{\boldsymbol{e}}_x\hat{\boldsymbol{e}}_y^* + \hat{\boldsymbol{e}}_y\hat{\boldsymbol{e}}_x^*) - \gamma^* P_{\mathrm{circ}}\hat{\boldsymbol{e}}_z]\Xi\,, \end{aligned} \tag{5.4}$$

with the Stokes parameter (see Chap. 3.3)

$$\begin{aligned} s_0 &= |E(x)|^2, \\ s_1 &= |\hat{\boldsymbol{e}}_x|^2 - |\hat{\boldsymbol{e}}_y|^2 = \frac{\cos 4\varphi + 1}{2} = \cos 2\alpha, \\ s_2 &= \hat{\boldsymbol{e}}_x\hat{\boldsymbol{e}}_y^* + \hat{\boldsymbol{e}}_y\hat{\boldsymbol{e}}_x^* = \frac{\sin 4\varphi}{2} = \sin 2\alpha, \\ s_3 &= -P_{\mathrm{circ}}\hat{\boldsymbol{e}}_{\boldsymbol{z}} = -\sin 2\varphi. \end{aligned}$$

The remaining coefficients are

$$\chi_2 = \chi_3 = -\omega\tau\gamma^*, \qquad \chi_1 = (4\tau_\epsilon - \tau)\omega\gamma^*\,,$$

with

$$\gamma^* = \frac{e^2}{2m^*}\frac{\mu_e N_0}{k_{\mathrm{B}}T}\frac{\tau}{\omega(1+\omega^2\tau^2)}\,.$$

The previous theoretical work undertaken, which led to Eq. (5.4), investigated unconnected parallel metal stripes. These systems have a C_s point group symmetry which consists of the identity element and the reflection in the xz-plane perpendicular to the gate stripes [14–17, 19, 22]. Hence, the circular photocurrent contribution $J_y^{\mathrm{C}} \propto \gamma^*\Xi$ and the linear photocurrent $J_y^{\mathrm{B}} \propto \chi_3\Xi$ can only occur parallel to the gate stripes, whereas the polarization independent offset $J_x^{\mathrm{D}} \propto \chi_1\Xi$ and the linear photocurrent $J_x^{\mathrm{A}} \propto \chi_2\Xi$ are only allowed in the x-direction (perpendicular to the gate stripes).
In this work, the experimental results demonstrate that all four contributions can be detected in both x- and y-directions which can be explained in the following way. The electromagnetic wave undergoes a change in its polarization when passing through the metal grating, due to an effective birefringence, meaning that the linear s_2 and the circular polarization s_3 are partially transformed into each other. Consequently, the electric field behind the grating - s_2^*

and s_3^* - is a linear combination for both of them: $s_2^* = s_2 + s_3$ and $s_3^* = s_2 + s_3$ which is explained in more details in Ref. [75]. An additional effect is that the DGG samples have interconnected gate stripes for the thinner and thicker gate fingers with finite lengths and, therefore, the reflection plane is excluded, leading to a reduction of the symmetry from the C_s to the C_1 point group. The C_1 symmetry does not restrict the photocurrent and thus the observed photocurrent $J_{x,y}/P$ includes all individual contributions $J^{\mathrm{D}}_{x,y}/P$, $J^{\mathrm{A}}_{x,y}/P$, $J^{\mathrm{B}}_{x,y}/P$ and $J^{\mathrm{C}}_{x,y}/P$ [70, 76, 77].
Therefore, the Eq. (5.4) can be written as

$$j_{x,y} = [\chi_1 + \chi_2(|e_x|^2 - |e_y|^2) + \chi_3(e_x e_y^* + e_y e_x^*) - \gamma^* P_{\mathrm{circ}} \hat{e}_z]\Xi \,,$$

which is similar to Eq. (5.2). This equation can explain and fit all of the experimental results presented in Figs. 5.1, 5.3 and 5.4 and provides a good accordance between the theory and the experiments in this thesis.

5.3 Brief Summary

The experimental results presented demonstrate that using THz radiation to excite a (Cd,Mn)Te quantum well with an asymmetric top gate structure generates a polarization independent Seebeck ratchet current as well as a polarization dependent current. The latter one is sensitive to the helicity and the linear polarization of the incident radiation.
The overall behavior of the photosignal at zero magnetic field provides a consistent picture of the ratchet effect at liquid helium temperature. This is demonstrated by controllably changing the current amplitude and direction by variation of the voltages applied to the individual gates. Further, it is shown that the current also changes its amplitude and sign for different polarization states. These characteristics are observed in different samples and are in agreement with the theory of the ratchet effect, as developed in Refs. [14, 15, 22, 28]. Such behavior was also observed in different semiconductor QW structures and graphene with a lateral superlattice, see Refs. [22, 28].

6 Magnetic Quantum Ratchet Effect in CdTe and (Cd,Mn)Te QWs

This chapter focuses on the polarization independent magnetic quantum ratchet effect in CdTe/CdMgTe QWs and (Cd,Mn)Te/CdMgTe diluted magnetic heterostructures superimposed with an asymmetric lateral dual grating gate superlattice. The influence of the different polarization states on the MQRE will be considered in detail in Chap. 7.
Here, it will be shown that the ratchet current exhibits sign-alternating $1/B$-periodic oscillations with amplitudes much larger than the ratchet signal at zero magnetic field. It will be demonstrated that the lateral asymmetry can change the amplitude and the sign of these oscillations. The theory explaining the MQRE, which was initiated by the experiments and developed parallel to the measurements [35], will also be introduced. These theoretical analyses can satisfactorily describe the experimental results. All results presented in this chapter are published in Ref. [37].

6.1 Experimental Results and Discussion

The normalized photocurrents J_x/P and J_y/P were measured in directions normal and parallel to the DGG stripes. These currents were excited by linearly polarized radiation, aligned perpendicularly to the gate stripes, while a magnetic field was applied normal to the quantum well plane. The overall behavior of both photocurrents is very similar but the magnitude of the photocurrent in x-direction is two up to 10 times higher than that in y-direction. Therefore, only the data for J_x/P will be presented here.
The normalized photocurrent J_x/P as a function of the magnetic field is shown in Fig. 6.1. It can be seen that the photosignal drastically increases in amplitude when the magnetic field B is increased. The current also exhibits sign-alternating $1/B$-periodic oscillations with the same periodicity as the longitudinal magneto-resistance oscillations at high magnetic fields. The figure shows that reversing the lateral asymmetry from the gate voltage combination $U_{\mathrm{G1/G2}} = 0/-0.5\,\mathrm{V}$ (blue line) to $U_{\mathrm{G1/G2}} = -0.5/0\,\mathrm{V}$ (red line) results in an

opposite direction of the magneto-photocurrent. This is the initial evidence that the current is generated by the ratchet effect as it follows the lateral asymmetry parameter Ξ.

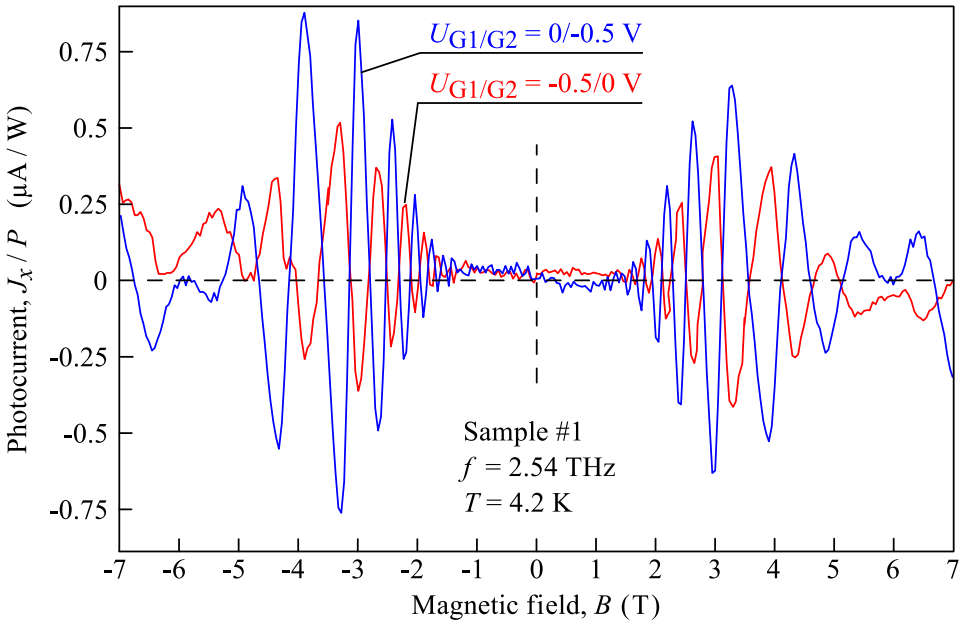

Figure 6.1: Normalized photocurrent J_x/P as a function of the magnetic field B measured in (Cd,Mn)Te QW sample #1 at $T = 4.2\,\mathrm{K}$ and radiation frequency $f = 2.54\,\mathrm{THz}$. Two different gate voltage combinations were applied: the blue (red) line represents the data for the gate voltage combination $U_{G1/G2} = 0/-0.5\,\mathrm{V}$ ($U_{G1/G2} = -0.5/0\,\mathrm{V}$). Zero magnetic field and zero photocurrent are indicated as dashed lines (adapted from Ref. [37]).

As well as predicting the sign change of the current, the asymmetry parameter Ξ also predicts the dependence on the square of the radiation electric field $|E(x)|^2$ (see Eq. (2.7)). This means that the magneto-photocurrent is a linear function of the radiation power P, which is depicted for sample #1 in Fig. 6.2. The photocurrent is shown for different radiation power levels from $P_{\mathrm{min}} = 0.8\,\mathrm{mW}$ to $P_{\mathrm{max}} = 4.3\,\mathrm{mW}$ in a small magnetic field range for the gate voltage combination $U_{G1/G2} = 0/-0.5\,\mathrm{V}$ in Fig. 6.2(a). The increase in the radiation power induces an enhancement of the photocurrent magnitude. This power dependence can be fitted linearly as illustrated in Fig. 6.2(b) and hence proves the prediction of the lateral asymmetry parameter Ξ. A further

observation in Fig. 6.2(a) is that the positions of the oscillation extrema do not depend on the radiation power.
These results, especially the magneto-oscillations with much higher amplitudes in the photocurrent as compared to the ratchet effect at zero magnetic field, were observed in all samples studied.

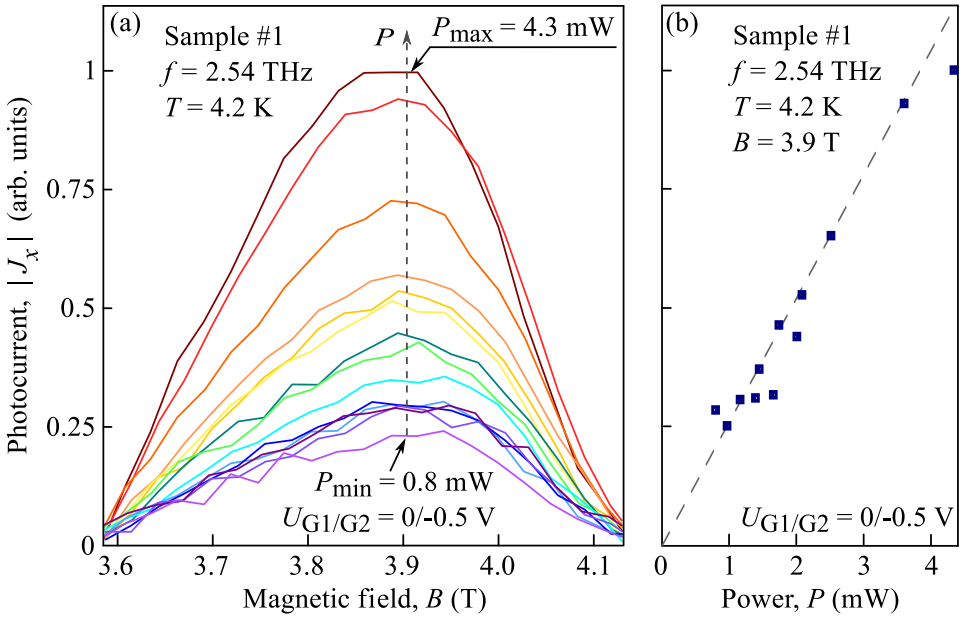

Figure 6.2: (a) shows photocurrents $|J_x|$ measured as a function of the magnetic field B at different power levels ranging from $P_{\mathrm{min}} = 0.8\,\mathrm{mW}$ to $P_{\mathrm{max}} = 4.3\,\mathrm{mW}$ for $U_{\mathrm{G1/G2}} = 0/-0.5\,\mathrm{V}$ in (Cd,Mn)Te QW sample #1. (b) illustrates the radiation power dependence of the photocurrent amplitude $|J_x|$ at $B = 3.9\,\mathrm{T}$. The dashed line is a linear fit (adapted from Ref. [37]).

In the following section, the magneto-oscillations of the ratchet current are investigated in a different top gate and a QW material to demonstrate that this effect is observed in many different samples. The influence of the top gate material is measured in the (Cd,Mn)Te QW sample #4 with the superlattice made of ferromagnetic Dy/Au gate stripes. The huge increase in the amplitude as well as the oscillations are shown in Fig. 6.3(a) for $U_{\mathrm{G1/G2}} = 0/0$. The $1/B$-oscillation period observed correlates with the transport data and is very close to the photocurrent observed in (Cd,Mn)Te QW samples with a gold superlattice, e.g. sample #1 in Fig. 6.1.

Figure 6.3(b) shows the magneto-photocurrent measured in non-magnetic CdTe QW sample #5 with a gold grating for two different gate voltage combinations, $U_{\mathrm{G1/G2}} = -2.5\,\mathrm{V}/0$ and $U_{\mathrm{G1/G2}} = 0/-2.5\,\mathrm{V}$. In sample #5, the oscillations are clearly visible but are superimposed by a substantial non-oscillating photocurrent. Consequently, the current exhibits no sign alternating behavior as detected in samples #1 and #4. This additional non-oscillation contribution to the photocurrent was also obtained for (Cd,Mn)Te QW samples #2 and #3. The reason for this photocurrent can be attributed to the imperfections found in the large-size superlattice, which can be observed through an optical microscope (see for example Fig. 4.2(c) in the top right corner). The additional current is caused by the inhomogeneities due to the imperfections and, therefore, leads to ratchet unrelated magneto-gyrotropic photogalvanic currents in the QW. For more details see Chap. 4.1.6 and, for example, Ref. [77].

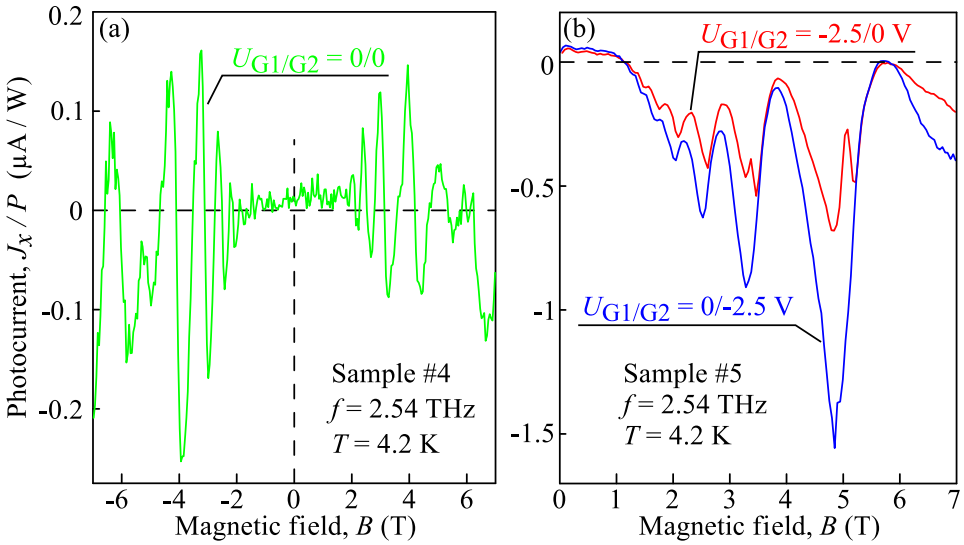

Figure 6.3: (a) shows the normalized photocurrent J_x/P measured as a function of the magnetic field B in (Cd,Mn)Te QW sample #4 with the Dy/Au grating for zero gate voltages. In (b), the J_x/P for CdTe-based QW sample #5 is depicted for two gate voltage sequences: $U_{\mathrm{G1/G2}} = -2.5\,\mathrm{V}/0$ and $U_{\mathrm{G1/G2}} = 0/-2.5\,\mathrm{V}$ as a function of B (adapted from Ref. [37]).

All aforementioned experimental results demonstrate that the ratchet current is generated by illuminating the top gate structure and is sensitive to the applied gate voltages. A sample surface scan was performed to provide additional experimental evidence for this, whereby the linearly polarized beam spot ($\boldsymbol{E}_\mathrm{f} \parallel x$) was moved along the x-direction over the sample surface.

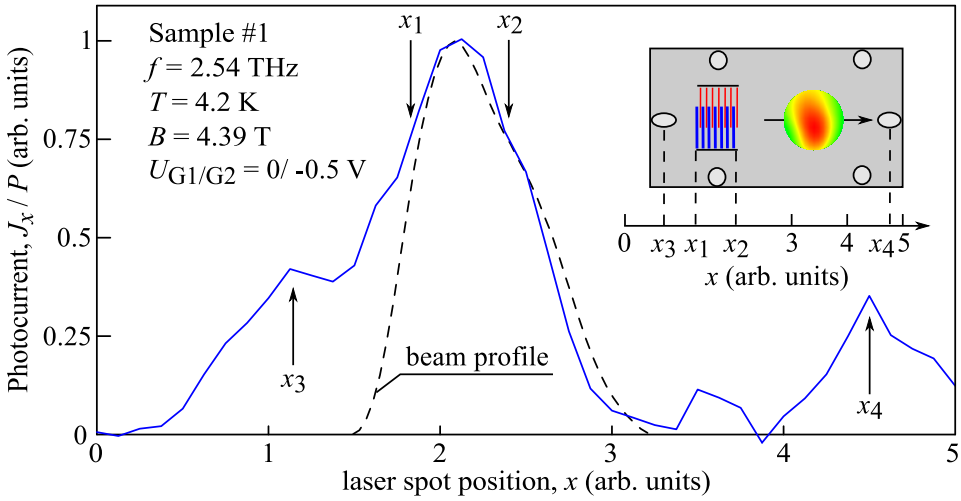

Figure 6.4: Normalized photocurrent J_x/P as a dependence of the laser spot position in (Cd,Mn)Te QW sample #1 at a maximum of the photocurrent oscillation at $B = 4.39\,\mathrm{T}$ and $U_{\mathrm{G1/G2}} = 0/-0.5\,\mathrm{V}$. The inset is a schematic sketch of the setup with the laser spot scanned along the x-direction. The borders of the superlattice are marked with x_1 and x_2. The points x_3 and x_4 denote the contact positions. The laser beam's spatial intensity distribution is normalized to the photocurrent maximum and illustrated by the dashed line (adapted from Ref. [37]).

The corresponding sketch of the experimental geometry is depicted in the inset of Fig. 6.4. The normalized photocurrent J_x/P was obtained for the gate voltage combination $U_{\mathrm{G1/G2}} = 0/-0.5\,\mathrm{V}$ at a fixed magnetic field value $B = 4.39\,\mathrm{T}$, corresponding to a maximum in the oscillations as shown in Fig. 6.1. The photocurrent J_x/P as a function of the laser spot position reaches its maximum when the laser spot is centered on the superlattice and decreases when the spot is moved away from the double grating gate, see Fig. 6.4. The smaller peaks at x_3 and x_4 occur when the laser spot touches the edges of the sample or the contacts. It should be mentioned that the contacts are rather large and,

therefore, the corresponding peaks in the surface scan are not exactly located at the sample edges. At these points, the radiation electric field causes carriers to move back and forth but they are exposed to an asymmetric scattering, induced by the contacts, resulting in a current. Such photocurrents are well known in semiconductor QWs [78] as well as in graphene [79, 80].
Comparing the Gaussian intensity distribution (dashed line in Fig. 6.4) with the change of the photocurrent amplitude by scanning across the surface, it can be seen that the current almost follows the beam profile. This measurement unambiguously demonstrates that the magneto-photocurrent generated stems from the THz irradiation of the superlattice.

One of the prerequisites for the ratchet effect is the lateral asymmetry Ξ. Therefore, the role of the double grating gate was systematically studied by measuring the magneto-photocurrents for different bias voltage combinations. For several samples, the results are depicted in Figs. 5.2, 6.1, 6.3 and 6.5.
For a better insight into the influence of Ξ, the photocurrent was measured for a set of various magnitudes and polarities of U_{G1} and U_{G2} (see Tab. 3) in the magnetic field range $B = 2.7\,\mathrm{T} - 4.1\,\mathrm{T}$ as shown in the inset in Fig. 6.5. This demonstrates that the variation of the gate potentials strongly influences the magnitude and the sign of the photocurrent oscillations. Further, it can be seen that the peak positions do not shift with variation of the gate combinations, which is illustrated with the vertical dashed lines in the inset of Fig. 6.5.

Number	1	2	3	4	5	6
U_{G1} (V)	0	-0.5	0.5	-0.5	0.5	-0.5
U_{G2} (V)	-0.5	0.5	0	-0.5	-0.5	0

Table 3: Gate voltage combinations for related numbers in inset in Fig. 6.5.

Taking into account that the extrema positions of the oscillations do not shift by varying the magnetic field, the influence of the lateral asymmetry Ξ was investigated at a certain magnetic field. The experiments were carried out at $B = \pm 3.9\,\mathrm{T}$, and the photocurrent was measured by the stepwise changing of

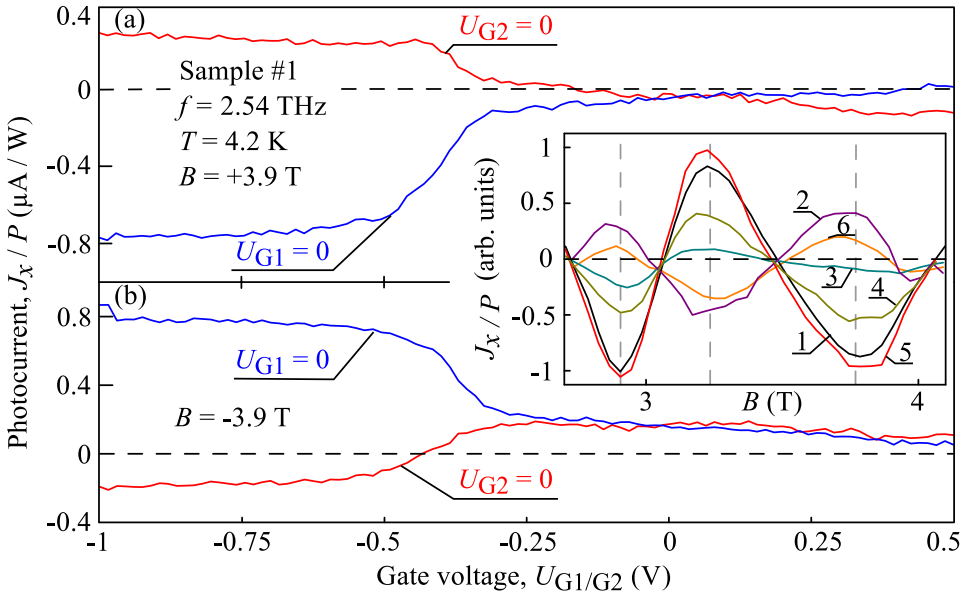

Figure 6.5: Magnitude of the normalized photocurrent J_x/P as a dependence of the gate voltage U_{G1} (U_{G2}) for zero potential on the second gate U_{G2} (U_{G1}). (a) and (b) show the data obtained for (Cd,Mn)Te QW sample #1 at $B = +3.9\,\mathrm{T}$ and $-3.9\,\mathrm{T}$, respectively. Different gate voltage combinations in a small magnetic field dependence of the photocurrent are shown in the inset. The maxima/minima positions of the photocurrent oscillations are not shifted for different gate voltage combinations, as illustrated by the vertical dashed lines. The gate combinations relating to the numbers in the inset are summarized in Tab. 3 (adapted from Ref. [37]).

the applied potential to one of the gates, while the other one was held at zero bias. The experimental results for (Cd,Mn)Te QW sample #1 are depicted in Fig. 6.5(a) for $B = +3.9\,\mathrm{T}$ and the results for $B = -3.9\,\mathrm{T}$ are shown in Fig. 6.5(b). It can be seen that the photocurrent changes its polarity when the sign of the asymmetry parameter Ξ is inverted. The influence of this inversion can mainly be seen by comparing the data obtained by variation of the potentials applied either to the thinner (red) or to the thicker (blue) gate stripes. A stronger pronounced change of the signal is observed at $U_{G1}(U_{G2}) \approx -0.35\,\mathrm{V}$. This change corresponds to the increase of the longitudinal resistance, obtained in the magneto-transport measurements as shown in the inset in Fig. 4.4. Figure 6.5 also reveals that a ratchet current is observable for zero

voltage at both gates. This is caused by the built-in potential of the metallic top gate stripes.

The influence of the lateral asymmetry on the photocurrent was further studied in (Cd,Mn)Te samples #2 and #3, as well as in CdTe QW sample #5. In these three samples, the measurements reveal that the photocurrent magnitude can be controlled by the lateral asymmetry, despite the non-oscillating photocurrent part. The results for CdTe QW DGG structure #5 at $B = \mp 4.9\,\mathrm{T}$ are presented in Figs. 6.6(a) and (b) by way of example.

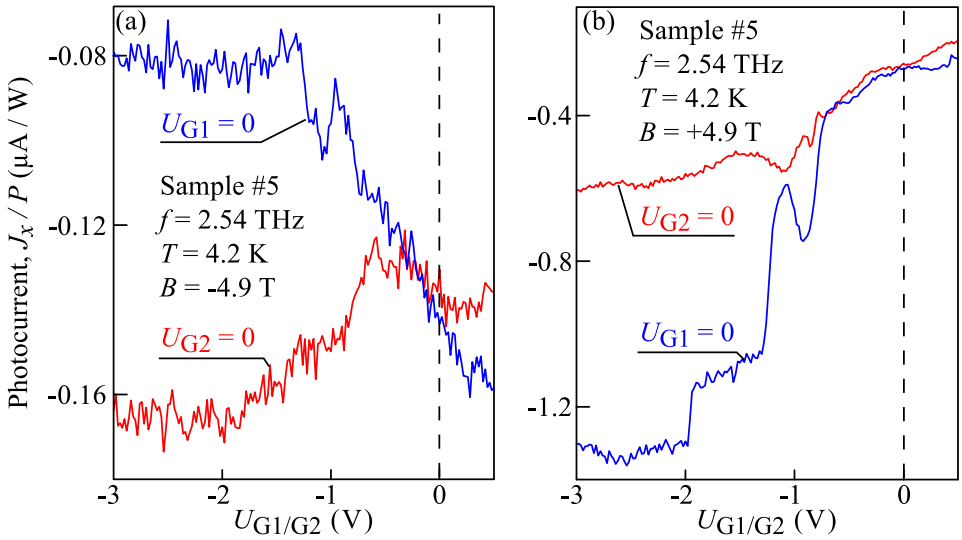

Figure 6.6: Normalized photocurrent J_x/P as a function of the gate voltage U_{G1} (U_{G2}) measured for zero potential on the second gate U_{G2} (U_{G1}). The data are obtained for photocurrent maxima/minima at $B = -4.9\,\mathrm{T}$ and $+4.9\,\mathrm{T}$ in (a) and (b), respectively (adapted from Ref. [37]).

All data presented were performed at liquid helium temperature, but to obtain an insight in the temperature dependence of the photocurrents, several experiments were carried out in the range from 2 K up to 9 K. The measurements reveal, that the amplitude of the oscillations grows with the increasing magnetic field in CdTe and (Cd,Mn)Te QW samples at relatively high temperatures. This is shown by way of example for (Cd,Mn)Te QW sample #1 at 9 K in Fig. 6.7(a). After reducing the temperature to $T = 4.2\,\mathrm{K}$, the increase in the magneto-photocurrent amplitude at low magnetic fields is followed by a

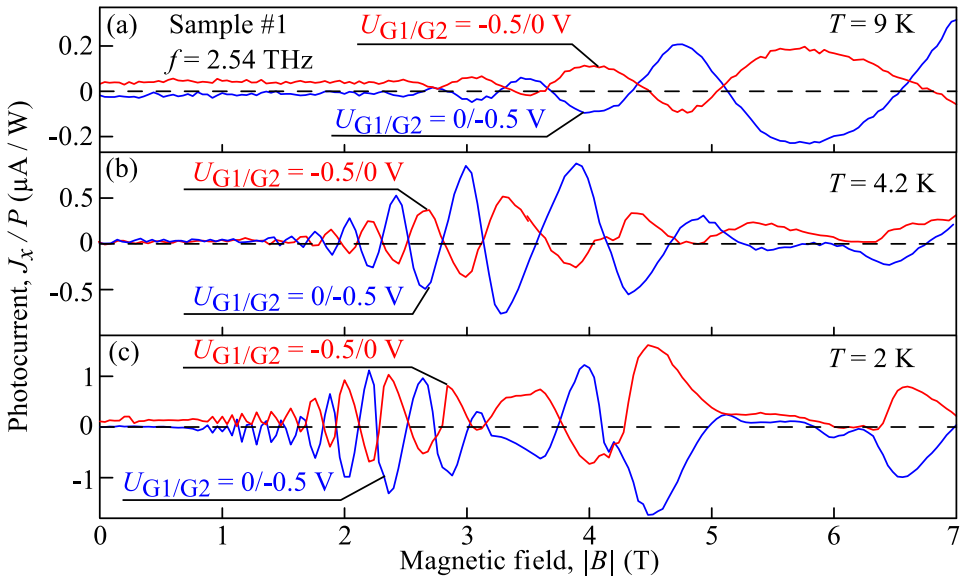

Figure 6.7: Normalized photocurrent J_x/P as a function of the magnetic field B in (Cd,Mn)Te QW DGG sample #1 for two gate voltage combinations at 9 K, 4.2 K and 2 K in (a)-(c), respectively (adapted from Ref. [37]).

decrease of the amplitude at higher magnetic fields in diluted magnetic semiconductor (Cd,Mn)Te QW samples, e.g. for sample #1 see Fig. 6.7(b). By cooling the sample to $T = 2\,\mathrm{K}$, the amplitude of J_x/P is further increased compared to $T = 4.2\,\mathrm{K}$ and starts earlier to oscillate. The decrease of the amplitude at higher magnetic fields ($B \approx 3\,\mathrm{T}$) occurs also earlier compared to $T = 4.2\,\mathrm{K}$ ($B \approx 4.2\,\mathrm{T}$) as shown in Fig. 6.7(c).

Similar behavior was detected in the longitudinal resistance, see Fig. 4.3(a), which is in a good agreement with the occurrence of the giant Zeeman splitting in the DMS materials as discussed in Chap. 2.3 [45]. The giant Zeeman splitting can be described by the temperature-dependent modified Brillouin function and is caused by the exchange interaction between Mn^{2+} ions and electrons. At first, the spin splitting grows with the increasing magnetic field but then saturates. The temperature increase results in a decrease of the giant Zeeman splitting and, therefore, shifts the saturation to higher magnetic fields. This behavior was observed in the photocurrent and in the magneto-transport measurements in all (Cd,Mn)Te samples.

6.2 Microscopic Theory and Comparison with Experiments

In order to describe the origin of the photocurrents shown in this chapter, the results of the microscopic magnetic quantum ratchet model will be presented here. This model was developed simultaneously to the experiments by Prof. L. E. Golub[5] and co-workers. It is based on the assumption of a quasi equilibrium Fermi-Dirac distribution and will be introduced according to Ref. [35]. A comparison between the theory and the experimental data will also be given.

The microscopic theory developed in Chap. 5.2 is expanded by the influence of the magnetic field and the results for the magnetic quantum ratchet effect are the equations for the ratchet currents j_x and $j_y \propto j_x B_z$, given by [35]

$$\begin{aligned} j_x &= j_0 \frac{48 E_\mathrm{f}^2}{\hbar\omega_c k_\mathrm{B} T} \frac{(\omega_c\tau)^2}{[1+(\omega_c\tau)^2]^2} \frac{\sinh z - z\cosh z}{\sinh^2 z}\delta\,, \\ j_y &= -\frac{B_z}{|B_z|} \frac{1+3(\omega_c\tau)^2}{2(\omega_c\tau)^2} j_x. \end{aligned} \tag{6.1}$$

Here, j_x and j_y are respectively the currents in the direction perpendicular and parallel to the stripes of the superlattice, while

$$j_0 = \frac{\pi e^3 \tau_\varepsilon k_\mathrm{B} T}{3 m^* \hbar^2 \omega^2 E_\mathrm{F}} \overline{|E(x)|^2 \frac{\partial V}{\partial x}}$$

is the current at zero magnetic field and was introduced in Chap. 5.2. The factor $(\sinh z - z\cosh z)/\sinh^2 z$ with $z = 2\pi^2 k_\mathrm{B} T/(\hbar\omega_c)$ shows the oscillation suppression with increasing temperature.

The Eq. (6.1) is obtained in the first order in δ, describing the magneto-oscillations for $|\delta| \ll 1$:

$$\delta = \cos\left(\frac{2\pi E_\mathrm{F}}{\hbar\omega_c}\right) \cos\left(\frac{\pi \Delta E_\mathrm{Z}}{\hbar\omega_c}\right) \exp\left(-\frac{\pi}{\omega_c\tau}\right). \tag{6.2}$$

Additionally and due to the fact that most experiments are carried out on DMS samples, the giant Zeeman effect must also be taken into account. Therefore, the theory developed in Ref. [35] considers the spin subband splitting ΔE_Z given by Eq. (2.13) in Chap. 2.3:

$$\Delta E_\mathrm{Z} = g\mu_\mathrm{B} B + \overline{x} S_0 N_0 \alpha_e \mathcal{B}_{5/2}\left(\frac{5\mu_\mathrm{B} g^*_\mathrm{Mn} B}{2k_\mathrm{B}(T_\mathrm{Mn}+T_0)}\right).$$

The ratchet current components j_x and $j_y \propto j_x B_z$ have opposite parity when the magnetic field reverses its sign, as predicted in Eq. (6.1). This is caused by the deflection of the photocurrent induced by the Lorentz force [78].
The oscillating behavior of the ratchet current is induced by the interaction of the magnetic field and the Landau levels. As described in Chap. 2.2, the Landau levels move through the Fermi level as a function of the magnetic field, resulting in $1/B$-periodic oscillations of the longitudinal magneto-resistance. The period is the same for the resistance oscillations and for the photocurrent oscillations. This will be discussed in more detail in Chap. 7.2.
The oscillation magnitude is greatly enhanced compared to the ratchet current at zero magnetic field. The reason for this is that, in a quantized magnetic field, the ratchet current does not arise due to a variation of the electron density but due to the heating-induced corrections to the conductivity. Since the conductivity is very sensitive to variations of the electron temperature in this regime, small variations in the temperature near the Dingle temperature [81] result in exponentially strong changes of the conductivity. Hence, the sensitivity of the conductivity to the electron gas heating results in the enhancement of the ratchet current [37]. The factor $(E_\mathrm{F}/k_\mathrm{B}T)(E_\mathrm{F}/\hbar\omega_c) \gg 1$ dominates the ratio $j(B)/j_0$ and, therefore, this ratio can reach about two orders of magnitude [35]. It should be mentioned that this increase of the amplitude arises in magnetic fields where the longitudinal resistance exhibits weak SdH oscillations. The conductivity can be decreased or increased by the heating effect, depending on the sign of the correction $\partial\sigma/\partial T$, which changes its sign as a function of B. Therefore, the heating-induced ratchet current is an oscillating function of the magnetic field with a mean value equal to zero. This predicted behavior of the photocurrent was measured and is shown in Figs. 6.1 and 6.3. Both figures show the increase of the amplitude compared to zero magnetic field, as well as the oscillating of the ratchet current.

In addition to the periodicity in $1/B$, the increase of the amplitude and the oscillations of the ratchet current, the theory predicts that the current is linearly proportional to the radiation intensity $|\boldsymbol{E}_\mathrm{f}|^2$. This behavior was experimentally studied and confirmed by illuminating the sample with different radiation powers. The results are presented in Fig. 6.2(a) and the linear dependence is shown in (b).

Besides the intensity, the lateral asymmetry parameter Ξ includes the influence of the potential $\partial V/\partial x$. This means that when the sign of the potential is changed, e.g. by changing the gate voltages applied, the ratchet current should reverse its sign as well. This characteristic was observed in many measurements as shown in Figs. 6.1, 6.5 and 6.6.

In the DMS structures, a more complicated behavior of the oscillating ratchet current was observed at low temperatures, which is also described in Eqs.(6.1) and (6.2). The giant Zeeman splitting is absent in QWs without magnetic ions and, therefore, the second term in ΔE_Z (Eq. (2.13)) disappears. The cosine argument $\zeta \equiv \pi \Delta E_Z/(\hbar\omega_c)$ in Eq. (6.2) is independent of the magnetic field and

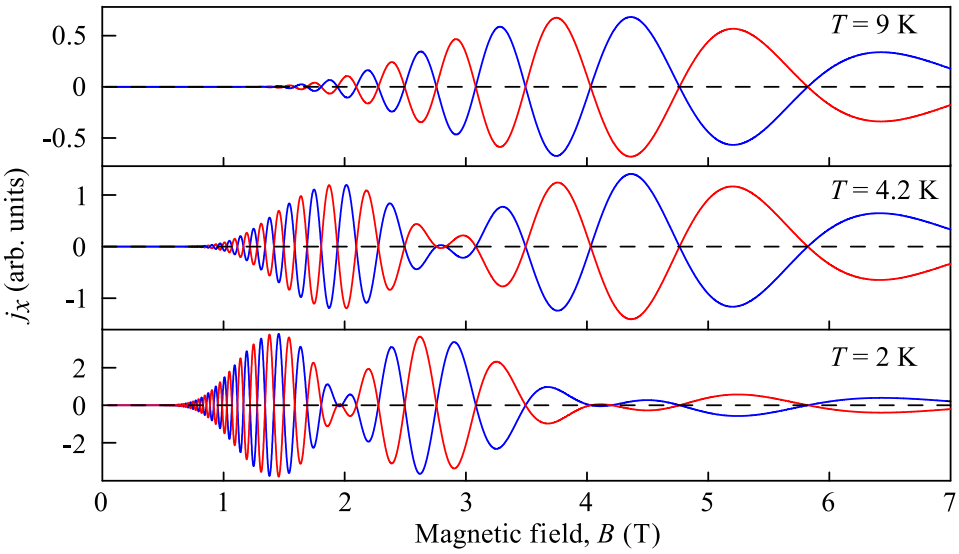

Figure 6.8: Calculated photocurrent j_x for three different temperatures for (Cd,Mn)Te QW sample #1. Parameters of the structure are in accordance with the experiment as presented in Fig. 6.1: $\mu = 0.95 \times 10^4\,\mathrm{cm}^2/(\mathrm{Vs})$, $E_F = 1.6\,\mathrm{eV}$ and $\bar{x} = 0.015$. The n-(Cd,Mn)Te literature values were used for the remaining parameters: $N_0\alpha_e = 220\,\mathrm{meV}$, $g = -1.64$ (see Ref. [45]) and $m^* = 0.1\,m_0$ (see Ref. [82]). For the calculations $T_{Mn} = T$, the literature data $T_0 = 0.8\,\mathrm{K}$ and $S_0 = 2.2$ for $\bar{x} = 0.015$ were assumed (see Ref. [83]). Two asymmetries with equal magnitudes but opposite signs of the lateral asymmetry parameter Ξ are illustrated by the red and blue curve. Compared to the ratchet current at zero magnetic field, the oscillation amplitude is much higher (adapted from Ref. [37]).

reduces to $(\pi g m^*)/(2m_0)$. For $\zeta \approx -0.26$ in CdTe-based materials, the value of $\cos(\zeta)$ differs only by 3% from unity and can be neglected. The factor $\cos(\zeta)$ for DMS structures in Eq. (6.2) results in a more complicated oscillating behavior of the ratchet current at low temperatures (for the experiments, see Fig. 6.7). Figure 6.8 shows the calculated ratchet current j_x as a function of the magnetic field for three different temperatures $T = 9, 4.2$ and $2\,\mathrm{K}$. The calculations were carried out for two gate voltage combinations with equal magnitude but opposite sign of the lateral asymmetry parameter Ξ. The influence of the temperature arises due to the temperature-dependent Brillouin function for DMS materials in the Zeeman term ΔE_Z (see Eq. (2.13)). As it is typical in DMS materials, the Zeeman splitting can be of the same order as the Landau level separation at low temperatures, which means that the manganese doping plays an important role. This influence is illustrated in Fig. 6.8 for three different lattice temperatures, namely $T = 9, 4.2$ and $2\,\mathrm{K}$ and, therefore, also for three different contributions of the Zeeman effect. Similar to the experiments, the calculations show oscillations of $j_x(B)$ with a strong reduction of the amplitude at certain magnetic field values, e.g. at $B \approx 3\,\mathrm{T}$ for $T = 4.2\,\mathrm{K}$ and at $B \approx 2\,\mathrm{T}$ for $T = 2\,\mathrm{K}$. This behavior is more pronounced at lower temperatures and results from the interaction of the Landau splitting with the Zeeman effect. The theory depicted in Eqs. (6.1) and (6.2), adequately describes the qualitative characteristics of the generated photocurrent. The small deviations between the experiments and the theory are caused by the different temperatures of the Mn atoms and the electron gas in the measurements and the values chosen for the calculations.

Note, that the manganese spin system temperature significantly influences the reduction of the oscillation amplitude in $j_x(B)$, which can be higher than the lattice temperature due to the electron gas heating [84]. This heating reduces the contribution of the second term on the right side in ΔE_Z (Eq. (2.13)), because of the Brillouin function's strong temperature T_Mn dependence, resulting in a shift of the amplitude reduction onset to higher magnetic fields.

6.3 Brief Summary

The magnetic quantum ratchet effect, i.e. the ratchet effect in quantizing magnetic fields, was experimentally demonstrated and the results obtained can be well described by the theory developed simultaneously to the experiments, see Eq. (6.1). The ratchet currents were generated by utilizing an asymmetric interdigitated dual grating gate on top of the CdTe and (Cd,Mn)Te quantum well structures. These electric currents are induced by the terahertz electric field and exhibit sign changing magneto-oscillations [37]. The amplitude of these oscillations is much higher than the photocurrent obtained at zero magnetic field, whilst the sign and the amplitude of the current can be changed controllably by variations to the voltage combinations applied to the individual gates [37]. The ratchet current is observed in different QW materials, as well as in top gate structures with different parameters, such as the stripe spacing or material.

The semi-classical theory of the magnetic ratchet effect, which was developed simultaneously, describes the generation of the photocurrent in good accordance to the experimental results. The ratchet current is caused by the periodic modulation of the electron temperature, which is introduced by the electric near-field. The Seebeck ratchet theory - in combination with a quantizing magnetic field - reveals that the current generated follows the oscillations of the longitudinal resistance [37]. The experiments performed on DMS structures show a strong influence of the exchange enhanced Zeeman splitting at low temperatures. This is caused by the exchange interaction of the Mn^{2+} ions with the electrons.

7 Polarization Sensitive Magnetic Quantum Ratchet Effect

The influence of the different polarization states on the magnetic quantum ratchet effect will be considered in detail here. The experiments and analysis were carried out in CdTe- and (Cd,Mn)Te-based QW structures superimposed with an asymmetric lateral dual grating gate superlattice.
It will be demonstrated that the ratchet effect varies its amplitude and sign by changing the linearly polarized radiation or by switching between right-handed and left-handed circularly polarized radiation. The influence of the lateral asymmetry parameter on the polarization dependent ratchet current will also be presented. The data obtained initiated the development of a theory simultaneously to the measurements; these theoretical analyses provide a good description of the experimental results.

7.1 Experimental Results and Discussion

The polarization dependencies at zero magnetic field were investigated and shown in Chap. 5 while the polarization independent Seebeck ratchet effect was in the focus of Chap. 6. In the following chapter, the experimental results of the previous chapters are combined to study the influence of the different polarizations on the ratchet effect when a magnetic field is applied.
At the magnetic field strengths $B = \mp 3.9\,\mathrm{T}$, the photocurrents are measured upon rotation of the linearly polarized radiation in sample #1 as shown in Fig. 7.1 in (a) and (b), respectively. Both magnetic field values correspond to peaks in the magnetic quantum ratchet current, see Fig. 6.1 and the initially polarized radiation is aligned along the x-direction (perpendicular to the gate stripes) for the azimuthal angle $\alpha = 0$. Figure 7.1 demonstrates that by rotating the linear electric field orientation, the photocurrent changes its amplitude which can be well fitted by

$$J_x(B,\alpha) = J_x^{\mathrm{A}}(B)\cos(2\alpha) + J_x^{\mathrm{B}}(B)\sin(2\alpha) + J_x^{\mathrm{D}}(B)\,, \tag{7.1}$$

with the fitting parameters $J_x^{\mathrm{A}}(B)$, $J_x^{\mathrm{B}}(B)$ and $J_x^{\mathrm{D}}(B)$. These parameters depend on the sign and magnitude of the magnetic field applied but in addition

to it is similar to Eq. (5.1). Sample #1 demonstrates a large contribution of the polarization independent Seebeck ratchet current $J_x^{\mathrm{D}}(B)/P$ and, as this current has already been presented and discussed in Chap. 6, it will not be the focus in this chapter. As it is shown in Fig. 7.1 changing the lateral electrostatic potential from $U_{\mathrm{G1/G2}} = -0.5/0\,\mathrm{V}$ to $U_{\mathrm{G1/G2}} = 0/-0.5\,\mathrm{V}$ results in a sign change of the polarization dependent photocurrent. Similar to the polarization independent Seebeck contribution in Chap. 6, the asymmetry parameter Ξ does not change the positions of the oscillations maxima/ minima, which was demonstrated and proven in Fig. 6.5. The observation of this sign changing behavior when the lateral asymmetry is reversed is clear evidence that the polarization dependent photocurrent is also caused by the ratchet effect.

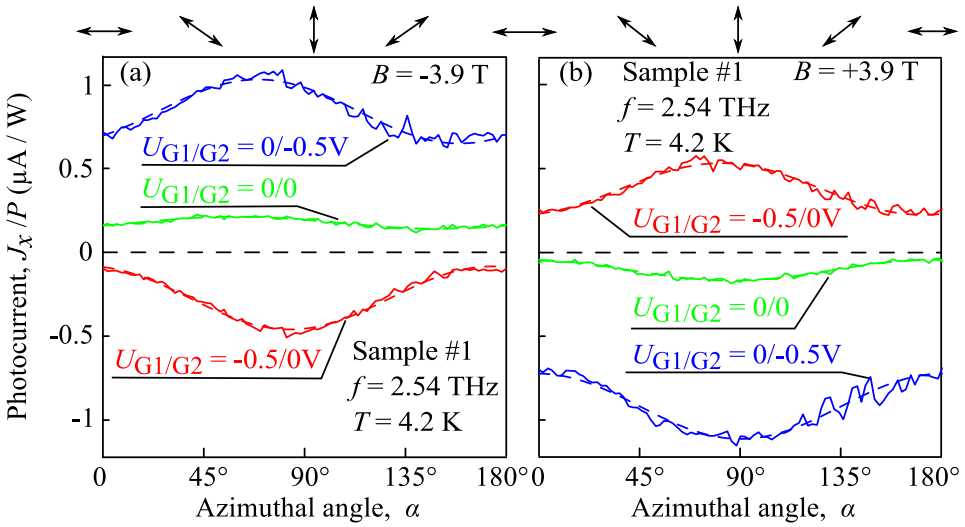

Figure 7.1: Normalized photocurrent J_x/P as a function of the azimuthal angle α measured in sample #1. The data are obtained for different lateral asymmetries $U_{\mathrm{G1/G2}} = -0.5/0\,\mathrm{V}$, $U_{\mathrm{G1/G2}} = 0/0$ and $U_{\mathrm{G1/G2}} = 0/-0.5\,\mathrm{V}$ at fixed magnetic field strengths, $B = -3.9\,\mathrm{T}$ and $+3.9\,\mathrm{T}$ in (a) and (b), respectively. The B-field values correspond to oscillation peaks in the magnetic field dependencies (see Fig. 6.1). Dashed curves are fits based on Eq. (7.1). The arrows on top illustrate the polarization plane orientation for several angles α.

Qualitative similar results for the dependence on the linear polarization are obtained in sample #2. In this sample, the total photocurrents J_x/P and J_y/P have similar magnitudes, but as an important difference the polarization independent current contribution $J_y^{\mathrm{D}}(B)/P$ is relatively small in y-direction.

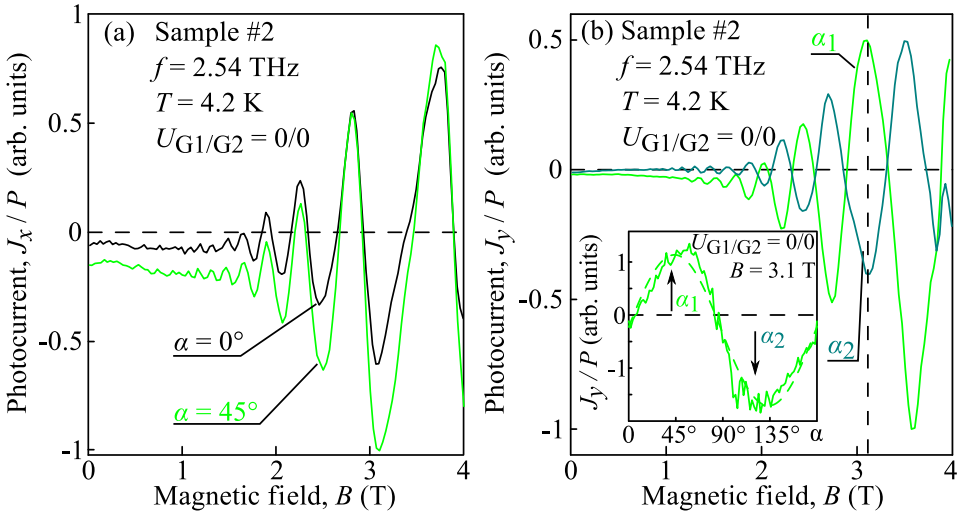

Figure 7.2: Magneto-oscillations of the normalized photocurrent J_x/P and J_y/P as a function of the magnetic field for two different azimuthal angles α measured in sample #2 in (a) and (b), respectively. The data are obtained for angles α at which the photocurrent approaches maximum/minimum values and for zero potential at both gates. The inset in (b) shows the normalized photocurrent J_y/P as a function of the azimuthal angle α measured at magnetic field $B = 3.1\,\mathrm{T}$, which corresponds to a peak of the magneto-oscillations, see the vertical dashed line.

The photocurrent J_x/P measured perpendicular to the stripes in sample #2 is dominated by the Seebeck ratchet effect and, therefore, the rotation of the linear polarization by the angle α only slightly influences the current amplitude without inverting the direction as shown in Fig. 7.2(a). In contrast to the x-direction, the photocurrent J_y/P has a dominating polarization dependent contribution, resulting in a sign change by rotating the linearly polarized radiation by $\approx 90°$ which is shown in Fig. 7.2(b) and in the inset. This inset shows the polarization dependence of the photocurrent J_y/P measured at a peak in the magneto-oscillations (see the vertically dashed line in Fig. 7.2(b)). It can

be seen that for zero potentials $U_{\mathrm{G1/G2}} = 0/0$ the photocurrent is dominated by the contribution $J_x^{\mathrm{B}}(B)\sin(2\alpha)$ and the polarization independent part is almost absent. Figure 7.2(b) further reveals that the magneto-oscillations of the photocurrent J_y/P have opposite signs for all peaks measured at the angles α_1 and α_2, which are marked in the inset.

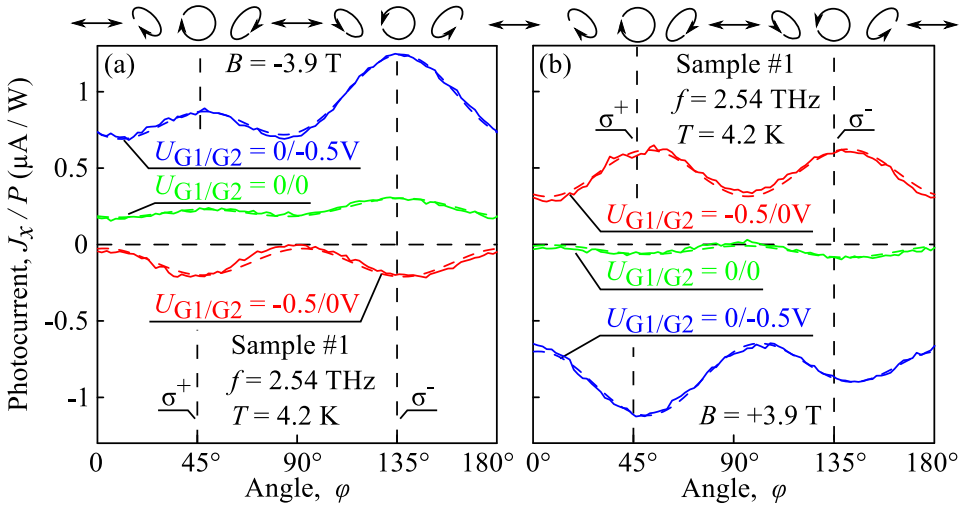

Figure 7.3: Normalized photocurrent J_x/P as a function of the angle φ defining the radiation polarization state, measured in sample #1 for magnetic field strengths $B = -3.9\,\mathrm{T}$ and $B = +3.9\,\mathrm{T}$ in (a) and (b), respectively. These values correspond to the magneto-oscillation peaks in Fig. 6.1. The data are presented for different gate voltage combinations $U_{\mathrm{G1/G2}}$. The symbols on top illustrate the polarization states for several values of φ. Vertical dashed lines indicate angles $\varphi = 45°$ for right-handed (σ^+) and $\varphi = 135°$ for left-handed (σ^-) circularly polarized radiation. The dashed curves are fits based on Eq. (7.2).

Also observed is the influence of the radiation helicity on the ratchet current generation which is investigated in the following section. Even though the Seebeck ratchet current dominates in sample #1, the photocurrent as dependence of the angle φ is observed in Fig. 7.3. The initially linearly polarized radiation is aligned parallel to the x-direction for $\varphi = 0$. The photocurrents J_x/P are

measured at two magnetic field strengths $B = \mp 3.9\,\mathrm{T}$ and can be well fitted by

$$J_x(B,\varphi) = J_x^{\mathrm{A}}(B)\frac{1+\cos(4\varphi)}{2} + J_x^{\mathrm{B}}(B)\frac{\sin(4\varphi)}{2} - J_x^{\mathrm{C}}(B)\sin(2\varphi) + J_x^{\mathrm{D}}(B), \quad (7.2)$$

where $J_x^{\mathrm{A}}(B)$, $J_x^{\mathrm{B}}(B)$, $J_x^{\mathrm{C}}(B)$ and $J_x^{\mathrm{D}}(B)$ are the fitting parameters, depending on the sign and magnitude of the magnetic field. It can be seen that a substantial contribution of the circular magneto-ratchet photocurrent can be detected which is revealed in the relatively large difference between the σ^+ and σ^- circularly polarized radiation for, e.g., $U_{\mathrm{G1/G2}} = 0/-0.5\,\mathrm{V}$ at $B = -3.9\,\mathrm{T}$ in Fig. 7.3(a).

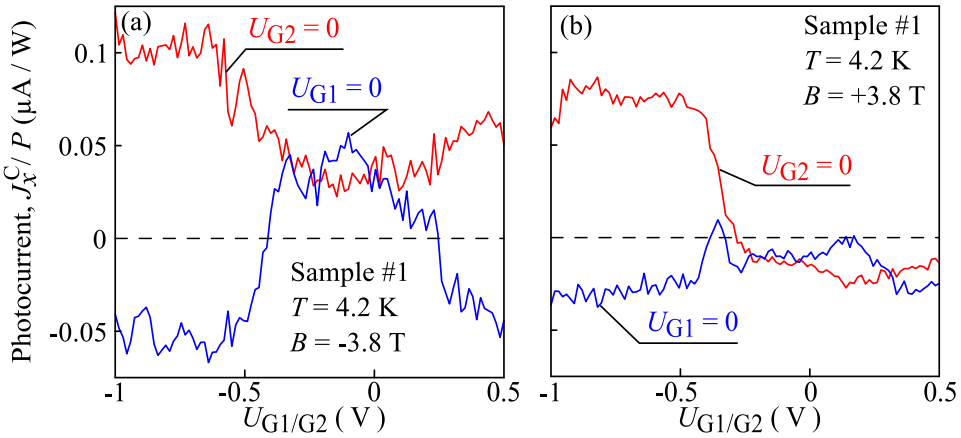

Figure 7.4: Dependencies of the normalized circular photocurrent contribution J_x^{C}/P obtained on the subgate voltage U_{G1} (U_{G2}) and zero subgate potentials U_{G2} (U_{G1}) for sample #1. The data in (a) and (b) are measured at peaks of the magneto-oscillation at $B = -3.8\,\mathrm{T}$ and $B = +3.8\,\mathrm{T}$, respectively. Peak positions are shown in Fig. 6.1.

In order to extract the pure circular photocurrent contribution, the photocurrents were measured for right- and left-handed circularly polarized radiation. For these polarization states, the linear contributions $J_{x,y}^{\mathrm{A}}(B)/P$ and $J_{x,y}^{\mathrm{B}}(B)/P$ vanish while the polarization independent contribution $J_{x,y}^{\mathrm{D}}(B)/P$ remains unchanged. By subtracting the currents measured with σ^+ and σ^- polarized radiation, $J_{x,y}^{\mathrm{D}}(B)/P$ is eliminated and the circular photocurrent contribution $J_{x,y}^{\mathrm{C}}(B)/P$ is obtained:

$$J_{x,y}^{\mathrm{C}}(B) = \left[J_{x,y}(B,\varphi = 45^\circ) - J_{x,y}(B,\varphi = 135^\circ)\right]/2. \quad (7.3)$$

This circular photocurrent contribution $J_x^{\mathrm{C}}(B)/P$ is depicted as a function of the gate voltage potentials at $B = \mp 3.8\,\mathrm{T}$ in Figs. 7.4(a) and (b), respectively. In both panels it can be seen that for $U_{\mathrm{G1/G2}} < -0.5\,\mathrm{V}$ a substantial contribution of the circular photocurrent is achieved which changes its direction when the gate voltage is switched between the thinner and thicker gate stripes. Fig. 7.4(a) shows that also for $U_{\mathrm{G1/G2}} > +0.2\,\mathrm{V}$ an amplitude increase and sign change can be obtained. This demonstrates that the lateral asymmetry parameter Ξ influences the amplitude and the sign of the circular photocurrent contribution and yields an evidence of the ratchet effect being the origin of the circular photocurrent contribution.

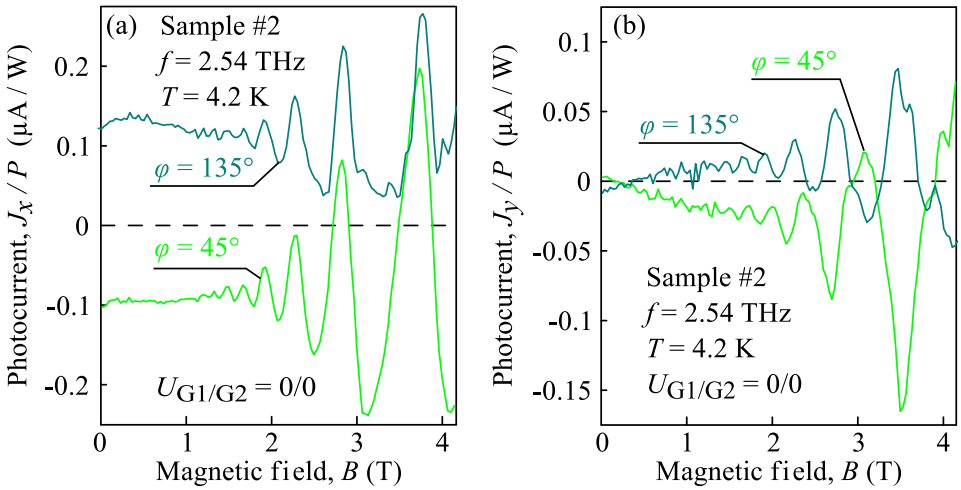

Figure 7.5: Magnetic field dependencies of the normalized photocurrent $J_{x,y}/P$ measured in sample #2 for zero gate voltages. The photocurrents J_x/P in (a) and J_y/P in (b) are obtained for right- ($\varphi = 45°$) and left- ($\varphi = 135°$) handed circularly polarized radiation.

The contribution of the circular photocurrent is - similar to the linear contribution - also more pronounced in sample #2 than in sample #1. This is due to the fact that, in sample #2, the polarization independent ratchet current is rather small. The total photocurrents J_x/P and J_y/P were measured as a function of the magnetic field B for right- and left-handed circularly polarized radiation and the results are shown in Fig. 7.5(a) and (b), respectively. It is observed that J_x/P only changes its sign by switching the radiation helicity at zero magnetic field, but the relative sign of the oscillations remains equal to

each other. In contrast, the photocurrent measured parallel to the gate stripes J_y/P has only a small helicity dependent current at $B = 0$, but the magneto-oscillations change their sign by switching the helicity from σ^+ ($\varphi = 45°$) to σ^- ($\varphi = 135°$) of the radiation.

To demonstrate the influence of the circular photocurrent component on the total photosignal generated, the current $J^{\mathrm{C}}_{x,y}(B)/P$, given by Eq. (7.3), is presented as a function of the magnetic field B for zero gates in Fig. 7.6. The figure shows that the pure circular contribution oscillates in the magnetic field and, for the current in y-direction, also changes its sign. In the inset of Fig. 7.6(a), the photocurrents in x- and y- directions are shown as a function of the angle φ for a fixed magnetic field, corresponding to a peak in the oscillations as shown in Fig. 7.5. It is clearly visible that the currents change sign when the polarization is switched between σ^+ and σ^-. These dependencies can be well fitted by Eq. (7.2).

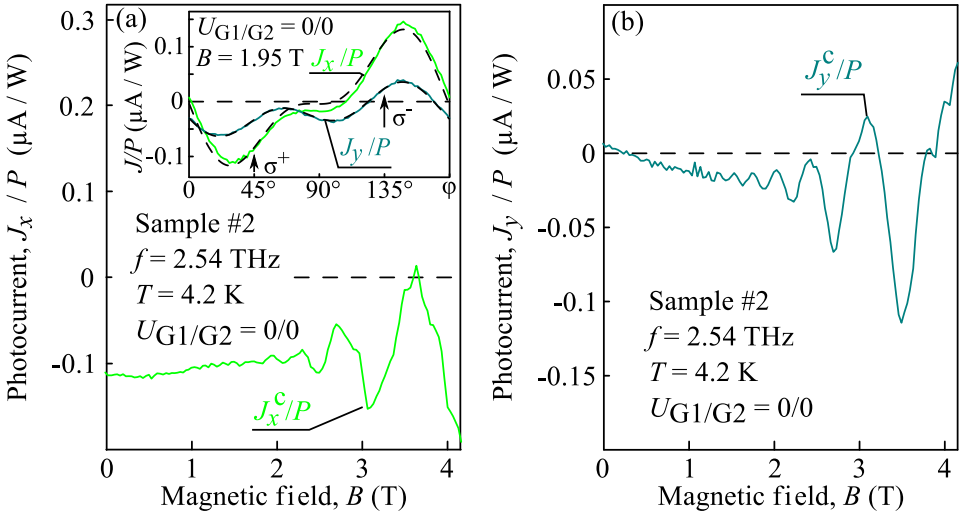

Figure 7.6: Normalized circular photocurrents $J^{\mathrm{C}}_{x,y}/P$ as a function of the magnetic field B measured in x- and y-directions in (a) and (b), respectively. The inset in (a) shows normalized total photocurrents J_x/P and J_y/P as a function of the angle φ. The data are obtained for magnetic field $B = 1.95\,\mathrm{T}$. The dashed lines are fits based on Eq. (7.2).

7.2 Microscopic Theory and Comparison with Experiments

The microscopic theory, based on the assumption of a quasi equilibrium Fermi-Dirac distribution, was developed by Prof. L. E. Golub and co-workers for describing the experimental data. This theory will be introduced and compared with the experimental results.

The polarization sensitive magnetic quantum ratchet theory utilizes the formalism for ratchet effects at zero magnetic field, proposed in Refs. [15, 16]. This theory is based on the time-dependent spatially periodic oscillation of the electron density $\delta N_\omega(x)\mathrm{e}^{-\mathrm{i}\omega t} + \text{c.c.} \equiv \delta N(x,t)$ which is linear both in the electric field $\boldsymbol{E}_\omega(x)$ and the lateral force $-\partial V(x)/\partial x$. In the following, the equations for the polarization sensitive magnetic quantum ratchet current are based on the working formula [15, 16]:

$$j_\alpha = \frac{\partial \sigma^0_{\alpha\beta}}{\partial N} \overline{\delta N_\omega(x) E^*_{\omega,\beta}(x)} + \text{c.c.} \tag{7.4}$$

Here $\sigma^0_{\alpha\beta}$ is the static conductivity tensor: $\sigma^0_{\alpha\beta} \equiv \sigma_{\alpha\beta}(\omega = 0)$, and the overline implies an average over the spatial coordinate x.

The currents were calculated for a simplified electric near-field $\boldsymbol{E}_\omega(x)$ and a static potential $V(x)$. As shown in Fig. 5.5, the near-field has a complex structure and also the electrostatic potential $V(x)$ can have a more complex modulation, giving rise to non-linear contributions in $V(x)$ [28]. To show the main features of the polarization sensitive magnetic quantum ratchet effect, it is sufficient to use the following equations to calculate the ratchet current equations:

$$\begin{aligned} \boldsymbol{E}_\omega(x) &= \boldsymbol{E}_0 \left[1 + h_1 \cos\left(\frac{2\pi}{d} x + \varphi_E \right) \right] , \\ V(x) &= V_1 \cos\left(\frac{2\pi}{d} x + \varphi_V \right) . \end{aligned} \tag{7.5}$$

These equations are the simplified form of the terms in Eq. (2.1) (similar to Ref. [15]).

Additionally, the following assumptions were made: The momentum scattering time τ is independent of the electron energy (see Ref. [15]) and these inequalities are satisfied:

$$E_\mathrm{F}\tau/\hbar \gg \omega\tau \gg \omega_c\tau \gg 1 \gg \mathrm{e}^{-\pi/(\omega_c\tau)} . \tag{7.6}$$

The Fermi energy $E_\mathrm{F} = 1.6\,\mathrm{eV}$ is extracted from the Shubnikov-de Haas oscillations and the electron scattering time $\tau = 0.54\,\mathrm{ps}$ from the mobility measurements. The laser radiation frequency ω is 15.96 THz and for $B = 2\,\mathrm{T}$, the cyclotron frequency is given by $\omega_c = 3.52\,\mathrm{THz}$ [82]. With the values from the experiments, the inequalities in Eq. (7.6) are given by $E_\mathrm{F}\tau/\hbar = 1310$, $\omega\tau = 8.6$, $\omega_c\tau = 1.9$ and $\mathrm{e}^{-\pi/(\omega_c\tau)} = 0.19$.
These assumptions together with the approximation of the electric field and lateral potential allow to calculated the equations for the polarization sensitive magnetic quantum ratchet effect which are given by

$$\begin{aligned} j_x =& \delta_s \Xi F \left[\omega\tau(s_0 + s_1) + \frac{B_z}{|B_z|} \left(\frac{3\omega}{2\omega_c} s_2 + \omega_c\tau s_3 \right) \right], \\ j_y =& \delta_s \Xi F \left[-\frac{3\omega}{2\omega_c} \frac{B_z}{|B_z|} (s_0 + s_1) + \omega\tau s_2 \right]. \end{aligned} \tag{7.7}$$

Here, the Stokes parameter $s_0 = |\hat{\boldsymbol{e}}_x|^2 + |\hat{\boldsymbol{e}}_y|^2$, $s_1 = |\hat{\boldsymbol{e}}_x|^2 - |\hat{\boldsymbol{e}}_y|^2$, $s_2 = \hat{\boldsymbol{e}}_x\hat{\boldsymbol{e}}_y^* + \hat{\boldsymbol{e}}_x^*\hat{\boldsymbol{e}}_y$ and $s_3 = -i(\hat{\boldsymbol{e}}_x\hat{\boldsymbol{e}}_y^* - \hat{\boldsymbol{e}}_x^*\hat{\boldsymbol{e}}_y)$ are given with the polarization unit vector $\hat{\boldsymbol{e}}$ of the electric near-field after passing through the metal grating. It should be mentioned that - in this case - s_0 is not the Seebeck ratchet current, caused by the electron gas heating, but the polarization independent term which is generated by the acceleration of electrons due to the time-dependent electric field. The remaining coefficients are given by

$$\begin{aligned} \delta_s &= \mathrm{e}^{-\pi/(\omega_c\tau)} \frac{z}{\sinh z} \sin\left(\frac{2\pi E_\mathrm{F}}{\hbar\omega_c} \right) \text{ with } z = \frac{2\pi^2 k_\mathrm{B} T}{\hbar\omega_c}, \\ F &= \frac{4e^3 E_\mathrm{F}}{m^*(\hbar\omega)^3\omega_c^3\tau^2}, \\ \Xi &= \overline{|\boldsymbol{E}_\omega(x)|^2 \frac{\partial V}{\partial x}}. \end{aligned}$$

The experimental results are described by this microscopic model with the structure asymmetry parameter Ξ as one of the parameters in Eq. (7.7). As shown in Chap. 5 and 6, this parameter predicts a sign change in the current for changing the applied asymmetry, which is generated by the voltages applied to the different gates. Exactly this behavior can be seen in Figs. 7.1 and 7.3. Both figures demonstrate that when the lateral asymmetry parameter is changed the current changes its amplitude and sign, providing a first evidence that the current is generated due to the ratchet effect. The parameter Ξ

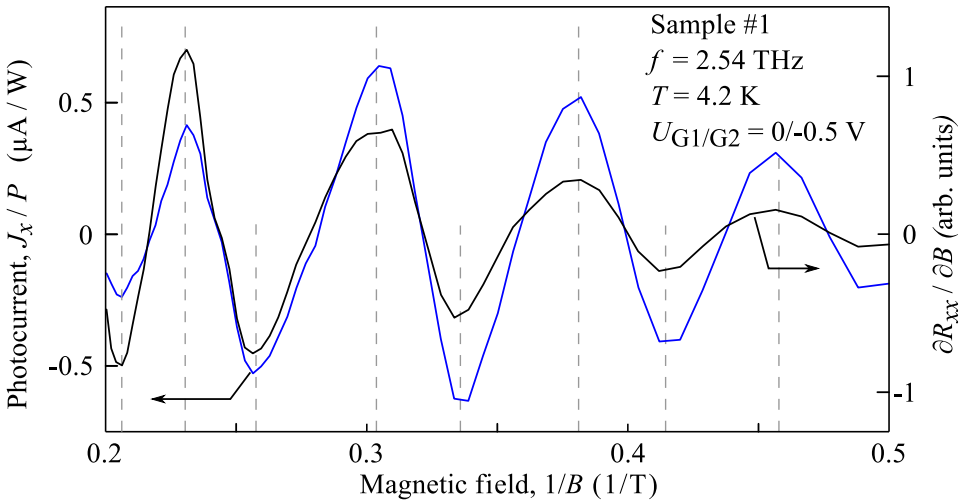

Figure 7.7: Normalized photocurrent J_x/P (blue) and derivative of longitudinal magneto-resistance $\partial R_{xx}/\partial B$ (black) as a function of the inverse magnetic field $1/B$ in (Cd,Mn)Te QW DGG sample #1 for the gate voltage combination $U_{\mathrm{G1/G2}} = 0/-0.5\,\mathrm{V}$. The vertical dashed lines indicate the extrema position of the photocurrent.

has also an influence on, for example, the circular photocurrent contribution $J_x^{\mathrm{C}}(B)/P \propto \delta_s \Xi \omega_c \tau s_3$. This is experimentally demonstrated in Fig. 7.4 which shows that the single contribution $J_x^{\mathrm{C}}(B)/P$ can be directly changed in the amplitude and the sign by variation of the asymmetry parameter. This demonstrates that the theory can well explain the amplitude and sign change of the ratchet currents in the experiments.

The ratchet currents are also proportional to δ_s (see Eq. (7.7)), which contains the derivative of the longitudinal magneto-resistance. Therefore, the polarization dependent ratchet current is supposed to have the same $1/B$-periodicity and its extrema positions are at the same magnetic field values as the extrema in the derivative of the Shubnikov-de Haas oscillations. These characteristics can be seen in Fig. 7.7, showing the photocurrent J_x/P and the derivative of the magneto-transport measurement $\partial R_{xx}/\partial B$ in a $1/B$-magnetic field dependence. It is demonstrated that the oscillations have the same periodicity and that the peaks of the oscillations are located at the same magnetic field values, providing a good accordance to the developed microscopy theory.

The following section is focused on the influence of the different polarization states of the radiation. The polarization dependencies of the ratchet currents, given in Eq. (7.7), are derived for the C_s symmetry group, assuming a reflection plane in xz-direction. The experiments, however, show contributions of all four Stokes parameters in both the x- and the y-directions, which was already observed for the ratchet currents at zero magnetic field and discussed in Chap. 5.2. For the description of the polarization sensitive magnetic quantum ratchet effect, the effective birefringence at the metal grating and the additional symmetry reduction to C_1 allow the superposition of all four Stokes parameter in both directions. Using the adjusted current equation, which is similar to Eq. (7.2), all data obtained can be well fitted, as it is shown in Figs. 7.1, 7.3 and in the insets of Figs. 7.2(b) and 7.6(a). These insets show that by changing the polarization the sign of the photocurrent is also inverted. Such behavior can be well described by the theory and indicates the ratchet effect as origin, because the change in the current direction cannot be achieved by modulation of the radiation power.

Also the oscillations of the magnetic quantum ratchet current are sensitive to the different polarizations, which is predicted by the theory $j_{x,y} \propto \delta_s s_{0,1,2,3}$ and experimentally proven in Figs. 7.2 and 7.5. These figures reveal that by changing the polarization state the current amplitude also changes. In Figs. 7.2(b) and 7.5(b) even a sign change of the direct current J_y/P is observed, which is well described by the theory. In contrast to the y-direction, the current J_x/P shows only variations in the amplitude, which can only partly be explained by the theory up to now. A possible explanation could be a strong influence of the Seebeck ratchet effect, which is not considered in Eq. (7.7) but this is not verified by now.

The circular contribution to the photocurrent $J^{C}_{x,y}(B)/P$ is oscillating with the same $1/B$-periodicity as R_{xx} and is also in phase with the derivative of the magneto-resistance oscillations as shown in Fig. 7.6. This behavior demonstrates that the current stems from the dual grating gate top structure and can be explained by the theory. It further proves the sensitivity of the magnetic quantum ratchet effect on the polarization state of the incident THz radiation.

It should be mentioned, that some of the contributions to the total photocurrent could arise from the edge effects similar to the photosignals in graphene flakes [80].

7.3 Brief Summary

The sensitivity of the magnetic quantum ratchet effect to the different polarization states of the incident radiation was experimentally demonstrated and the obtained results are well described by the microscopic theory, see Eq. (7.7). The theory was developed simultaneously to the experiments by the group of Prof. L. E. Golub and is based on the assumption of a quasi equilibrium Fermi-Dirac distribution.
The ratchet current was generated by utilizing an asymmetric interdigitated top gate superlattice on top of the CdTe and (Cd,Mn)Te quantum wells structures. These electric currents are generated by combinations of different polarization states of the terahertz electric field and the lateral asymmetry induced by the gate voltages applied to the DGG structure. The currents exhibit amplitude and sign changes by variation of the polarization states at fixed magnetic field values. The experiments further show that the magnetic quantum ratchet effect can be generated by, for example, right- and left-handed polarized radiation and changes the sign of the oscillations by switching between σ^+ and σ^- in the full magnetic field range. This behavior was observed in several samples for different gate voltage combinations. Further, the lateral asymmetry parameter Ξ can also change the amplitude and the sign of the polarization dependent photocurrent contributions, leading to a clear evidence for the magnetic quantum ratchet effect. The relation between the $1/B$ periodicity and the oscillation extrema positions in relation to the longitudinal magneto-resistance oscillations was demonstrated and is well explained by the theory.
The developed microscopy theory explains many effects observed in the experiments such as the polarization dependence, the periodicity, the extrema positions in relation to the magneto-resistance, the sign change due to the lateral asymmetry parameter Ξ and also the phase shift between the magnetic ratchet current oscillations and the Shubnikov-de Haas oscilations.

8 Helicity Sensitive THz Radiation Detection by InGaAs High Electron Mobility Transistors

This chapter presents the study of a radiation helicity sensitive photocurrent excited by THz radiation in a dual grating gate InAlAs/InGaAs/InAlAs/InP high electron mobility transistor. The basic physical principles are similar to the magnetic quantum ratchet effect (see Chaps. 5-7), as well as to the ratchet effect (see Chap. 2.1). Here, particular attention will be paid to the ratchet effect as a detector of the different radiation polarization states, which are, usually, not easy to detect electrically. It will be demonstrated that the structures investigated provide access to all Stokes parameters at room temperature. The results presented in this chapter are published in Ref. [70].

8.1 Experimental Results

The generated photocurrent j_x/I reveals a strong dependence on the radiation polarization state. The current was obtained by irradiating the structure with elliptically (circularly) polarized radiation at frequency $f = 2.54\,\mathrm{THz}$ under normal incidence at room temperature $T = 293\,\mathrm{K}$. In Fig. 8.1 the photocurrent is shown as a function of the angle φ and φ is illustrated with various symbols on top. The measurements were performed for the gate voltage combinations $U_{\mathrm{G1/G2}} = -1.06/0\,\mathrm{V}$ and $U_{\mathrm{G1/G2}} = 0/-0.9\,\mathrm{V}$. A crucial characteristic of the photocurrent is that, for right- (σ^+) and left-handed (σ^-) polarized radiation, the signs of the photocurrents j_x/I are reversed, i.e. at $\varphi = 45°$ and $\varphi = 135°$, respectively. The dependencies are well fitted by the equation

$$j_x(\varphi) = j_x^{\mathrm{A}} \frac{1+\cos(4\varphi)}{2} + j_x^{\mathrm{B}} \frac{\sin(4\varphi)}{2} - j_x^{\mathrm{C}} \sin(2\varphi) + j_x^{\mathrm{D}}, \tag{8.1}$$

which is a superposition of the Stokes parameters. The coefficients j_x^{A}, j_x^{B}, j_x^{C} and j_x^{D} are the fitting parameters for the Stokes parameters as stated in Chap. 5.1. The difference to the polarization dependencies shown in previous chapters is that the linearly polarized radiation is aligned parallel to the gate

stripes in y-direction for $\varphi = \alpha = 0$ in the following measurements, see the inset in Fig. 8.1.

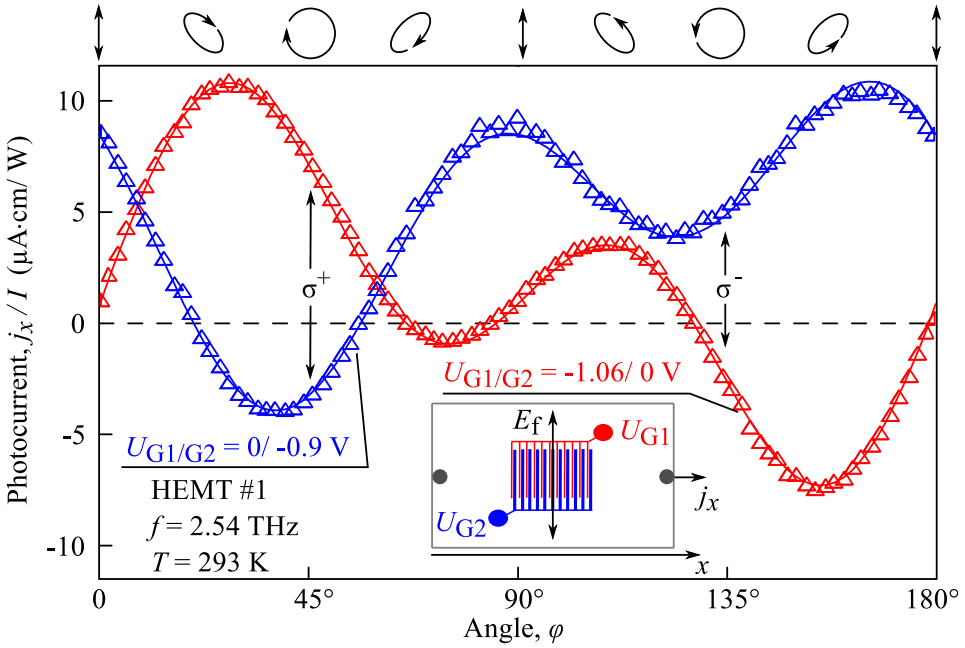

Figure 8.1: Dependencies of the THz radiation induced normalized photocurrent j_x/I on the radiation helicity, defined by the angle φ, for two different gate voltage combinations $U_{G1/G2} = -1.06/0\,\mathrm{V}$ and $U_{G1/G2} = 0/-0.9\,\mathrm{V}$ for the red and blue line, respectively. The data are obtained for sample HEMT #1 and the full lines are fits after Eq. (8.1). Various polarization states φ are illustrated on top. The inset shows a schematic diagram of the experimental setup. For $\varphi = 0$ the polarization of the electric field $\boldsymbol{E}_f$ is aligned perpendicular to the x-direction (parallel to the gate stripes) (adapted from Ref. [70]).

The polarization dependencies depicted in Fig. 8.1 were detected for arbitrary relations between the thinner gate G1 and the thicker gate G2. By interchanging the bias voltages applied to the gate fingers, the lateral potential asymmetry is inverted and results in a sign inversion of all contributions of the photocurrent, except the polarization independent offset j_x^D/I.

The dependencies of the individual contributions on the applied gate voltages are shown in Fig. 8.2. The contributions j_x^A/I, j_x^B/I and j_x^C/I are measured as a function of the gate voltage U_{G1} (U_{G2}) for zero biased second gate $U_{G2} = 0$

($U_{G1} = 0$) in Figs. 8.2(a) and (b), respectively. The photocurrent contributions have a maximum at $U_{G1} \approx -1.06\,\mathrm{V}$ and zero voltage at U_{G2} in Fig. 8.2(a). For the dependencies of the contributions for the second gate U_{G2}, the maximum is at $-0.9\,\mathrm{V}$ for $U_{G1} = 0$ as shown in Fig. 8.2(b). The polarization independent offset, represented by the coefficient j_x^D/I, will not be discussed in detail even though it was detected in all of the measurements presented. Here, the focus is on the currents driven by linearly polarized radiation - j_x^A/I and j_x^B/I - as well as on the helicity sensitive photocurrent j_x^C/I. The sign inversion of the contributions j_x^A/I, j_x^B/I and j_x^C/I can be seen in almost all values of U_{G1} compared to U_{G2} in Figs. 8.2(a) and (b), respectively. These figures clearly demonstrate that the lateral potential asymmetry influences the amplitude and the sign of the photocurrent contributions.

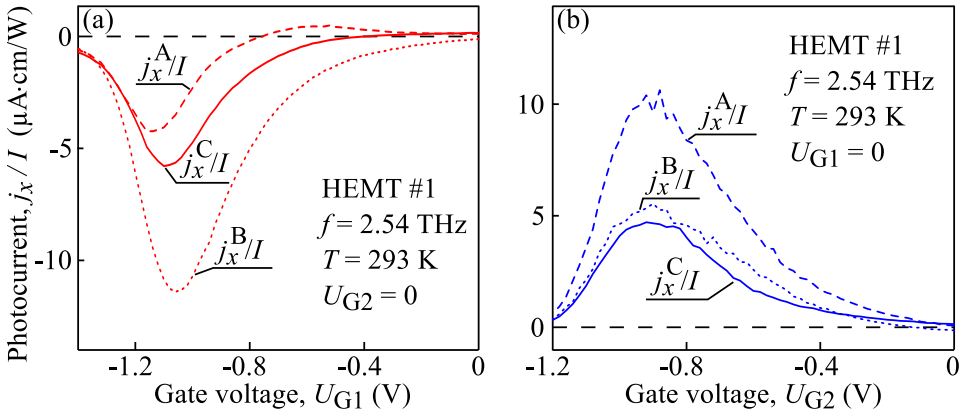

Figure 8.2: Normalized photocurrent contributions $j_x^{A,B,C}/I$ measured as a function of the gate voltage U_{G1} (U_{G2}) for zero potential on the other gate U_{G2} (U_{G1}) in (a) and (b), respectively for sample HEMT #1. The contribution j_x^C/I is driven by the radiation helicity and j_x^A/I , j_x^B/I are induced by the linear polarization (adapted from Ref. [70]).

A further observation is that one selected photocurrent contribution can be completely suppressed by choosing the appropriate relation between the amplitudes of the individual gate potentials. The three photocurrent contributions, j_x^A/I, j_x^B/I and j_x^C/I, are depicted as a function of the gate voltage U_{G1} for fixed $U_{G2} = -0.92\,\mathrm{V}$ in Fig. 8.3(a). The figure shows that the photocurrent contributions j_x^B/I and j_x^C/I change their sign when the amplitude of the gate

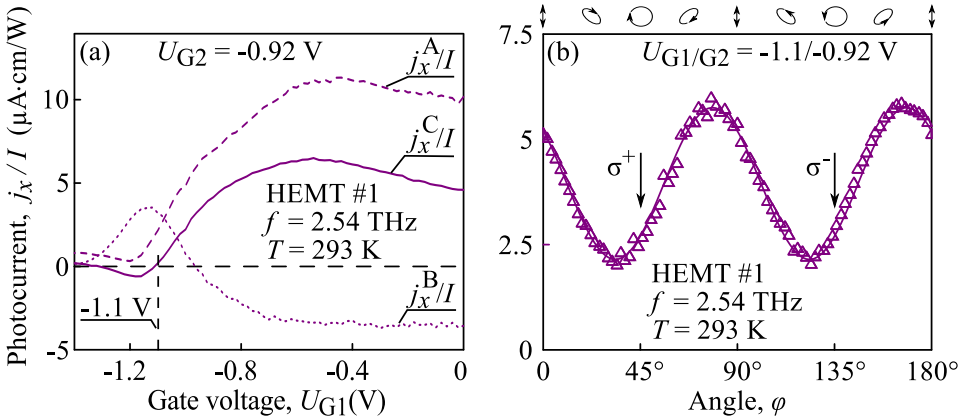

Figure 8.3: (a) shows the helicity sensitive photocurrent contribution j_x^{C}/I and the linear polarization sensitive photocurrent contributions j_x^{A}/I, j_x^{B}/I as a function of the gate voltage U_{G1} for fixed $U_{\mathrm{G2}} = -0.92\,\mathrm{V}$. The vertical dashed line indicates $U_{\mathrm{G1/G2}} = -1.1/-0.92\,\mathrm{V}$. The normalized photocurrent j_x/I as dependence of the angle φ defining the radiation helicity with applied gate voltage combination $U_{\mathrm{G1/G2}} = -1.1/-0.92\,\mathrm{V}$ is shown in (b). The fit to the total current calculated by Eq. (8.1) is illustrated as the full line. Various polarization states φ are illustrated on top (adapted from Ref. [70]).

voltage U_{G1} is increased for a non-zero second gate ($U_{\mathrm{G2}} = -0.92\,\mathrm{V}$). In addition, the sign inversion occurs at different gate voltages U_{G1}. Crucially, this behavior can be used to turn on and off the circular photocurrent contribution j_x^{C}/I which vanishes for the gate voltage combination $U_{\mathrm{G1/G2}} = -1.1/-0.92\,\mathrm{V}$ as shown in Fig. 8.3(b). In this dependency, a hardly existent amplitude difference in the photocurrent j_x/I is revealed for the two different helicity states, σ^+ and σ^-.

As addressed above, the photocurrent contributions j_x^{A}/I and j_x^{B}/I are caused by the degree of the linearly polarized radiation, see Eq. (8.1). Therefore, they can be induced by applying linearly polarized radiation. Figure 8.4(a) shows the gate dependencies of the normalized photocurrent j_x/I for several azimuthal angles α. The measurements were carried out on two different samples, HEMT #1 and #2, at a zero biased second gate ($U_{\mathrm{G2}} = 0$). It can be seen that, for different linear polarization states α, the photocurrent has different signs and amplitudes. The photocurrent j_x/I is shown as a function of the

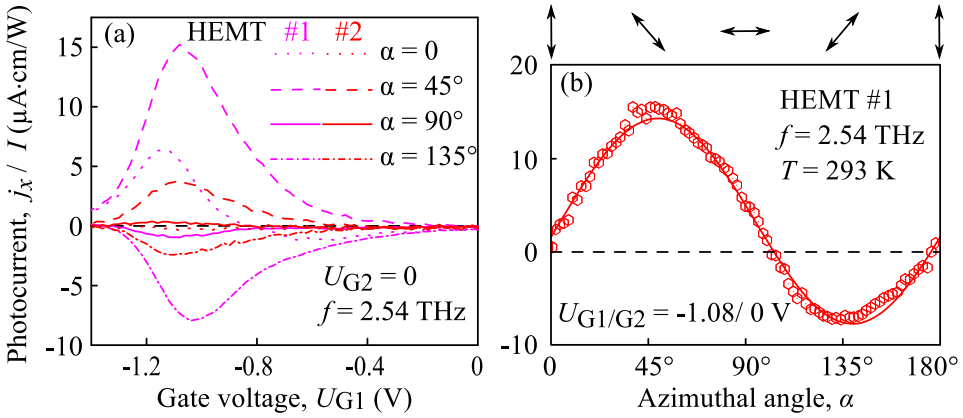

Figure 8.4: (a) shows the normalized photocurrent j_x/I excited by linearly polarized THz radiation in HEMT #1 and #2 as a function of the gate voltage U_{G1} for zero second gate $U_{G2} = 0$. Azimuthal angle α defines the in-plane orientation of the radiation electric field, with $\alpha = 0$ being parallel to the stripes (y-direction). The photocurrent j_x/I as dependence of the azimuthal angle α for $U_{G1/G2} = -1.08/0\,\mathrm{V}$ is depicted in (b). The total current is fitted by Eq. (8.2), see the full line as the fit curve. Electric field orientation is illustrated with arrows for several angles α at the top of the diagram (adapted from Ref. [70]).

azimuthal angle α for the gate voltage combination $U_{G1/G2} = -1.08/0\,\mathrm{V}$ in Fig. 8.4(b). This polarization dependence can be well fitted with a simplified Eq. (8.1)

$$j_x(\alpha) = j_x^{\mathrm{A}} \cos(2\alpha) + j_x^{\mathrm{B}} \sin(2\alpha) + j_x^{\mathrm{D}} \,, \tag{8.2}$$

under the consideration, that the circular term vanishes. The coefficients j_x^{A}, j_x^{B} and j_x^{D} which were used for fitting the data in Fig. 8.4(b), have the same sign and nearly the same amplitude as the parameters used for fitting the φ-dependencies for approximately the same gate voltage combinations as shown in Fig. 8.1 for example. Hence, the photocurrent contributions, j_x^{A}/I and j_x^{B}/I, are only controlled by the orientation of the linear polarization of the elliptically polarized radiation, which occurs by applying a $\lambda/4$-waveplate.

All of the samples measured with similar design and arbitrary relation between the first and second gate potential show a polarization sensitive photocurrent.

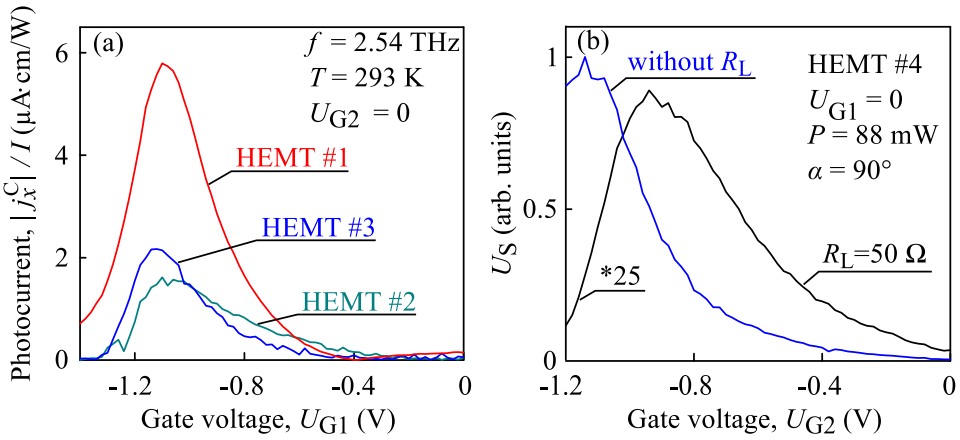

Figure 8.5: (a) shows amplitudes of the photocurrent contributions j_x^{C}/I measured as a function of the gate voltage U_{G1} for zero second gate, $U_{\mathrm{G2}} = 0$, in three different samples, HEMT #1, #2, and #3. (b) depicts the comparison between the photovoltage in HEMT #4 measured across a 50 Ω load resistance ($R_{\mathrm{L}} \ll R_{\mathrm{S}}$) and directly across the lock-in amplifier's input resistance $R_{\mathrm{A}} \gg R_{\mathrm{S}}$. The signal voltage U_{S} detected via 50 Ω load resistance was multiplied by factor 25 (adapted from Ref. [70]).

The photocurrents detected are always well fitted by Eq. (8.1). The helicity driven photocurrent j_x^{C}/I as a function of the gate potential U_{G1} for a zero second gate ($U_{\mathrm{G2}} = 0$) was measured in three different samples, HEMT #1, #2 and #3 as shown in Fig. 8.5(a). It can be seen that the maximum position of the photocurrent dependencies hardly differs, but the signal magnitudes are different for all samples studied.

It is to mention that the photocurrents depicted were measured in a closed circuit configuration, whereby the load resistance R_{L} was much smaller than the sample resistance R_{S} and, therefore, the photovoltage generated is only determined by R_{L} as shown in Eq. (3.3). The photosignals, which are obtained in the closed circuit configuration, show a non-monotonic behavior. This is caused by the interaction of the potential asymmetry and the sample resistance. Both rise when the gate voltage applied is increased due to an increase in the asymmetry and due to the gates converging to the threshold voltage of the HEMT. In an open circuit configuration, the signal is fed into the high input impedance of a lock-in amplifier. In this case, the maximum of the signal

is observed for gate voltages that are close to the threshold voltage U_{th}, see Fig. 8.5(b) [70].

The voltage responsivity R_{v} is a crucial characteristic for many detectors. Therefore, the voltages of the photosignal contribution U_x^{B} and U_x^{C} obtained in the open circuit configuration were taken for calculating R_{v} according to Ref. [23]:

$$R_{\mathrm{v}} = \frac{U_{\mathrm{S}}}{P}\frac{S}{S_{\mathrm{t}}}$$

Here, U_{S} is the photosignal voltage, P is the total power at the detector plane, S is the size of the radiation beam and $S_{\mathrm{t}} = 20 \times 20\,\mu\mathrm{m}^2$ is the transistor area. The responsivity for the linear photovoltage contribution U_x^{B} is $R_{\mathrm{v}} \approx 0.3\,\mathrm{V/W}$ and for the helicity sensitive contribution U_x^{C}, it is $R_{\mathrm{v}} \approx 0.15\,\mathrm{V/W}$. Typically the plasmonic FET detectors have higher voltage responsivities [23] than it was observed in the experiments for this thesis, meaning a further optimization of the structural design is necessary.

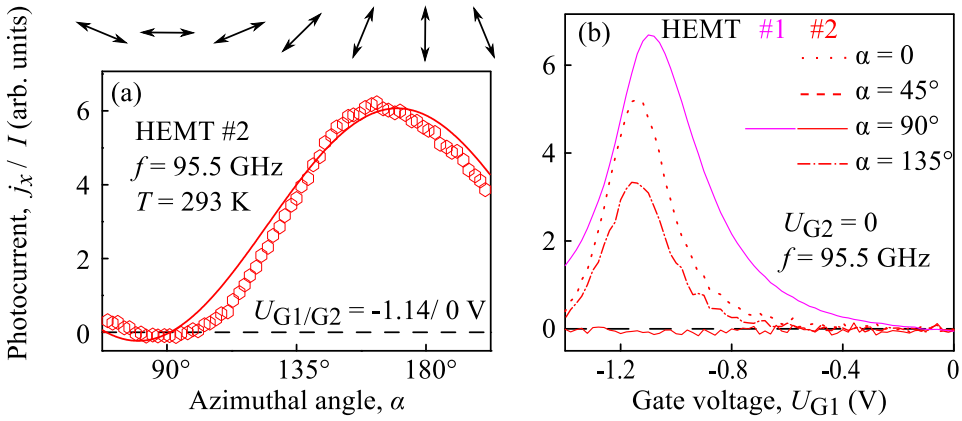

Figure 8.6: (a) shows dependence of j_x/I on the azimuthal angle α obtained in HEMT #2 for $U_{\mathrm{G1/G2}} = -1.14/0\,\mathrm{V}$ and $f = 95.5\,\mathrm{GHz}$. The full line is a fit curve after $j_x \propto \cos^2(\alpha + \theta)$ with the phase angle θ. (b) depicts the photocurrent j_x/I excited by linearly polarized microwave radiation in HEMT #1 and #2 as a function of the gate voltage U_{G1} ($U_{\mathrm{G2}} = 0$) (adapted from Ref. [70]).

The polarization dependencies change qualitatively for lower frequencies for example $f = 95.5\,\mathrm{GHz}$. The data obtained for microwave radiation have no more sign-alternating behavior as shown in Fig. 8.6(a). The signal varies after

$j_x \propto \cos^2(\alpha + \theta)$ with phase angle θ [85]. Figure 8.6(b) shows the photocurrent for different linear polarization states α as a function of the gate voltage U_{G1} for zero second gate $U_{\mathrm{G2}} = 0$. It reproduces the results obtained previously for similar structures, see Ref. [86]. The maximum photosignal in various samples is detected for different directions of the electric field vector in respect to the source-drain direction (x-direction) as shown by way of example for $\alpha = 90°$ in Fig. 8.6(b). This is attributed to the antenna coupling of the microwave radiation to the transistor [86].

8.2 Discussion

The results presented in Fig. 8.1, 8.3(a) and 8.4(b) demonstrate that the sign-alternating linear j_x^{B}/I and circular photocurrent j_x^{C}/I are caused by a microscopic process which goes beyond the plasmonic Dyakonov-Shur model [85]. The Dyakonov-Shur model is usually applied to explain the operation principle of FET THz detectors. As shown in Fig. 8.6(a), this model predicts that an oscillating electric field along the source-drain direction (x-direction) causes a sign conserving variation upon rotation of the linear polarization plane after $j_x \propto \cos^2(\alpha + \theta)$. This variation of the signal is proportional to the linear Stokes parameter s_1, excluding the offset. Therefore, the photocurrent contribution j_x^{A}/I can also be described by this polarization dependence. As shown in Refs. [87, 88], the circular photocurrent can be only explained by the Dyakonov-Shur model on the basis of an interference effect of two different channels and two interacting antennas. This model is made for small size specially designed FETs, which can hardly be applied to the large DGG samples used in the experiments.

As mentioned in Chap. 2.1, the electronic ratchet effect can describe the observation of the polarization behavior in asymmetric periodic structures [14–16,22] and also in linear/circular plasmonic ratchet effects [17, 19]. The ratchet effect can be explained by a phase shift between the periodic potential and the periodic radiation electric field. This phase shift is caused by the near-field diffraction in a system with broken symmetry. The photocurrent, which is sensitive to the helicity, appears because the carriers move in two directions and are subjected to the action of the two components $\boldsymbol{E}_x$, $\boldsymbol{E}_y$ of the electric

field in a laterally modulated quantum well [70]. This microscopic theory was developed in Ref. [22]. The theory depicted describes a system with a C_s point group symmetry, but, as already discussed in Chap. 5.2, the observed photocurrent j_x/I includes all individual contributions j_x^{D}/I, j_x^{A}/I, j_x^{B}/I and j_x^{C}/I. Therefore, the photocurrent can be described by Eq. (8.1) which is in good agreement with the experimental data shown in Figs. 8.1, 8.3(b) and 8.4(b).

Furthermore, the ratchet photocurrents are proportional to the lateral asymmetry parameter Ξ (see Chap. 2.1), therefore the inversion of the static potential asymmetry is supposed to reverse the sign of the photocurrents. Exactly this behavior is experimentally demonstrated in Figs. 8.1 and 8.2. When increased voltage is applied to one gate and the second is fixed, the rising signal amplitude can be well explained by the proportionality to the lateral asymmetry parameter. The interaction of the periodic modulation of the THz electric field and the lateral asymmetry causes complex gate-voltage dependencies, e.g. $U_{\mathrm{G1}} \approx U_{\mathrm{G2}}$ [70]. The total photocurrent consists of many individual contributions, which can include different microscopic mechanisms of the photocurrent generation. These individual contributions can change their behavior due to the variation of external parameters and, thus, the unique behavior can be used to distinguish them from each other. As a result, the photocurrent as a function of the gate voltage should obtain sign-alternating behavior. This was observed in the experiment, in particular for comparable gate voltages $U_{\mathrm{G1}} \approx U_{\mathrm{G2}}$, see Fig. 8.3.

The electronic or plasmonic ratchet effect can be enhanced by the resonant amplified near-field diffraction in a 2DEG at the plasmon resonance excitation. This has already been demonstrated for plasmonic ratchets in Refs. [19, 30]. The condition for the resonant plasmon effect ($\omega\tau > 1$, see Ref. [85]) is well satisfied in the samples used ($\omega\tau = 4$ at 2.54 THz). In similar structures, the fundamental plasmon resonance is excited at ≈ 2 THz, see Ref. [30]. Consequently, the ratchet effects observed can have contributions of the plasmon resonance excitations, but the contributions are independent of certain microscopic mechanisms of the ratchet photocurrent formation. The role of the plasmonic resonance excitation can be clarified by measurements in a broader THz frequency range.

8.3 Brief Summary

The results presented were obtained in dual grating gate InAlAs/InGaAs/InAlAs/InP high electron mobility transistors, which were irradiated by THz radiation. These measurements reveal a photocurrent, which is sensitive to the linearly or circularly polarized radiation. This current can be generated in HEMTs with an asymmetric lateral superlattice, consisting of thinner and thicker stripes. Moreover, the photosignal can be proportional to only one Stokes parameter by a proper choice of the bias voltages applied to the individual gates. This can be well described by the ratchet effect theory.
The lateral top gate has two effects: First, it induces a periodical potential, which acts on the 2DEG in the QW. Second, is modulates the incident radiation, due to the near-field effect. Both contributions lead to circular, linear, and polarization-independent ratchet effect at room temperature.
In the presented results, the responsivity of the polarization dependent signals was calculated. It is rather low compared to normal FET transistors and can be substantially improved by optimizing the design. This could lead to the resonant enhancement of the ratchet effect in the plasmon resonance excitation.

9 Conclusion

In the framework of this thesis, different magnetic quantum ratchet effects were firstly discovered which were generated by the excitation of dual grating gate samples with terahertz radiation in the presence of a magnetic field. These effects were observed in various CdTe and (Cd,Mn)Te samples with different parameters of the top gate structure. The observed magnetic quantum ratchet currents exhibit sign-changing magneto-oscillations with an amplitude by orders larger than the photocurrent at zero magnetic field. These oscillations are $1/B$-periodic and they are in phase with the derivative of the Shubnikov-de Haas oscillations. The current amplitude and direction were controllably changed by the variation of the lateral potential asymmetry parameter Ξ, induced by the voltages applied to the thinner or thicker gate stripes. Moreover, the amplitude and the sign of the current oscillations were altered by the in-plane orientation of the electric field in respect to the double grating gate structure for the linear magnetic ratchet effect or by the radiation helicity for the circular magnetic ratchet effect.

The photocurrent formation is well described in terms of the theory developed simultaneously to the experiments. Here, the lateral dual grating gate has two tasks: First, it induces a periodical lateral potential acting on the electrons in the quantum well and second, this grating modulates the incident radiation in the near-field and hence in the plane of the two-dimensional electron gas.
In fact, the generated photocurrent consists of three different contributions, namely the Seebeck (polarization independent), the linear and the circular magnetic quantum ratchet current. They are caused by different physical principles which will be briefly explained in the following. The polarization independent photocurrent is well described in terms of the semiclassical theory of the Seebeck magnetic ratchet effects. The observed effect is driven by the periodic modulation of the electron temperature in the two-dimensional electron gas which is caused by the local heating induced by the electrical near-field diffraction at the dual grating gate structure. The theory of the Seebeck ratchet effect in the presence of a quantizing magnetic field shows that the ratchet current follows the longitudinal magneto-resistance oscillations and the numerical calculations of the Seebeck ratchet current fit well to the experi-

mental data. The theoretical explanation of the polarization dependent ratchet currents considers the different polarization states of the radiation, the static conductivity tensor and the time-dependent spatially periodic electron density oscillations which are linear in both the electric field and the lateral potential. All considered mechanisms for explaining the magnetic ratchet effect were shown to be of orbital nature. As discussed in Ref. [29, 35, 36], spin ratchet effects may be generated in systems like the diluted magnetic semiconductor (Cd,Mn)Te. This material system was expected to reveal spin ratchet phenomena and was further studied by depositing dysprosium gate stripes on its surface, but all spin phenomena only contribute to the enhanced Zeeman splitting in the longitudinal magneto-resistance. The firstly discovered magnetic quantum ratchet effect is well explained by the developed theory without including spin properties at all.

The idea of building a detector based on the ratchet effect to detect different polarization states of the radiation was realized by applying terahertz radiation to dual grating gate InAlAs/InGaAs/In-AlAs/InP high electron mobility transistors resulting in a polarization sensitive photocurrent response at room temperature. This work demonstrates that high electron mobility transistors with an asymmetric lateral superlattice of gate fingers with unequal widths and spacing can be applied for generation of a photocurrent caused by linearly and circularly polarized radiation. Although the reported responsivity of field effect transistor detectors [23] is higher than the ones obtained in this work, the measured currents change their amplitude and sign by variation of the polarization states as well as by changing the lateral asymmetry parameter which was not observed up to now. Furthermore, the obtained photocurrents can be proportional to one selected Stokes parameter simply by variation of the voltages applied to the individual gates, offering new possibilities for detecting.

Appendix: Documentation of Processing

1. Sample Piece Preparation:

- original wafer piece (grown by Tomasz Wojtowicz from Institute of Physics, Polish Academy of Sciences, Warsaw, Poland) coating with optical resist (AR-P 3740) layer for protection against fragments
  Parameters for 1.5 μm layer thickness:
  covering the sample before starting with 3 drops of the optical resist
  - Phase 1: $3000 - 0 - 5$;
  - Phase 2: $6000 - 0 - 30$

- baking for 5 min at 90 °C

- breaking the wafer in small sample pieces (10×4 mm^2 or 4×4 mm^2) (parameters: force 4, scratched four times)

- standard cleaning parameters:
  - 1 h in 60 °C acetone bath
  - 5 min in fresh 90 °C acetone
  - 1 min in room temperature acetone
  - 30 s in iso-propanol at room temperature
  - blowing dry with nitrogen

2. Structuring the Surface:

- double-layer electron lithography resist:
  - Layer 1: PMMA 200 K 9% Anisol, baking: 15 min, 90 °C
  - Layer 2: PMMA 950 K 2% Anisol, baking: 15 min, 90 °C
  with the centrifugal sling parameters for both:
  - 3200/10000/5 s; 6 drops while running up
  - 6000/750/30 s; 6 drops within the first 10 s

- LEO REM parameters for the grating:
  - acceleration voltage 30 kV
  - working distance 14.2 mm

- aperture 30 μm
- area dose 200 μC for thicker gate stripes
- area dose 225 μC for thinner gate stripes

- LEO REM parameters for the supply pipes:
  - acceleration voltage 30 kV
  - working distance 14.2 mm
  - aperture 120 μm
  - area dose 200 μC

- development:
  - 40 s in MIBK:iso-propanol = 1:3
  - 5 s in iso-propanol
  - blowing dry with nitrogen

- for gold grating and its supply pipes:
  - Univex (base pressure $\approx 10^{-6}$ mbar)
  - 25 nm gold, $1.8 - 2.0$ $\mathring{A}$/s

- for dysprosium and gold grating:
  - sputtering (base pressure $\approx 10^{-9}$ mbar)
  - 75 nm dysprosium: 9 sccm argon flow, 50 W sputter power for 6 min 20 s
  - 15 nm gold: 7 sccm argon flow, 20 W sputter power for 2 min

- for supply pipes to connect the dysprosium and gold grating: (stripes height is larger than samples without dysprosium)
  - Univex (base pressure $\approx 10^{-6}$ mbar)
  - 100 nm gold, $1.8 - 2.0$ $\mathring{A}$/s

- lift-off in both cases in acetone at 60 °C for at least $\approx$ 12 h

- standard cleaning

3. Ohmic Contacts

- scratching contact area with needle smoothly several times to break up oxide and cap layer

- press fresh cut indium pieces (purity $\approx 99\%$) on the scratched area
- press for ≈ 7 s soldering iron in indium piece (temperature $\approx 300\,^{\circ}\mathrm{C}$)
- checking ohmic quality at point probe station
- if bad ohmic behavior, repeat heating with soldering iron for 3 s

4. Contacting gates

- mixing of Epoxy Technology Silver Paste (two components A : B = 1 : 1)
- take a thin needle and pick up a very small portion of the mixture
- put one drop on the contact pad for the grating
- press a gold - wire into the doughy liquid
- dry out in Annealing Oven at $\approx 40\,^{\circ}\mathrm{C}$ for 12 h

References

[1] F. Jülicher, A. Ajdari, and J. Prost, *Modeling molecular motors*, Rev. Mod. Phys. **69**, 1269 (1997).

[2] P. Reimann, *Brownian motors: noisy transport far from equilibrium*, Phys. Rep. **361**, 57 (2002).

[3] H. Linke, T. E. Humphrey, P. E. Lindelof, A. Löfgren, R. Newbury, P. Omling, A. O. Sushkov, R. P. Taylor, and H. Xu, *Quantum ratchets and quantum heat pumps*, Appl. Phys. A: Mater. Sci. Process. **75**, 237 (2002).

[4] P. Hänggi and F. Marchesoni, *Artificial Brownian motors: Controlling transport on the nanoscale*, Rev. Mod. Phys. **81**, 387 (2009).

[5] S. Denisov, S. Flach, and P. Hänggi, *Tunable transport with broken space-time symmetries*, Phys. Rep. **538**, 77 (2014).

[6] M. Büttiker, *Transport as a Consequence of State-Dependent Diffusion*, Z. Phys. B **68**, 161 (1987).

[7] Ya. M. Blanter and M. Büttiker, *Rectification of fluctuations in an underdamped ratchet*, Phys. Rev. Lett. **81**, 4040 (1998).

[8] P. Reimann, M. Grifoni, and P. Hänggi, *Quantum Ratchets*, Phys. Rev. Lett. **79**, 1 (1997).

[9] A. Lorke, S. Wimmer, B. Jager, J. P. Kotthaus, W. Wegscheider, and M. Bichler, *Far-infrared and transport properties of antidot arrays with broken symmetry*, Physica B **249**, 312 (1998).

[10] A. M. Song, P. Omling, L. Samuelson, W. Seifert, and I. Shorubalko, *Room-temperature and 50 GHz operation of a functional nanomaterial*, Appl. Phys. Lett. **79**, 1357 (2001).

[11] A. D. Chepelianskii, M. V. Entin, L. I. Magarill, and D. L. Shepelyansky, *Photogalvanic current in artificial asymmetric nanostructures*, Eur. Phys. J. B **56**, 323 (2007).

[12] A. D. Chepelianskii, M. V. Entin, L. I. Magarill, and D. L. Shepelyansky, *Theory of photogalvanic effect in asymmetric nanostructure arrays*, Physica E **40**, 1264 (2008).

[13] S. Sassine, Yu. Krupko, J.-C. Portal, Z. D. Kvon, R. Murali, K. P. Martin, G. Hill, and A. D. Wieck, *Experimental investigation of the ratchet effect in a two-dimensional electron system with broken spatial inversion symmetry*, Phys. Rev. B **78**, 045431 (2008).

[14] P. Olbrich, E. L. Ivchenko, R. Ravash, T. Feil, S. D. Danilov, J. Allerdings, D. Weiss, D. Schuh, W. Wegscheider, and S. D. Ganichev, *Ratchet Effects Induced by Terahertz Radiation in Heterostructures with a Lateral Periodic Potential*, Phys. Rev. Lett. **103**, 090603 (2009).

[15] E. L. Ivchenko and S. D. Ganichev, *Ratchet Effects in Quantum Wells with a Lateral Superlattice*, JETP Letters **93**, 673 (2011).

[16] A. V. Nalitov, L. E. Golub, and E. L. Ivchenko, *Ratchet effects in two-dimensional systems with a lateral periodic potential*, Phys. Rev. B **86**, 115301 (2012).

[17] V. V. Popov, *Terahertz rectification by periodic two-dimensional electron plasma*, Appl. Phys. Lett. **102**, 253504 (2013).

[18] S. V. Koniakhin, *Ratchet effect in graphene with trigonal clusters*, Eur. Phys. J. B **87**, 216 (2014).

[19] I. V. Rozhansky, V. Yu. Kachorovskii, and M. S. Shur, *Helicity-Driven Ratchet Effect Enhanced by Plasmons*, Phys. Rev. Lett. **114**, 246601 (2015).

[20] V. V. Popov, D. V. Fateev, E. L. Ivchenko, and S. D. Ganichev, *Noncentrosymmetric plasmon modes and giant terahertz photocurrent in a two-dimensional plasmonic crystal*, Phys. Rev. B **91**, 235436 (2015).

[21] W. Weber, L. E. Golub, S. N. Danilov, J. Karch, C. Reitmaier, B. Wittmann, V. V. Bel'kov, E. L. Ivchenko, Z. D. Kvon, N. Q. Vinh, A. F. G. van der Meer, B. Murdin, and S. D. Ganichev, *Quantum ratchet*

effects induced by terahertz radiation in GaN-based two-dimensional structures, Phys. Rev. B **77**, 245304 (2008).

[22] P. Olbrich, J. Karch, E. L. Ivchenko, J. Kamann, B. März, M. Fehrenbacher, D. Weiss, and S. D. Ganichev, *Classical ratchet effects in heterostructures with a lateral periodic potential*, Phys. Rev. B **83**, 165320 (2011).

[23] T. Watanabe, S. A. Boubanga-Tombet, Y. Tanimoto, D. Fateev, V. Popov, D. Coquillat, W. Knap, Y. M. Meziani, Y. Wang, H. Minamide, H. Ito, and T. Otsuji, *InP- and GaAs-Based Plasmonic High-Electron-Mobility Transistors for Room-Temperature Ultrahigh-Sensitive Terahertz Sensing and Imaging*, IEEE Sens. J. **13**, 89 (2013).

[24] Y. Kurita, G. Ducournau, D. Coquillat, A. Satou, K. Kobayashi, S. Boubanga Tombet, Y. M. Meziani, V. V. Popov, W. Knap, T. Suemitsu, and T. Otsuji, *Ultrahigh sensitive sub-terahertz detection by InP-based asymmetric dual-grating-gate high-electron-mobility transistors and their broadband characteristics*, Appl. Phys. Lett. **104**, 251114 (2014).

[25] S. Boubanga-Tombet, Y. Tanimoto, A. Satou, T. Suemitsu, Y. Wang, H. Minamide, H. Ito, D. V. Fateev, V. V. Popov, and T. Otsuji, *Current-driven detection of terahertz radiation using a dual-grating-gate plasmonic detector*, Appl. Phys. Lett. **104**, 262104 (2014).

[26] E. S. Kannan, I. Bisotto, J.-C. Portal, T. J. Beck, and L. Jalabert, *Energy free microwave based signal communication using ratchet effect*, Appl. Phys. Lett. **101**, 143504 (2012).

[27] C. Drexler, S. A. Tarasenko, P. Olbrich, J. Karch, M. Hirmer, F. Müller, M. Gmitra, J. Fabian, R. Yakimova, S. Lara-Avila, S. Kubatkin, M. Wang, R. Vajtai, P. M. Ajayan, J. Kono, and S. D. Ganichev, *Magnetic quantum ratchet effect in graphene*, Nat. Nanotechnol. **8**, 104 (2013).

[28] P. Olbrich, J. Kamann, M. König, J. Munzert, L. Tutsch, J. Eroms, D. Weiss, M.-H. Liu, L. E. Golub, E. L. Ivchenko, V. V. Popov, D. V. Fateev, K. V. Mashinsky, F. Fromm, Th. Seyller, and S. D. Ganichev, *Terahertz ratchet effects in graphene with a lateral superlattice*, Phys. Rev. B **93**, 075422 (2016).

[29] S. Smirnov, D. Bercioux, M. Grifoni, and K. Richter, *Quantum Dissipative Rashba Spin Ratchets*, Phys. Rev. Lett. **100**, 230601 (2008).

[30] V. V. Popov, D. V. Fateev, T. Otsuji, Y. M. Meziani, D. Coquillat, and W. Knap, *Plasmonic terahertz detection by a double-grating-gate field-effect transistor structure with an asymmetric unit cell*, Appl. Phys. Lett. **99**, 243504 (2011).

[31] T. Otsuji, M. Hanabe, T. Nishimura, and E. Sano, *A grating-bicoupled plasma-wave photomixer with resonant-cavity enhanced structure*, Opt. Express **14**, 4815 (2006).

[32] D. Coquillat, S. Nadar, F. Teppe, N. Dyakonova, S. Boubanga-Tombet, W. Knap, T. Nishimura, T. Otsuji, Y. M. Meziani, G. M. Tsymbalov, and V. V. Popov, *Room temperature detection of sub-terahertz radiation in double-grating-gate transistors*, Opt. Express **18**, 6024 (2010).

[33] V. V. Popov, *Plasmon Excitation and Plasmonic Detection of Terahertz Radiation in the Grating-Gate Field-Effect-Transistor Structures*, J. Infrared Millimeter THz Waves **32**, 1178 (2011).

[34] G. C. Dyer, G. R. Aizin, J. L. Reno, E. A. Shaner, and S. J. Allen, *Novel Tunable Millimeter-Wave Grating-Gated Plasmonic Detectors*, IEEE J. Sel. Top. Quantum Electronics **17**, 85 (2011).

[35] G. V. Budkin, L. E. Golub, E. L. Ivchenko, and S. D. Ganichev, *Magnetic Ratchet Effects in a Two-Dimensional Electron Gas*, JETP Lett. **104**, 649 (2016).

[36] G. V. Budkin and L. E. Golub, *Orbital magnetic ratchet effect*, Phys. Rev. B **90**, 125316 (2014).

[37] P. Faltermeier, G. V. Budkin, J. Unverzagt, S. Hubmann, A. Pfaller, V. V. Bel'kov, L. E. Golub, E. L. Ivchenko, Z. Adamus, G. Karczewski, T. Wojtowicz, V. V. Popov, D. V. Fateev, D. A. Kozlov, D. Weiss, and S. D. Ganichev, *Magnetic quantum ratchet effect in (Cd,Mn)Te- and CdTe-based quantum well structures with a lateral asymmetric superlattice*, Phys. Rev. B **95**, 155442 (2017).

[38] J. H. Davies, *The Physics of Low-Dimensional Semiconductors*. Cambridge University Press, Cambridge, 2005.

[39] T. Ihn, *Semiconductor Nanostructures*. Oxford University Press, Oxford, 2010.

[40] C. Kittel, *Einführung in die Festkörperphysik*. Oldenburg Verlag, München, 1973.

[41] K. v. Klitzing, *The Quantized Hall Effect*, Physica B **126**, 242 (1984).

[42] T. Ando, A. B. Fowler, and F. Stern, *Electronic properties of two-dimensional systems*, Rev. Mod. Phys. **54**, 437 (1982).

[43] B. Laikhtman and E. L. Altshuler, *Quasiclassical Theory of Shubnikov-de Haas Effect in 2D Electron Gas*, Ann. Phys. **232**, 332 (1994).

[44] M. K. Kneip, D. R. Yakovlev, M. Bayer, G. Karczewski, T. Wojtowicz, and J. Kossut, *Engineering of spin-lattice relaxation dynamics by digital growth of diluted magnetic semiconductor CdMnTe*, Appl. Phys. Lett. **88**, 152105 (2006).

[45] J. K. Furdyna, *Diluted magnetic semiconductors*, J. Appl. Phys. **64**, R29 (1988).

[46] J. Kossut and J. A. Gaj, eds., *Introduction to the Physics of Diluted Magnetic Semiconductors*. Springer, Berlin, 2010.

[47] P. Olbrich, C. Zoth, P. Lutz, C. Drexler, V. V. Bel'kov, Ya. V. Terent'ev, S. A. Tarasenko, A. N. Semenov, S. V. Ivanov, D. R. Yakovlev, T. Wojtowicz, U. Wurstbauer, D. Schuh, and S. D. Ganichev,

Spin-polarized electric currents in diluted magnetic semiconductor heterostructures induced by terahertz and microwave radiation, Phys. Rev. B **86**, 085310 (2012).

[48] F. K. Kneubühl and M. W. Sigrist, *Laser*. Teubner, Leipzig, 1999.

[49] S. D. Ganichev and W. Prettl, *Intense Terahertz Excitation of Semiconductors*. Oxford Univ. Press, Oxford, 2006.

[50] P. Olbrich, *THz radiation induced spin polarized currents in low dimensional semiconductor structures*. PhD thesis, University of Regensburg, 2010.

[51] J. B. Gunn, *Microwave oscillations of current in III-V semiconductors*, Solid State Comm. **1**, 88 (1963).

[52] S. M. Sze, *Physics of Semiconductor Devices*, vol. 2. Wiley-Interscience Publication, USA, 1981.

[53] M. Shur, *Introduction to Electronic Devices*. Hamilton Printing Co, USA, 1996.

[54] B. E. A. Saleh and M. C. Teich, *Fundamentals of Photonics*. John Wiley and Sons, Inc., New York, 2007.

[55] S. D. Ganichev, W. Weber, J. Kiermaier, S. N. Danilov, P. Olbrich, D. Schuh, W. Wegscheider, D. Bougeard, G. Abstreiter, and W. Prettl, *All-electric detection of the polarization state of terahertz laser radiation*, J. Appl. Phys. **103**, 114504 (2008).

[56] M. Born and E. Wolf, *Principles of Optics*. Pergamon Press, Oxford, 1964.

[57] S. N. Danilov, B. Wittmann, P. Olbrich, W. Eder, W. Prettl, L. E. Golub, E. V. Beregulin, Z. D. Kvon, N. N. Mikhailov, S. A. Dvoretsky, V. A. Shalygin, N. Q. Vinh, A. F. G. van der Meer, B. Murdin, and S. D. Ganichev, *Fast detector of the ellipticity of infrared and terahertz radiation based on HgTe quantum well structures*, J. Appl. Phys. **105**, 013106 (2009).

[58] W. Menz and P. Bley, eds., *Mikrosystemtechnik für Ingenieure*. VCH-Verlagsgesellschaft, Weinheim, 1993.

[59] J. Vossen and W. Kern, eds., *Thin film processes*. Academic Press, San Diego, 1978.

[60] D. Widmann, H. Mader, and H. Friedrich, *Technologie hochintegrierter Schaltungen*. Springer, Berlin, 1996.

[61] S. A. Crooker, D. A. Tulchinsky, J. Levy, D. D. Awschalom, R. Garcia, and N. Samarth, *Enhanced Spin Interactions in Digital Magnetic Heterostructures*, Phys. Rev. Lett. **75**, 505 (1995).

[62] J. C. Egues and J. W. Wilkins, *Spin-dependent phenomena in digital-magnetic heterostructures: Clustering and phase-space filling effects*, Phys. Rev. B **58**, R16012(R) (1998).

[63] J. Jaroszyński, T. Andrearczyk, G. Karczewski, J. Wróbel, T. Wojtowicz, E. Papis, E. Kamińska, A. Piotrowska, D. Popović, and T. Dietl, *Ising Quantum Hall Ferromagnet in Magnetically Doped Quantum Wells*, Phys. Rev. Lett. **89**, 266802 (2002).

[64] S. D. Ganichev, S. A. Tarasenko, V. V. Bel'kov, P. Olbrich, W. Eder, D. R. Yakovlev, V. Kolkovsky, W. Zaleszczyk, G. Karczewski, T. Wojtowicz, and D. Weiss, *Spin Currents in Diluted Magnetic Semiconductors*, Phys. Rev. Lett **102**, 156602 (2009).

[65] M. Staab, M. Matuschek, P. Pereyra, M. Utz, D. Schuh, D. Bougeard, R. R. Gerhardts, and D. Weiss, *Commensurability oscillations in a lateral superlattice with broken inversion symmetry*, New J. Phys. **17**, 043035 (2015).

[66] M. A. Seo, H. R. Park, S. M. Koo, D. J. Park, J. H. Kang, O. K. Suwal, S. S. Choi, P. C. M. Planken, G. S. Park, N. K. Park, Q. H. Park, and D. S. Kim, *Terahertz field enhancement by a metallic nano slit operating beyond the skin-depth limit*, Nat. Photonics **3**, 152 (2009).

[67] J. Biberger, *Transportphänomene in mesoskopischen 2DEG-Strukturen unter dem Einfuss inhomogener Streufelder von Nanomagneten.* PhD thesis, University of Regensburg, 2007.

[68] S. Weishäupl, *Quanteninterferenzeffekte in topologischen Isolatoren und magnetischen Halbleitern.* PhD thesis, University of Regensburg, 2014.

[69] C. Betthausen, *Transportexperimente an semimagnetischen CdMnTe/ CdMgTe-Heterostrukturen*, diploma thesis, University of Regensburg, 2007.

[70] P. Faltermeier, P. Olbrich, W. Probst, L. Schell, T. Watanabe, S. A. Boubanga-Tombet, T. Otsuji, and S. D. Ganichev, *Helicity sensitive terahertz radiation detection by dual-grating-gate high electron mobility transistors*, J. Appl. Phys. **118**, 084301 (2015).

[71] T. Enoki, H. Yokoyama, Y. Umeda, and T. Otsuji, *Ultrahigh-Speed Integrated Circuits Using InP-Based HEMTs*, Jpn. J. Appl. Phys. **37**, 1359 (1998).

[72] D. Nguyen, K. Hogan, A. Blew, and M. Cordes, *Improved process control, lowered costs and reduced risks through the use of non-destructive mobility and sheet carrier density measurements on GaAs and GaN wafers*, J. Cryst. Growth **272**, 59 (2004).

[73] D. V. Fateev, V. V. Popov, and M. S. Shur, *Transformation of the Plasmon Spectrum in a Grating-Gate Transistor Structure with Spatially Modulated Two-Dimensional Electron Channel*, Semicond. **44**, 1406 (2010).

[74] T. Kawamura, S. Das Sarma, R. Jalabert, and J. K. Jain, *Low-temperature energy relaxation in* $Al_xGa_{1-x}As/GaAs$ *heterojunctions*, Phys. Rev. B **42**, 5407(R) (1990).

[75] E. L. Ivchenko and M. I. Petrov, *Near field of Terahertz Radiation Transmitted through a Lateral Non-Centrosymmetric Grating*, Phys. Solid State **56**, 1833 (2014).

[76] B. Wittmann, S. N. Danilov, V. V. Bel'kov, S. A. Tarasenko, E. G. Novik, H. Buhmann, C. Brüne, L. W. Molenkamp, Z. D. Kvon, N. N. Mikhailov, S. A. Dvoretsky, N. Q. Vinh, A. F. G. van der Meer, B. Murdin, and S. D. Ganichev, *Circular photogalvanic effect in HgTe/CdHgTe quantum well structures*, Semicond. Sci. Technol. **25**, 095005 (2010).

[77] V. V. Bel'kov and S. D. Ganichev, *Magneto-gyrotropic effects in semiconductor quantum wells*, Semicond. Sci. Technol. **23**, 114003 (2008).

[78] K.-M. Dantscher, D. A. Kozlov, P. Olbrich, C. Zoth, P. Faltermeier, M. Lindner, G. V. Budkin, S. A. Tarasenko, V. V. Bel'kov, Z. D. Kvon, N. N. Mikhailov, S. A. Dvoretsky, D. Weiss, B. Jenichen, and S. D. Ganichev, *Cyclotron-resonance-assisted photocurrents in surface states of a three-dimensional topological insulator based on a strained high-mobility HgTe film*, Phys. Rev. B **92**, 165314 (2015).

[79] J. Karch, C. Drexler, P. Olbrich, M. Fehrenbacher, M. Hirmer, M. M. Glazov, S. A. Tarasenko, E. L. Ivchenko, B. Birkner, J. Eroms, D. Weiss, R. Yakimova, S. Lara-Avila, S. Kubatkin, M. Ostler, T. Seyller, and S. D. Ganichev, *Terahertz Radiation Driven Chiral Edge Currents in Graphene*, Phys. Rev. Lett. **107**, 276601 (2011).

[80] M. M. Glazov and S. D. Ganichev, *High frequency electric field induced nonlinear effects in graphene*, Phys. Rep. **535**, 101 (2014).

[81] C. Hamaguchi, ed., *Basic Semiconductor Physics*. Springer, Berlin, 2014.

[82] A. A. Dremin, D. R. Yakovlev, A. A. Sirenko, S. I. Gubarev, O. P. Shabelsky, A. Waag, and M. Bayer, *Electron cyclotron mass in undoped CdTe/CdMnTe qunatum wells*, Phys. Rev. B. **72**, 195337 (2005).

[83] W. J. Ossau and B. Kuhn-Heinrich, *Dimensional dependence of antiferromagnetism in diluted magnetic semiconductor heterostructures*, Physica B **184**, 422 (1993).

[84] D. Keller, D. R. Yakovlev, B. König, W. Ossau, Th. Gruber, A. Waag, L. W. Molenkamp, and A. V. Scherbakov, *Heating of the magnetic ion system in (Zn,Mn)Se/(Zn,Be)Se semimagnetic quantum wells by means of photoexcitation*, Phys. Rev. B. **65**, 035313 (2001).

[85] M. Dyakonov and M. S. Shur, *Detection, Mixing, and Frequency Multiplication of Terahertz Radiation by Two-Dimensional Electronic Fluid*, IEEE Trans. Electron. Dev. **43(3)**, 380 (1996).

[86] D. Coquillat, V. Nodjiadjim, A. Konczykowska, M. Riet, N. Dyakonova, C. Consejo, F. Teppe, J. Godin, and W. Knap, *InP Double Heterojunction Bipolar Transistor As sub-Terahertz Detector*, in *Digest of International Conference on Infrared Millimeter and Terahertz Waves*. 2014.

[87] C. Drexler, N. Dyakonova, P. Olbrich, J. Karch, M. Schafberger, K. Karpierz, Yu. Mityagin, M. B. Lifshits, F. Teppe, O. Klimenko, Y. M. Meziani, W. Knap, and S. D. Ganichev, *Helicity sensitive terahertz radiation detection by field effect transistors*, J. Appl. Phys. **111**, 124504 (2012).

[88] K. S. Romanov and M. I. Dyakonov, *Theory of helicity-sensitive terahertz radiation detection by field effect transistors*, Appl. Phys. Lett. **102**, 153502 (2013).

Danksagung

Ich möchte mich an dieser Stelle recht herzlich bei allen bedanken, die mich während meiner Promotion begleitet und unterstützt haben.

Besonderer Dank gilt Herrn Prof. Sergey D. Ganichev, der mir die Möglichkeit gab diese Promotion in seiner Arbeitsgruppe durchzuführen. Ich bedanke mich, dass er sich immer Zeit genommen hat, meine Fragen zu beantworten und eingehend zu erklären.

Ebenso möchte ich mich bei meinen Eltern dafür bedanken, dass sie mir mein Studium ermöglicht haben und mich immer bei allen Dingen unterstützt haben.

Weiterhin möchte ich Peter Olbrich und Sergey Danilov danken, die immer bereit waren mir bei experimentellen Fragen mit Rat und Tat zur Seite zu stehen, auch wenn es nicht immer leicht mit mir war. Ich möchte mich auch bei meinen Bachelor- und Master-Studenten Leonhard Schell, Alexander Pfaller, Willibald Probst, Jan Unverzagt und Stefan Hubmann für die Unterstützung bei den Experimenten für diese Dissertation bedanken. Mein besonderer Dank gilt meinen Doktorandenkollegen Kathrin-Maria Dantscher, Helene Plank und Tobias Herrmann, die für eine stets gute Stimmung gesorgt haben und auch aufbauende Worte fanden! Danke! Auch unseren Technikern Toni Humbs und Christian Schneider möchte ich für die rasche Umsetzung diverser Aufbauten danken, sowie Frau Hannelore Lanz für die Unterstützung bei formellen Fragen. Ich möchte mich auch hiermit bei Helene Plank, Rosemary Simpson und Tobias Herrmann fürs Korrekturlesen meiner Arbeit bedanken. Ein weiterer Dank geht an die Kollegen vom Lehrstuhl Weiss für ihre Hilfe beim Probenstrukturieren. Besonderer Dank auch an die Kollegen Leonid Golub, Eugenius Ivchenko, Thomas Wojtowicz, Vasily Popov und Vasily Bel'kov für die Hilfe bei den Experimenten und den theoretischen Hintergründen von den Ergebnissen. Ein weiterer Dank gilt allen meinen Kollegen und Kooperationspartnern, die ich nicht namentlich erwähnt habe.

Zuguterletzt möchte ich mich bei meiner Freundin Maria Beck für ihre Unterstützung und stets aufbauenden Worten bedanken! Vielen Dank!